UNIVERSITÀ DEGLI STUDI DI PADOVA

DIPARTIMENTO DI SCIENZE CHIMICHE

CORSO DI LAUREA MAGISTRALE IN CHIMICA

TESI DI LAUREA MAGISTRALE

Spectroscopic Investigation on Orange Carotenoid Protein (OCP): From the Activation Mechanism to the Development of OCP-based Fluorescent Nanoparticles

Relatore: Prof.ssa Donatella Carbonera
Correlatore: Prof. Alberto Mezzetti
Controrelatore: Prof. Alberto Gasparotto

Laureando: Calcinoni Andrea

Anno Accademico: 2021/2022

UNIVERSITÀ
DEGLI STUDI
DI PADOVA

SORBONNE
UNIVERSITÉ
CRÉATEURS DE FUTURS
DEPUIS 1257

Contents

1

Abstract

Orange Carotenoid Protein (OCP) is a photoactive water-soluble protein involved in photoprotective functions. Among different strains of cyanobacteria OCP is responsible of photoprotection processes through non-photochemical quenching (NPQ) of excess light energy absorbed by antenna systems as well as quenching of reactive oxygen species (ROS). The photoactivation mechanism is triggered by blue/green light absorption which induces the protein to undergo a conformational variation from a dark-adapted state (OCP^O) to an active state (OCP^R), the latter activating photoprotective mechanisms. Optical FTIR spectroscopy was applied in order to elucidate the process. In particular, as previous studies suggest that an important function might be played by internal water molecules, FTIR light-*minus*-dark difference spectroscopy on OCP in solution was used to investigate this aspect. With the perspective of applying OCP properties to the development of photochromic nanodevices, a protocol to adsorb OCP on aminopropyl functionalized mesoporous silica SBA-15-NH_2 nanoparticles was followed, finding that OCP remains photoactive even inside silica matrix. Fluorophores such as cyanines and flavonoids were adsorbed on SBA-15-NH_2 in presence of OCP in order to create tunable fluorescent systems with a possible application in fluorescence imaging and other domains. Furthermore, EPR spectroscopy was applied to OCP in solution and adsorbed on SBA-15-NH_2 nanoparticles, alone or in presence of a chlorophyll *a* photosensitizer, in order to detect and characterize possible paramagnetic states of OCP's internal carotenoid molecule. Preliminary, but not conclusive results are reported.

2

Introduction

The research project of this master's degree thesis was achieved through a collaboration between University of Padova (Italy) and Sorbonne University (France) in the framework of an Erasmus+ Traineeship mobility from February to July 2022. The objectives of the presented research work revolve around the study, mainly by a spectroscopic approach, of some peculiar properties of Orange Carotenoid Protein (OCP). Even though OCP was discovered more than forty years ago, the protein mechanism of photoactivation is still not fully elucidated. This makes OCP a lively topic of discussion among many researchers. OCP consists of a small water-soluble protein that performs photoprotective activity in cyanobacteria. All photosynthetic organisms present specific mechanisms that protect the photosynthetic apparatus from photodamage. Cyanobacteria have a unique photoprotective system where OCP plays a key role. In presence of intense blue/green light illumination OCP converts from a dark-adapted state (named OCP orange - OCP^O) to an active state (named OPC red - OCP^R). The strong light absorption that triggers the consequent photoconversion of OCP is due to an internal carotenoid molecule which spans inside the protein. The active state OCP^R of the protein performs photoprotection by binding the antenna systems of cyanobacteria, the phycobilisomes (PBS), and dissipating their excess light energy through non-photochemical quenching (NPQ). In addition, OCP also shows the ability to quench reactive oxygen species (ROS) such as singlet oxygen. OCP is therefore a photoactive protein that performs photoprotection by multiple synergic paths. As mentioned above, the activation mechanism of the protein (the conversion from OCP^O to OCP^R) is a complicated process still not fully understood. Different hypothesis, sometimes in contrast with each other, have been proposed to try to explain this photochemical process. In order to contribute to clarify this issue, the first part of the research project was dedicated to the study of the activation mechanism. Time Resolved light-*minus*-dark Difference Infrared Spectroscopy (DS-FTIR) was applied on OCP in solution for our research purposes. A protocol for proton/deuterium exchange was applied on OCP and the deuterated protein was studied using the same technique. The comparison between the measurements done in normal OCP and in deuterated OCP provided a strategy for spectra analysis and band assignment. The attention was focused on the wavenumber region where stretching bands of water absorb (3700-3200 cm^{-1}). Previous studies performed by Gupta *et al.* (Proc. Natl. Acad. Sci. U.S.A. (2015) 112,

E5567-74) suggest that internal water molecules may actively participate during the activation mechanism and contribute to an efficient photoconversion of the protein. This led us to focus on an infrared analysis that could detect the presence of putative water molecules involved in the photoactivation mechanism.

Another important spectral characteristic of OCP is its Vis absorption spectrum. The inactive state OCP^O of the protein shows a strong absorption maximum around 480 nm due to the presence of the carotenoid molecule, which happens to be a strong chromophore. After conversion to the active state OCP^R, the absorption spectrum is modified with a red-shifted peak at around 510-520 nm. The development of the second part of the project is based on the idea that the spectral changes of the protein during photoactivation could be used to create photochromic devices. Thus, first we decided to adsorb OCP on a solid support made of nanoparticles. The chosen material was SBA-15 mesoporous nanoparticles, as they are a very well-known inorganic scaffold with high surface area that can adsorb and stabilize proteins and enzymes. By regulating the experimental conditions during SBA-15 synthesis it is possible to easily control the specific properties of the material, such as the mean pore diameter, for an efficient protein loading. The actual nanoparticles that have been adopted for our purposes consisted of aminopropyl post-functionalized SBA-15 particles (SBA-15-NH_2) that have been prepared through a grafting protocol starting from normal SBA-15 and using the APTES molecule as a grafting agent. Solid state UV-Vis spectroscopy on the final synthesised system proved that OCP can be adsorbed on nanoparticles and its photoactivation mechanism remains effective and preserved. In addition, the process was found to be reversible. With the perspective of applying SBA-15-NH_2 particles loaded with OCP as a tunable fluorescent system, solid state fluorescence emission spectroscopy was applied to investigate this aspect. OCP does not have significant detectable fluorescence emission. Thus, different fluorophores like cyanines and flavonoids were adsorbed on SBA-15-NH_2 nanoparticles in the presence of OCP . The fluorophores acted as light emitters, whereas OCP ensured a mechanism that could regulate reversibly the intensity emission of the fluorophores trough protein photoactivation.

FTIR analysis on OCP in solution and synthesis and characterization by fluorescence emission (and other techniques) of fluorescent SBA-15-NH_2 nanoparticles loaded with fluorophores and OCP were performed at Laboratoire de Réactivité de Surface (LRS) – Sorbonne Université, Paris (France) under the kind supervision of Dr. Alberto Mezzetti.

The last part of the project was dedicated on Time Resolved Electron Paramagnetic Resonance spectroscopy (TR-EPR) applied to OCP under photoexcitation. Different paramagnetic states of the internal carotenoid molecule, mainly triplet states and charge-separation states, might be populated and characterized by the technique, thus adding information on the photophysical and magnetic properties of the protein. First, a TR-EPR analysis on OCP in solution and OCP immobilized in SBA-15-NH_2 nanoparticles was performed. Photoexciting the samples at the wavelength of maximum absorption of the carotenoid, we tried to detect possible light-induced paramagnetic states that might have a key role in the photoactivation cycle of the pro-

tein. Another way to populate a paramagnetic state of a molecule, specifically a triplet state, is through triplet-triplet energy transfer (TTET) between a donor (also called photosensitizer) and an acceptor. For example, this is the case of photoprotection mechanisms in plants and algae where the triplet state of chlorophylls, that can be a source of photodamage, is transferred to carotenoids. Basing our approach on these natural systems, we tried to detect the triplet state of OCP's carotenoid via TTET between an external chlorophyll *a* molecule, acting as a photosensitizer, and OCP both adsorbed on SBA-15-NH_2. The protein environment can largely affect the properties of the electronic triplet state of carotenoid; investigations of this aspect using TR-EPR on our system under different wavelengths of photoexcitation were attempted.
EPR analysis on chlorophyll and OCP inserted in mesoporous SBA-15-NH_2 was performed at Department of Chemical Sciences – University of Padova (Italy) under the kind supervision of Prof. Donatella Carbonera and Prof. Marco Bortolus.

3

The Orange Carotenoid Protein

Light is essential in photosynthetic organisms. Evolution in the course of time provided for an efficient method for environmental sunlight energy collection in the natural conditions of fluctuating irradiance. This method consists in the light harvesting antenna systems. Antenna systems in plants, algae and cyanobacteria are a supramolecular assembly of proteins and pigments aiming to absorb, harvest and transmit energy to reaction centres in order to sustain photosynthesis [1]. But, in the circumstances of high intensities, light becomes a threat for cell survival. Oversaturation of the photosynthetic chain leads to generation of oxidizing species that can eventually cause photodamage to the cell apparatus. So, living organisms need to sense and respond to environmental sunlight oscillations in order to overcome dangerous oxidative stress in the case of excessive overexposure. Photoprotection generally includes all the different possible mechanisms through which the light-harvesting systems are reversibly converted into a photoprotected state. In this case, the efficient properties of transmission of energy to the reaction centres are minimized, transforming into heat the light energy surplus that may be absorbed by the antennae [2].

Cyanobacteria own a specific mechanism of photoprotection that differs from the one shown in plants and algae. In cyanobacteria, a special water-soluble protein called Orange Carotenoid Protein (OCP) acts as a reversible photoreceptor that can master photoprotective tasks [3, 4]. Through absorption of blue/green light, OCP converts into an activated form that interacts with the antenna systems of cyanobacteria, the phycobilisomes (PBS), and quenches their excess energy by thermal dissipation. Moreover, it is reported that OCP can block reactive oxygen species (ROS), neutralizing them before compromising the cell [37].

OCP was first discovered in 1981 [5] and in 1997 it was isolated and partially sequenced [6]. However, only in 2006 the photoprotective roles of OCP were clarified [7], while in 2008 the photoactive properties as a reversible photoreceptor were confirmed [8]. Nowadays, OCP is still the subject of study by many research groups. Albeit several properties of the protein have been already assessed and commonly accepted by the scientific community, there are still some hot topics under discussion. In particular, the details of the photoactivation mechanism of OCP remain an unresolved aspect. The FTIR analysis performed on the protein during this thesis work had the objective to shed some light on the activation mechanism, especially regarding the

critical involvement of possible water molecules participating in the process.

3.1 Structure

Up to date, there have been discovered at least three different paralog families of OCP, called OCP1, OCP2 and OCPX [9]. The majority of all OCPs that are present in cyanobacteria belong to the OCP1 category. From now on the term OCP that will be used during this report, and all the described properties of the protein, are referred to the OCP1 found in the well-characterized *Synechocystis* PCC 6803 cyanobacteria or in *Arthrospira maxima*.

OCP is a water-soluble 35 kD protein structurally composed of two different domains: a N-terminal domain (NTD) and a C-terminal domain (CTD). Phylogenomic analysis and bioinformatics applied on a multitude of sequenced cyanobacteria have identified homologous proteins of the NTD and CTD domains of OCP. The NTD-like proteins, called Helical Carotenoid Proteins (HCPs) [10], and CTD-like proteins (CTDHs) [11] are thought to be ancestral precursors that have been fused together in a primordial cyanobacterium, resulting in the formation of OCP.

The first OCP crystal structure from *A. maxima* was reported in 2003 [12], while for *Synechocystis* PCC 6803 the structure was determined in 2010 [13].

The NTD (residues 19-165, numbering after *Synechocystis* OCP) is composed of an all α-helix structure divided in two four-helix bundles. In contrast, CTD (residues 193-311) presents a mixed α/β fold that comprises a five-stranded β-sheet core flanked by three α-helices [13]. A 28-aminoacid flexible linker connects the NTD to the CTD. The two domains are close together in space, giving OCP a globular-like shape (Figure 3.1). Interdomain interactions between NTD and CTD stabilize the said conformation, in particular through a salt bridge between R155 and E244. In addition, the portion of the protein formed by residues 1-20, the helical N-terminal extension (NTE), anchors to an external part of CTD, keeping the two domains associated. In the centre of the protein, placed inside a hydrophobic pocket, a carotenoid molecule (3'-hydroxyechinenone, hECN) is shared between NTD and CTD. The carotenoid is kept in position through H-bonds between the keto group in the β1 ring of the carotenoid and aminoacides Y201 and W288 inside CTD. On the other side of the molecule, the hydroxyl group bonded to the β2 ring is involved in π interactions with Y44 and W101 (inside NTD) [13]. It is also known that OCP can be reconstructed with different carotenoids other than 3'- hydroxyechinenone: echinenone (ECN), canthaxanthin (CAN), and zeaxanthin [14].

At low concentration OCP is organized as a single monomer. In contrast, at higher concentrations the protein tends to form dimers and even tetramers [15].

The structure of OCP as described is related to the inactive dark-adapted state OCP^O. The tridimensional arrangement of the photoactivated form OCP^R is still not characterized due to lacking of crystallographic data. However, research works based on crosslinking experiments [16] and comparisons between full OCP and isolated NTD containing the carotenoid [17] allowed to gain some structural information on OCP^R that will be briefly described in the following paragraphs.

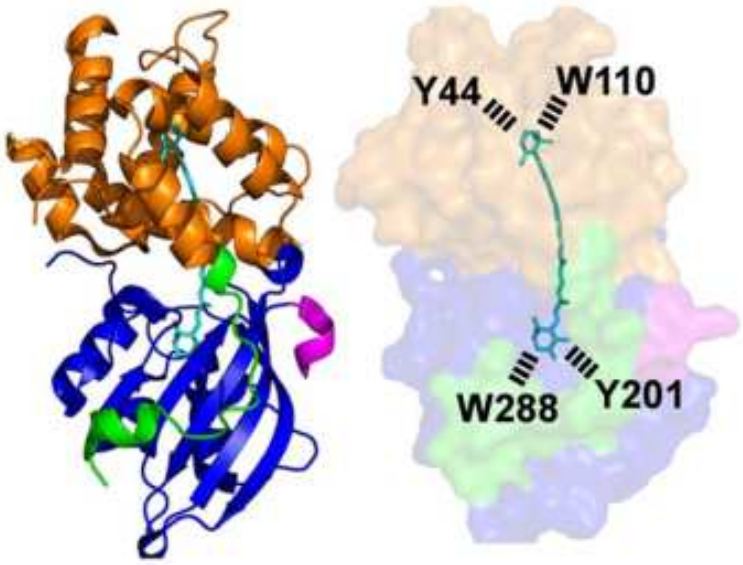

Figure 3.1: OCP crystal structure from *Synechocystis* PCC 6803 (Protein Data Bank ID: 3MG1). In orange, the all α-helix structure of NTD. In blue, the mixed α/β structure of CTD. In green, the NTE. On the right, H-bond and π interaction network of the bonded internal carotenoid. Image taken from reference [14].

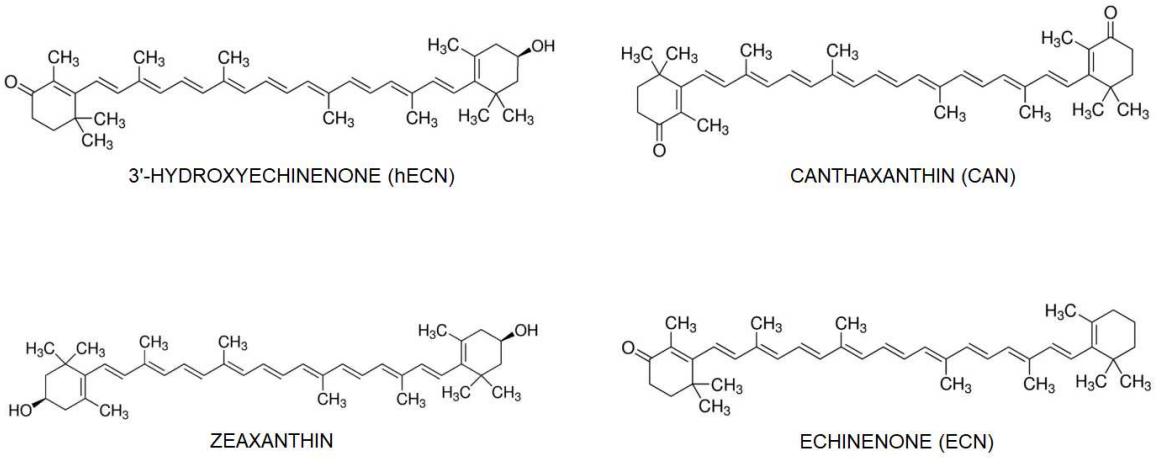

Figure 3.2: Chemical structures of different carotenoids.

3.2 The Activation Mechanism

OCP photoprotection is executed only by the activated form OCP^R. After absorption of light, the protein converts from the inactive state OCP^O to the photoactive state OCP^R. The letters O and R stand for "orange" and "red", as the protein assumes an orange colour in the dark-adapted state and then changes to red after photoactivation. The mechanism through which OCP turns from its orange state to its red state consists in a very complex process still under discussion. The photocycle spans multiple timescales. It starts from femtosecond dynamics, mainly involving localized modifications of the electronic state of the internal carotenoid, to millisecond dynamics which impacts the overall structural OCP conformation. Summarizing, absorption of light by the carotenoid induces the breakage of H-bonds between the C=O group

of the carotenoid and two specific OCP residues (a Tyr and a Trp) of the CTD of the protein. Next, the carotenoid translocates inside the NTD, moving about 12 Å from its initial position. As a consequence, the NTD and CTD domains dissociate from one another, giving OCP a more elongated shape and a loosened structure. Thus, the OCP^R form is accumulated.

3.2.1 Carotenoid dynamics

Multiple studies, mainly by ultrafast transient UV-Vis spectroscopy, clarified the sequencial steps that characterize the photophysics of the carotenoid molecule during the activation cycle [18 - 23].

First, the absorption of a blue/green photon promotes the molecule from the ground state to its excited S_2 state ($S_0 \rightarrow S_1$ transition is prohibited due to symmetrical reasons [24]). In 80-100 femtoseconds the S_2 state decays into a set of different excited states: a sub-picosecond-lived intramolecular charge-transfer (ICT) state, a picosecond-lived mixed S_1/ICT state, called usually S_1, and an excited state S* characterized by a lifetime in the range of few picoseconds [23]. It was proposed that the S* state is associated to a distorted carotenoid conformation that leads to H-bond breakage between the carotenoid and the Y201/W288 residues of OCP [20]. It was also supposed that a carotenoid cis/trans isomerization could occur during the photocycle [17, 25], however other studies confute this scenario [20]. More recent scientific works on OCP suggest that it is rather the S_1 state the precursor that leads to H-bond breakage [23]. After these photochemical processes, more than 99% of the population of the excited photoproducts relaxes to S_0 state, restoring the original conditions of the carotenoid and of OCP. Less than 1% of the population retains the loose H-bond network, giving rise to the photoproduct P1. In the timescale of nanoseconds/microseconds, passing through different intermediate states from P1 to P3, the carotenoid migrates inside the NTD [20].

The new chemical environment in which the carotenoid is inserted influences the Vis spectral properties of OCP. At the beginning, OCP^O shows an absorption spectrum with vibronic bands at 474 nm and 500 nm and a shoulder at 440 nm. In OCP^R, the modified chemical surroundings cause a redshift of the absorption spectrum to 515 nm and the disappearance of the vibronic structure (Figure 3.3). The features of the absorption spectrum depend also on the type of carotenoid that is located inside the protein. The absorption wavelengths just mentioned are referred to OCP reconstructed with canthaxanthin.

The intricacy of the photocycle is made even more complicated by other aspects. The type of carotenoid, the exact excitation wavelengths and the excitation power can all influence the photochemistry of the process. Regarding this last aspect, it was postulated that at high excitation energy a multiphoton process can occur [23].

3.2.2 Conformational changes

In the timescale of microseconds/milliseconds the protein changes its 3D structure upon photoactivation. The internal carotenoid stabilises the resting-state conformational organisation of OCP^O using the network of H-bonds between the carotenoid carbonyl group and some OCP

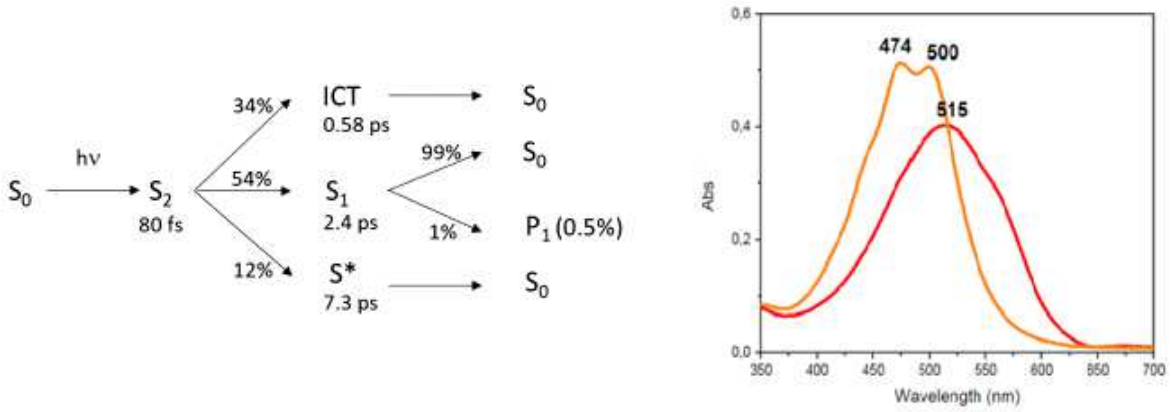

Figure 3.3: On the left, lifetimes of the different photoproducts of OCP's carotenoid. Image taken from reference [23]. On the right, absorption spectrum of inactive OCP^O (orange trace) and active OCP^R (red trace) states of OCP(CAN) in aqueous solution 0.3 mg/mL.

Figure 3.4: Structural changes of OCP during photoactivation. Image taken from reference [20].

residues. The absorption of light triggering the photophysical dynamics described above causes a rupture of these H-bonds. As a consequence, the stabilized structure is compromised and the two domains NTD and CTD dissociate. The protein assumes a more elongated structure where the NTD and CTD are far apart, kept together only by a small flexible linker. The involvement of specific H-bonds is confirmed by the fact that OCP reconstructed with zeaxanthin (which does not have any carbonyl groups forming H-bonds) is not photoactive [26].

Spectroscopic FTIR studies tried to characterize the structural changes from OCP^O to OCP^R [20, 27]. In particular, it has been proposed that the unfolding of some α-helices may occur. First, a modification of an internal nonsolvent-exposed α-helix is supposed to be at the beginning of the conformational variation. Following this, the unfolding of other structural motifs, the NTE and/or the CTT (C-terminal tail) takes place, undocking from the CTD. In addition, as the protein photoactivates, the dimerization equilibrium is modified and OCP assumes a monomeric form [28].

3.3 Photoprotection

3.3.1 OCP interaction with antenna systems

OCP acts as a quencher of fluorescence of the phycobilisomes (PBS), the antenna systems of cyanobacteria. The interaction between OCP and PBS blocks the mechanism of energy transfer between PBS and reaction centres (RC) of photosynthesis, photoprotecting them from excessive light energy which can cause production of oxidizing agents [4]. Only the active state OCP^R can bind PBSs. As mentioned in the last paragraph, the quantum yield of OCP^R is lower than 1%, confirming that photoprotection mechanism by OCP starts only as required, i. e. in the condition of high luminous irradiance. OCP binds to PBS through a set of multiple interactions between specific aminoacids. Above all, the residue R155 of OCP is crucial for OCP binding [29]. This aminoacid is part of the NTD, it is placed in the interface between NTD and CTD and participates in a salt bridge with the residue E244 of CTD. After photoactivation, the dissociation of NTD from CTD exposes R155, which can eventually interact with PBS. Recent studies have shown that other residues together with R155 are involved in PBS binding, all of them positioned in the NTD/CTD interplay and close to the β1 ring of the carotenoid [30]. The portion of the protein that mainly interacts with PBS is the NTD, as the carotenoid that performs photoprotection is translocated inside the NTD after photoactivation. Furthermore, studies have shown that the isolated NTD can quench PBS, but not the CTD. This information leads us to consider that NTD can be defined as the effector domain of photoprotection because it binds PBS performing photoprotective actions, while the CTD can be called regulator domain, since its dissociation from NTD exposes the residues (belonging to NTD) that bind PBS [31]. It was proposed that a single molecule of OCP binds to one of the basal cylinders that compose the core of PBS [32], quenching most of PBS fluorescence. However, another study suggests that to achieve 100% fluorescence quenching, two OCPs are necessary [33].

Experiments *in vitro* have shown that OCP^R back-converts to its orange inactive form with a rate that depends mainly on temperature [34]. Conversely, OCP^R *in vivo* requires the presence of an additional protein, called Fluorescence Recovery Protein (FRP) in order to return to OCP^O [35]. In the absence of FRP the cell remains in a quenched state even in dark.
FRP is an all α-helix elongated protein [36] that performs two different activities: it is essential for the OCP^R-to-OCP^O conversion reaction and it promotes the detachment of OCP^R from PBS. FRP interacts with CTD, triggering the separation of OCP from PBS, and brings together NTD and CTD stabilizing an intermediate state that facilitates the back conversion.

3.3.2 OCP ability to quench reactive oxygen species

As a secondary protective function, OCP is able to quench reactive oxygen species (ROS) [4], the main component of this category being singlet oxygen $^1O_2$. Cyanobacteria are dangerously exposed to oxidative stress by $^1O_2$ because pigments like chlorophylls and bilins act as photo-

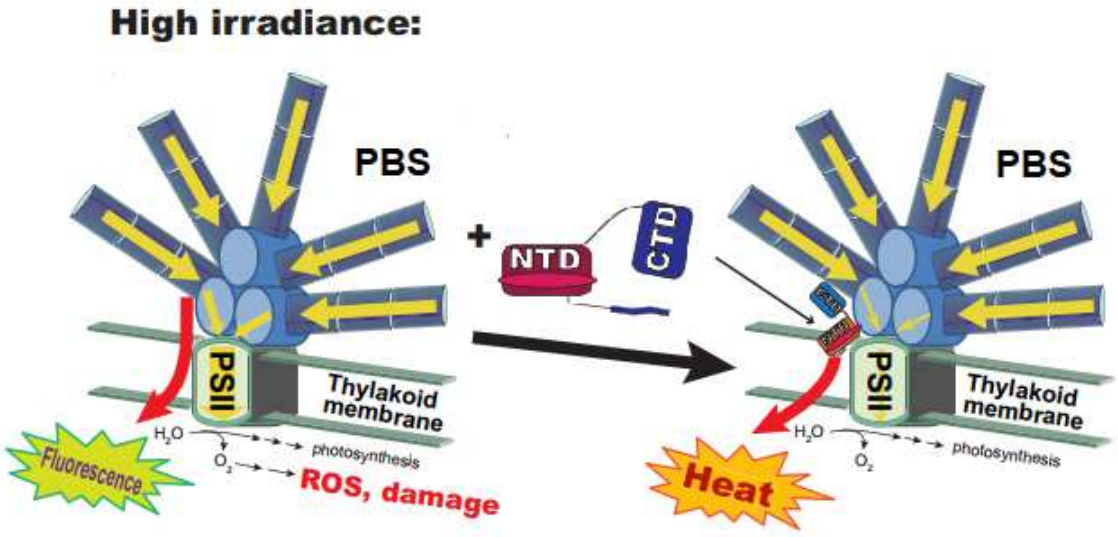

Figure 3.5: Interaction between OCP and PBS. Image taken from reference [3].

sensitizers for $^1O_2$. In the case of high-light conditions, chlorophyll and bilin triplet states are accumulated, leading to formation of $^1O_2$. Also, charge recombination reactions at the level of the reaction centres are most likely related to formation of oxidative species. Studies conducted by spin trapping EPR spectroscopy [37, 38] confirm that OCP can suppress $^1O_2$ accumulation, supporting a protective activity towards ROS. Both OCP^O and OCP^R can quench $^1O_2$, as it has been reported that even under red illumination, which does not activate OCP, the protein can block singlet oxygen.

The exact mechanism through which OCP quenches singlet oxygen is not clarified in detail. Two possible paths can be supposed: an energy transfer between the carotenoid molecule and $^1O_2$, or a direct oxidation reaction that causes degradation of the carotenoid.

3.4 Applications of Orange Carotenoid Protein

The interesting photoactive and spectral properties of Orange Carotenoid Protein inspired a few studies on the application of OCP in different ways in order to create photoactive switches and sensors.

In 2017 Andreoni *et al.* [39] developed a system in which OCP and two organic dyes Cy3 and Cy5 were attached to a DNA scaffold. It turned out that, upon absorption of light energy from Cy3, the energy transfer between Cy3 and Cy5 could be regulated by photoactivation of OCP, thus tuning the fluorescence emission from Cy5. The creation of this switch on/off device inspired the development of our fluorescent nanoparticles based on OCP, Cy3 and Cy5 adsorbed on SBA-15-NH_2 solid support.

In 2019, Maksimov *et al.* [40] designed a system made of chimeras based on OCP that could find application as a temperature sensor. In particular, fluorescent proteins GFP (Green Fluorescent Protein) and RFP (Red Fluorescent Protein) have been genetically encoded to the OCP sequence in *E.coli.* Monitoring the fluorescence intensity after photoactivation of OCP, the two

systems RFP-OCP and OCP-GFP showed to be suitable for temperature measurements in microenvironments. The temperature could in fact affect the energy transfer between the proteins and, as a response, their fluorescence emission.

4

FTIR Analysis on OCP Photoactivation

Fourier Transform Infrared spectroscopy is a common and versatile technique used in every field of chemical sciences. From the study of simple molecules to the characterization of large complex chemical systems, FTIR spectroscopy is widely applied routinely in a variety of circumstances. The possibility to adopt an FTIR analysis in almost every situation arises from the fact that the physical observables detected by the technique, which are the energies involved in vibrational transitions, reflect important and specific chemical properties that characterize the sample. All polyatomic systems present multiple vibrational degrees of freedom that can be investigated by infrared spectroscopy. The composition, the structure, the presence of intermolecular o intramolecular interactions can all affect the vibrational degrees of freedom and thus the FTIR response [41].

The considerable information content that is present in an infrared spectrum carries over also to biological systems. In the case of proteins, FTIR analysis is applied in order to obtain information on protein structure and molecular mechanisms of protein reactions, folding and unfolding. The backbone of the protein, the side chains of aminoacids, cofactors and water molecules are constituents of the protein that can all give rise to meaningful infrared signals. The extensive set of chemical groups that are infrared-active in a protein apparently makes the spectrum analysis difficult to be done. In fact, the large number of superimposed bands that are slightly modified in intensity and position after a reaction or a conformational change of the protein cannot be easily detected and interpreted looking at the absolute absorption spectrum. Difference infrared spectroscopy (DS-FTIR) is much more useful. In DS-FTIR, a first spectrum of the sample in its initial conditions is recorder and considered as the background of the system. Then, the protein reaction is induced and a new infrared spectrum is recorded. The subtraction of the background from the new spectrum allows to obtain a difference infrared spectrum, where only spectral contributions arising from the part of the protein that change because of the reaction will be present.

In this chapter, the DS-FTIR analysis on the activation mechanism of OCP will be presented. Before this, a brief overview on some theoretical considerations of infrared spectroscopy will be described.

4.1 Theory of FTIR analysis on proteins

In this section, some important technical and theoretical characteristics of infrared spectroscopy applied to proteins are described. In particular, the Fourier Transform elaboration, the sampling technique, the time resolved resolution, the difference spectroscopy approach and some specific considerations on the relationship between chemical structure of proteins and infrared absorption.

4.1.1 Fourier Transform spectroscopy

All modern infrared spectrometers are Fourier Transform infrared spectrometers (FT-IR). This means that the intensity of the IR light beam passing through the sample is not detected as a function of frequency but rather as a function of a difference in path of two incident beams. The demodulation of the recorded signals by Fourier Transform elaboration permits to obtain a spectrum in frequency. To adopt this methodology, infrared spectrometers are equipped with an interferometer, like the Michaelson interferometer (Figure 4.1).
In the Michaelson interferometer setting, the light generated by the IR source is directed towards a beam splitter, which separates IR rays in two different beams. One is sent to a fixed mirror, the other is conducted to a movable mirror which inserts a varying path difference d. The two beams are then recombined, sent to the sample, and detected. The intensity of the recombined beam depends on the phase difference between the two initial beams, which can either interfere constructively or destructively depending on the difference in path lengths.
Focusing on a single component of wavenumber $\tilde{\nu}$, the intensity recorded at the detector in the range of wavenumbers $\tilde{\nu}$ and $\tilde{\nu} + d\tilde{\nu}$ depends on the difference of path d and on the initial intensity $I(\tilde{\nu})$:

$$I(d, \tilde{\nu})d\tilde{\nu} = I(\tilde{\nu})(1 + cos2\pi\tilde{\nu}d)d\tilde{\nu} \tag{4.1}$$

The actual signal consists in a radiation spanning a wide range of wavenumbers (as the IR source

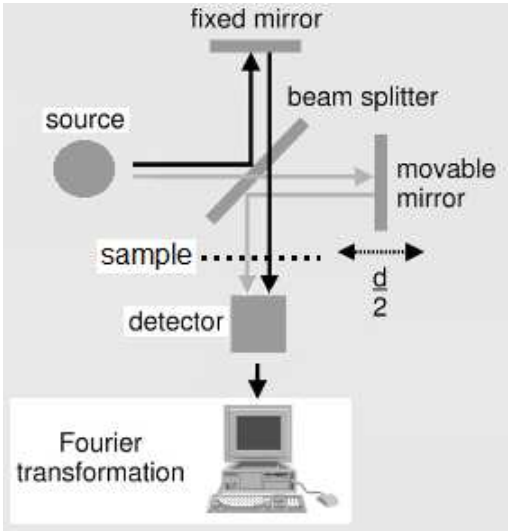

Figure 4.1: Scheme of the Michaelson interferometer. Image taken from reference [42].

is polychromatic) and the total intensity at the detector is the sum of all the contributions:

$$I(d) = \int_0^\infty I(d, \tilde{\nu})d\tilde{\nu} = \int_0^\infty I(\tilde{\nu})(1 + cos2\pi\tilde{\nu}d)d\tilde{\nu} \tag{4.2}$$

The plot of $I(d)$ against d is called an interferogram. The interferogram as it is, without any additional manipulation, is too difficult to interpret. The main information hidden in the interferogram is the intensity of each component $I(\tilde{\nu})$. This information can be extracted performing a Fourier transform of the interferogram. The result is a plot of $I(\tilde{\nu})$ against $\tilde{\nu}$, which is the absorption spectrum, also called *single beam spectrum*.
One of the main advantages of using a Fourier transform approach is the very rapid data collection and, as a consequence, the possibility to register multiple spectra one after the other in order to obtain high signal to noise ratios.

4.1.2 IR Samples

The most common measurement technique in infrared spectroscopy is transmission: the infrared light passes through a sample holder (cuvette or window) containing the protein, usually solubilized in a water buffer, and then reaches the detector. If the sample is homogeneous, the amount of absorbed light follows the Lambert-Beer law:

$$A(\tilde{\nu}) = -log(I(\tilde{\nu})/I_0(\tilde{\nu})) = c\epsilon(\tilde{\nu})p$$

where A is the absorbance, I and I_0 the intensity of light after and before interacting with the sample, c the concentration of the protein, $\epsilon(\tilde{\nu})$ the molar extinction coefficient at the specific wavenumber and p the path length. Typically, for an infrared analysis on proteins, the sample is placed between two windows made of CaF_2, which is a IR transparent material.
A drawback of the transmission technique in aqueous solution is the strong absorbance of water. The band at 1645 cm^{-1} that can be assigned to the bending mode of water is superimposed with the important amide I band of the protein. A way to solve this problem is to dry the sample as much as possible, always having in mind that a protein too dehydrated might denaturate or not work properly. Another possibility is to use ^2H_2O as its bending mode is downshifted at around 1210 cm^{-1}.

4.1.3 Difference Spectroscopy

As mentioned earlier, an infrared spectrum of a protein contains a very large number of peaks that usually overlap together, making the spectrum difficult to interpret. A way to solve this problem is to reduce the components that contribute to the spectrum. This can be achieved using difference techniques. These types of analysis are particularly suited to investigate protein reactions, in which the system changes its state: the modification of the absorbance during the course of reaction can be detected by difference spectroscopy and thus the properties of the system can be assessed.
In difference spectroscopy, a first IR absorption spectrum of the protein in its initial state, called state A, is recorded. Afterwards, the protein reaction is induced, so that the final state B of

the protein is obtained. A new infrared absorption spectrum of the state B is recorded. The subtraction of the spectrum A (which can be considered as a background) from spectrum B allows to obtain a difference infrared spectrum (DS-FTIR). Using this approach, all the positive and negative bands that appear in the difference spectrum reflect chemical modifications of the system, while all the components that do not change during the protein reaction cancel out. In particular, positive bands are related to the final state of the system, while negative bands are associated to the initial state.
The changes in absorbance after protein reaction are usually very low. This means that subtracting two spectra from two different samples (one for state A and the other for state B) is not the most suggested way to perform difference spectroscopy. It is rather more useful to induce the protein reaction directly inside the spectrometer, so that the initial and final states of the system are detected on the same sample.
Difference FTIR spectroscopy has been widely applied to study photoinduced reactions [43], photoreceptors [44] and photosynthetic systems [45]. In the following paragraphs, application of DS-FTIR spectroscopy on the study of OCP photoactivation mechanism will be described.

4.1.4 Time Resolution

As the protein reacts, it is interesting to monitor the time evolution of the system in order to understand the kinetics (or other aspects) of the protein reaction. One of the most used methods to obtain time resolution is to displace the movable mirror of the interferometer as fast as possible, thus recording multiple spectra one after the other, noting down in a recursive way the instant of time in which each spectrum was made. This procedure is called *rapid scan* technique. The time resolution that can be reached using *rapid scan* mode is in the timescale of milliseconds-seconds.
However, there are some requirements that need to be verified for a time resolved *rapid scan*

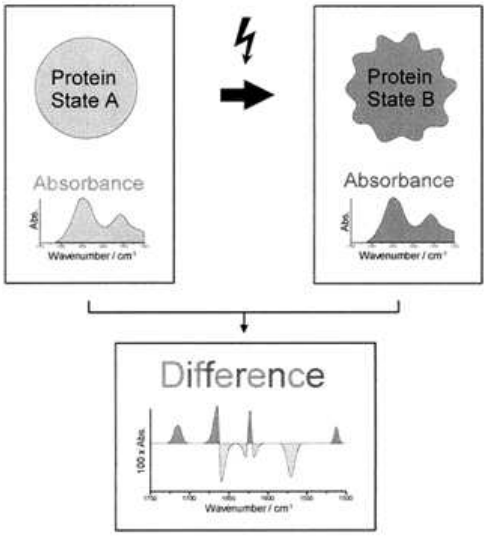

Figure 4.2: Scheme for difference FTIR spectroscopy.

analysis. First, the movable mirror of the Michaelson interferometer must displace very rapidly (2 - 10 cm/s). Moreover, the instrument must be equipped with a very sensible detector having a fast response, for example a photoconductive HgCdTe (MCT) detector cooled down with liquid N_2, as in this thesis. A fast analog-to-digital converter is also mandatory in order to convert properly the oscillating signals.

4.1.5 IR absorption of proteins

The chemical structure and composition of proteins strongly affects the FTIR response. The chemical functional groups that give rise to the most important IR signals are located on the side chains of amioacids and in the backbone. In particular, the amide functional group that links all the different aminoacids composing the protein is one of the main source of infrared absorption that contains information on the protein properties, the secondary structure above all. Four main IR bands related to the backbone amide functional group can be distinguished [46]:

- *NH stretching vibration:* The N-H bond gives rise to stretching bands between 3300 cm^{-1} and 3000 cm^{-1}. In detail, N-H stretching is composed of two different contributions: amide A (at higher wavenumbers) and amide B (at lower wavenumbers). The identification of these bands in the IR spectrum is usually not feasible because they are superimposed to other intense absorption bands, for instance the ones associated to O-H stretching of water. In deuterated water, the N-H group can exchange its proton with a deuterium atom (H/D exchange), thus downshifting the band.

- *Amide I:* The amide I band, typically positioned at around 1650 cm^{-1}, can be considered as the most important band in an FTIR spectrum of a protein. It is associated to the stretching of C=O bond, with contributions from CN stretching and NH bending (the latter making amide I band sensible to deuteration). Amide I band frequency and intensity is strongly dependent on the protein secondary structure. The different mechanisms through which the features of amide I are affected by the secondary structure can be summarized in three different phenomena: transition dipole coupling (TDC) [47], through-bond coupling [48] and hydrogen bonding. In particular, TDC mechanism is responsible of the very frequent splitting of the amide I band in two components. The position and intensity of these two splitted bands can be a tool for estimating the secondary motifs that are present in a protein [49].

- *Amide II:* At around 1550 cm^{-1}, the amide II band is an out-of-phase combination of NH bending and CN stretching vibration. The properties of amide II band are less straightforward related to the secondary arrangement of proteins than amide I band. However, some valuable characteristics of protein secondary structure can also be determined by amide II band analysis [50].

- *Amide III:* positioned in the range between 1400 cm^{-1} and 1200 cm^{-1}, the amide III band is an in-phase combination of NH bending and CN stretching vibrations. This mode is rarely used in secondary structure determination since its absorption intensity is usually low, making difficult its identification. Nevertheless, some studies have shown the possibility of amide III analysis in order to estimate protein structure [51].

In addition to the IR absorption features of the protein backbone amide group, more absorption bands related to other chemical groups of the protein are shown in an IR experiment. These bands are originated from:

- *Side chains of aminoacids:* Several chemical functional groups such as C=C double bonds, C-O simple bonds, SH and CH groups that characterize the side chains of aminoacids give rise to specific IR bands that can be identified [42]. The analysis of side chain IR bands is usually performed in order to elucidate the catalytic activity of enzymes. In fact, side chains are often involved in the catalytic reaction mechanisms.

- *Water:* Water is essential for protein functions. It acts as solvent (for water-soluble proteins), as a reactant (in enzymes) and it is indispensable to stabilize the protein structure. Water can bind both the external surface and the internal parts of the protein, giving rise to specific bands in the IR spectrum. In detail, water presents three normal modes of vibration: two stretching normal modes (symmetrical and asymmetrical) and a bending normal mode [52]. At low wavenumbers, the bending vibration gives rise to a band centered at 1643 cm^{-1} (at 1209 cm^{-1} for D_2O). The symmetrical stretching vibration resonates at around 3450 cm^{-1} (at 2500 cm^{-1} for D_2O) and the asymmetrical stretching at 3600 cm^{-1} (2600 cm^{-1} for D_2O) [52]. In addition, other bands reflecting combinations of normal modes and overtones can appear in the spectrum. The wavenumbers just mentioned describe liquid pure water. However, when water interacts with the protein environment, it can easily change the position of its IR bands. Especially, the hydrogen bond network in which water molecules are involved with the protein chemical groups can affect the position of the bands. As a rule of thumb, H-bonds tend to lower the IR frequency of the stretching bands of water [42].

4.1.6 Interpretation of Difference Spectra

After inducing protein reactions, many bands in the difference spectrum can appear. The changes involving the conformational and chemical structure of proteins and cofactors after the reaction cause the appearance of difference IR bands. Among the large amount of information that a difference spectrum can contain, it usually difficult to ascribe every single IR signal to its corresponding chemical event and chemical group, thus making tougher the extraction of precious chemical information of the analyzed system form the IR difference spectra. Some methods have been developed in order to perform band assignment to the individual molecular groups of the protein. These methods include:

- *Spectra of model compounds:* Comparisons between the analyzed protein and other similar systems that have already been characterized can be considered as a starting point. In addition, the contributions of cofactors or substrates to the infrared difference spectra can be identified by comparisons with the corresponding isolated molecules.

- *Site-directed mutagenesis:* In principle, each component of the protein gives rise to a IR band. The complete elimination (or substitution) of a specific aminoacid (or sets of aminoacids) and other portions of the protein should have an effect on the difference spectra. The modified IR signals can be assigned to the mutated component.

- *Isotopic labeling:* This strategy can be considered as the most frequent and effective method in order to perform band assignment. Due to the mass effect on vibrational frequencies, infrared bands of labeled groups are shifted at different wavenumbers and can be identified in the spectrum. Ligands, cofactors and protein side chains as well as backbone groups can be labeled. The easiest way to perform isotopic labeling is H/D exchange: exchangeable protons are replaced by deuterons. This procedure can be achieved by putting the protein in an environment containing deuterated water. The groups that can exchange with deuterium, mainly the NH components of amide groups (that are solvent exposed), will give rise to bands shifted at lower wavenumbers.

- *Calculations:* Theoretical calculations based on the Density Functional Theory (DFT), Quantum Mechanics - Molecular Mechanics (QM/MM) and Normal Mode Analysis (NMA) are used to calculate the IR spectrum. Theoretical approaches are often coupled to the experimental above-mentioned strategies to strengthen the formulated hypothesis concerning protein mechanisms.

For DS-FTIR analysis on the photoactivation mechanism of OCP protein, the strategies adopted for band assignment consisted in H/D exchange (IR spectra were recorder in H_2O and in D_2O) and comparisons between infrared spectrum of the protein and of the isolated carotenoid pigment (cathaxanthin).

4.2 FTIR Analysis

In the following paragraphs, a description of the Difference Infrared Spectroscopy analysis on OCP photoactivation mechanism is presented. As previously mentioned in the introduction, attention was put in particular on the frequency region of the IR spectrum where stretching bands of water molecules appear, as one of the main objectives is to try to reveal putative internal water molecules that may participate in the activation cycle. Nevertheless, the simple absorption spectrum and difference spectra in the canonical frequency window from 1800 cm^{-1} to 1000 cm^{-1} will be reported.

4.2.1 Synthesis of OCP

Recombinant OCP from *Synechocystis* PCC 6803 reconstructed with canthaxanthin was provided by PhD student Silvia Leccese, who synthesized the protein following the protocol of Bourcier de Carbon *et al.* [14]. Stock solution of OCP 1.2 mg/mL (30 μM) in TRIS-NaCl buffer was used for all the analysis.

4.2.2 Sample Preparation

For normal FTIR absorption spectroscopy and for DS-FTIR spectroscopy, samples were prepared by putting 60 μL of stock OCP solution 30 μM on a CaF_2 circular window. Using a N_2 flux, the sample was dried in order to reach a mild/low hydration. This is because in a too wet sample the IR bands of the protein can be hidden by water bands, making normal FTIR and DS-FTIR analysis useless. At the same time, reducing the hydration level in a protein can affect its activity and stability. This is the case of OCP protein containing canthaxanthin, as studies suggest that self-activation of OCP(CAN) in a dry environment can easily occur even in darkness [53]. To have an idea of the hydration level of the protein, confrontations between amide I and amide II bands were done. Amide I band is superimposed with the bending normal mode of water, while amide II band is not. The higher the hydration level, the higher is the intensity difference between amide I and amide II. To make sure that the protein is not too dehydrated or too wet, the intensity of amide I and II were controlled. After several trials, suitable condition were reached.
After drying the sample, a second CaF_2 window was put on top of the first one and sealed with silicone grease to prevent sample leakage.

Hydrogen/Deuterium exchange was done following a protocol similar to the one proposed by Malferrari *et al.* [54]. The CaF_2 window holding the OCP solution was placed in the vicinity of a saturated solution of LiCl in D_2O (LiCl saturated solution ensures a relative humidity of 11 %) for one hour, closing the system under a sealed Petri dish. This ensures strong (but not complete) dehydration of the sample. The second step (rehydration with D_2O) was carried out placing the sample in the vicinity of a saturated solution of NaCl in D_2O (always under a sealed Petri dish) for two hours, ensuring a relative humidity of 75 %. Then, a second CaF_2 window was used to close the sample cell, sealing the system with silicone grease.

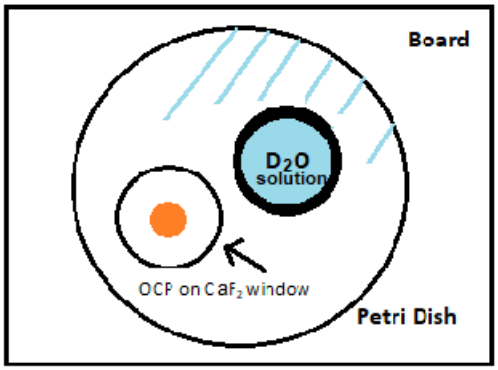

Figure 4.3: Schematic representation of the experimental setup for H/D exchange.

4.2.3 Instrumentation

FTIR analysis were performed using a Bruker Vertex80 FTIR spectrometer equipped with a photoconductive MCT detector cooled down with liquid N_2. A flow of N_2 was kept inside the spectrometer to get rid of gaseous substances (like CO_2 and H_2O vapors) inside the analysis chamber. The OPUS software was used to control data acquisition.

For static FTIR absorption spectroscopy, a first background spectrum of the void chamber was recorded. Then, the sample containing OCP protein in CaF_2 windows was placed inside the spectrometer chamber and the sample FTIR spectrum recorded. For both background and sample, 50 scans were accumulated and averaged.

For DS-FTIR, the sample was put inside the spectrometer and it was let to stabilize overnight. A first absorption spectrum was recorded as a background. Consequently, a blue LED light (λ = 475 nm) placed inside the FTIR chamber was switched on in order to induce protein reaction (conversion from OCP^O to OCP^R). Just after switching on the LED light, multiple spectra one after the other were recorded, thus applying the *rapid scan* technique in order to monitor the kinetic evolution of the system. Subtraction of the background form the recorded spectra under continuous illumination allows to obtain light-*minus*-dark DS-FTIR spectra. For the background, 2000 scans were averaged. For each spectrum showing the kinetics of photoactivation, 500 scans were recorded and averaged.

4.2.4 Static FTIR absorption spectra

FTIR analysis on OCP started with the collection of the normal absorption FTIR spectrum of the protein (Figure 4.5) in H_2O and in D_2O in its dark-adapted state OCP^O. Some typical prop-

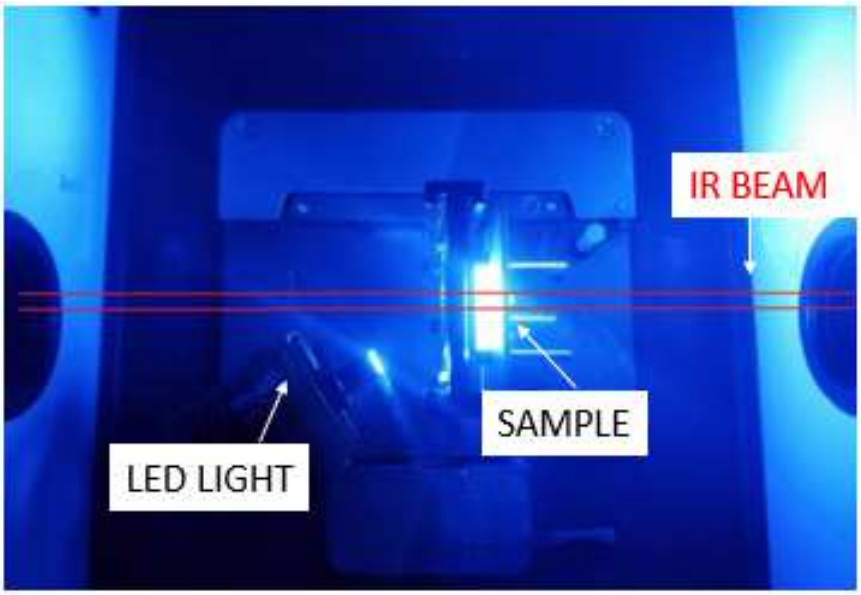

Figure 4.4: Experimental setup for DS-FTIR analysis.

erties of infrared spectra of proteins are straightforward recognizable. For the sample in normal water, a first broad band at 3400 cm^{-1} can be attributed to stretching of water molecules and OH and NH groups of the protein. At 1644 cm^{-1} and 1546 cm^{-1} amide I and amide II bands are respectively located. A small broad band at 2105 cm^{-1} can be associated to a combination band of water, even if some other contributions from the protein can be postulated.
For the sample analysed in D_2O, the same broad band at around 3400 cm^{-1} is shown. Contributions from OH and NH groups of the protein as well as residual H_2O molecules (as the complete substitution of H_2O with D_2O during the H/D exchange protocol is not guaranteed) are hypothesized. A strong absorption at 2513 cm^{-1}, that is absent in the first sample, is attributable to the downshifted D-H stretching of deuterated water. Another band related to vibrations of D_2O is the one at 1208 cm^{-1}, which can be related to the bending mode of D_2O. In normal H_2O the bending mode of water cannot be identified as it is superimposed with amide I. Last, amide I for the protein in D_2O is positioned almost at the same wavenumber of amide I in H_2O. Conversely, the band at 1455 cm^{-1} is associated to amide II, which is largely downshifted compared to the sample in normal water.
The preparation of the sample was set in order to have a maximum absorbance at around 0.8-0.9 for the stretching bands of water and at around 0.6 for the amide I band. These conditions are the most suited to perform subsequent efficient DS-FTIR measurements.

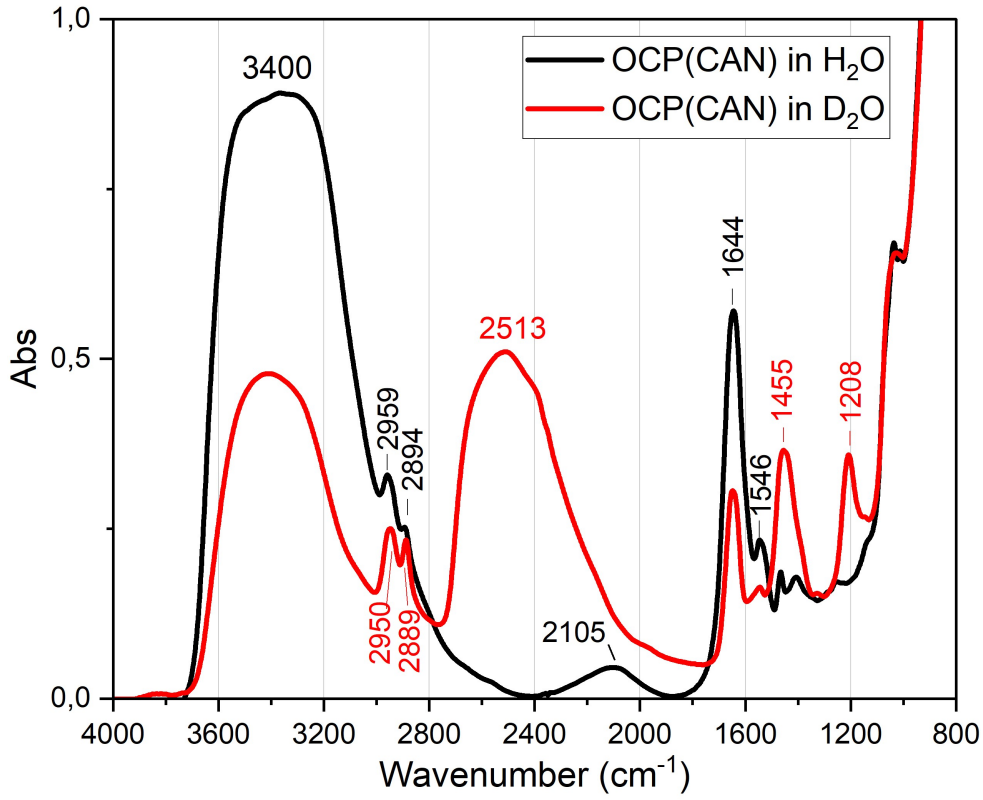

Figure 4.5: FTIR absorption spectra of OCP(CAN) in H_2O (black trace) and D_2O (red trace).

4.2.5 DS-FTIR spectra in the frequency window of 3800 - 2400 cm^{-1}

Light-*minus*-dark DS-FTIR analysis on OCP photoactivation was performed in order to try to identify the presence of putative internal water molecules that may participate during the activation mechanism of the protein. Previous studies by X-ray radiolytic labeling with mass spectrometry (XF-MS) in conjunction with small angle X-ray scattering (SAXS) performed by Gupta *et al.* [55] have suggested the possibility that some water molecules could effectively participate in the OCP^O-to-OCP^R transition. In particular, it was postulated that the conformational changes of the protein after photoactivation could be triggered by a signal propagation occurring from the light-activated carotenoid to the overall protein structure through an internal network of hydrogen bonds that involves also bound water molecules. This hypothesis led us to a difference FTIR measurement that could possibly detect signals of water molecules. The region of the spectrum that serves well for our objectives is the one at high frequencies, where the stretching normal modes of vibration of water are located. Analyzing this portion of the spectrum is strategic as there are not many other bands from the protein that could overlap with the desired signals. In fact, the analysis of the canonical region of the protein IR spectrum (1800-1000 cm^{-1}), where the bending modes of water are present, is not the most recommendable because of the presence of all the other bands arising from the protein structure.
The possibility of applying the above-mentioned strategy takes confirmation from studies performed on other protein systems, for example the light-induced proton pump bacteriorhodopsin

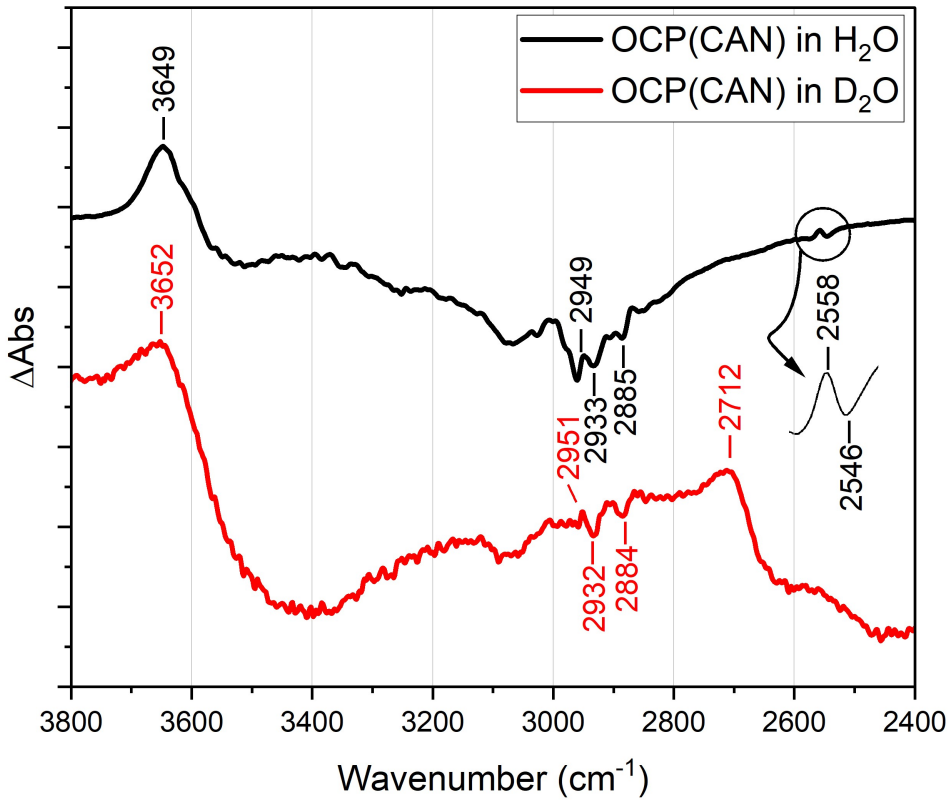

Figure 4.6: Light-*minus*-dark DS-FTIR spectra of OCP(CAN) in H_2O (black trace) and D_2O (red trace).

[56] or for the water-oxidizing complex of Photosystem II [57]. In both cases it was observed that the DS-FTIR investigation could detect stretching bands of internal water molecules at high frequencies, thus concluding that weakly H-bonded H_2O molecules participate actively in the reaction, changing their properties among protein activation and providing a path for signal propagation.

DS-FTIR spectra on OCP photoactivation are reported in Figure 4.6. For the sample in normal H_2O, a strong positive band at 3649 cm^{-1} appeared. The high frequency of this band could be associated to the stretching of weakly H-bonded water molecules. In fact, while liquid water (where H-bond networks are particularly strong) absorbs at 3600 and 3450 cm^{-1} for respectively asymmetrical and symmetrical stretching modes, water in vapor (where strong H-bonds are not present) shows the corresponding stretching modes at 3756 and 3652 cm^{-1} [58]. Thus, this comparison may led us to postulate that single or multiple water molecules weakly H-bonded to the protein are involved actively in the activation mechanism. To gain an ulterior proof for this band assignment, the deuterated sample was analyzed as well. Indeed, a positive band at 2712 cm^{-1}, which is not present in the sample in H_2O, appeared. This downshifted band can be similarly assigned to stretching vibrations of D-H bonds of deuterated water. Strikingly, the difference in frequency between the two stretching bands (about 937 cm^{-1}) is the same reported for the positive IR bands in H_2O and D_2O shown on the DS-FTIR analysis of Photosystem II in reference [57].

The deuterated OCP sample presents, although with a smaller intensity, a stretching band at 3652 cm^{-1}, which is very similar to the one at 3649 cm^{-1} of the first sample. This behavior can be justified considering the fact that a complete H/D exchange is not guaranteed and some residual H_2O molecules could still be located inside the protein.

Some other important features can be identified in the spectra. For example, the three bands at 2949 cm^{-1}, 2933 cm^{-1} and 2885 cm^{-1}, which do not change much in the deuterated sample (2951 cm^{-1}, 2932 cm^{-1} and 2884 cm^{-1} respectively) can be assigned mainly to stretching modes of the CH groups of the protein. These frequencies do not shift after deuteration because CH groups are not exchangeable. The small differences can be explained considering experimental uncertainty and instrumental errors.

The very small positive and negative bands at 2558 cm^{-1} and 2546 cm^{-1} can be assigned to stretching modes of SH groups, as the protein contains at least 4 residues of cysteine. These bands disappear in the deuterated sample, taking us to consider that SH groups might exchange with deuterium. The fact that no downshifted bands were identifiable (at around 1850 cm^{-1} where S-D stretching resonates [42]) can be justified considering that the S-D stretching could have a very limited intensity and thus making the bands indistinguishable from the background.

Overall, the DS-FTIR analysis seemed to be successful. Identification of stretching bands of water molecules participating in the activation process of OCP was achieved, validating our hypothesis and objectives. However, the results reached in this analysis present some limits.

In particular, even if a strong confirmation of the involvement of internal water molecules in the photocycle was obtained, no more information can be extrapolated from the analysis. The detailed mechanism explaining how water molecules are actually contributing to the reaction is still missing.

4.2.6 DS-FTIR spectra in the frequency window of 1800 - 1000 cm^{-1}

Chemical changes of the protein during photoactivation can be monitored especially in the canonical frequency portion of the IR spectrum from 1800 cm^{-1} to 1000 cm^{-1}. In this region, bands arising in the difference spectrum reflect chemical and structural modifications of OCP, including conformational changes of the overall three-dimensional arrangement of the backbone as well as modifications and displacements of the internal carotenoid molecule, moving inside the protein during the photocycle. The kinetic evolution of the system under continuous illumination for OCP in H_2O and D_2O is reported in Figure 4.7. Each sets of spectra show that the spectral shape does not evolve: indeed the same kinetic is observed for all bands, confirming that the reaction mechanism takes place in synchronicity (within the time resolution of the technique) in both samples. It should be noticed that time resolution is not very high, as each spectrum is recorded every 30 seconds. This is because OCP has a very low yield of photoactivation (less than 1%, as previously mentioned), thus making the accumulation of OCP^R relatively slow. In addition, the blue LED light used to induce protein reaction is not so intense. As a consequence, in order to gain strong signals clearly distinguishable from the background, a few seconds need to be waited, lowering time resolution.

By analyzing the growth of positive and negative bands in the difference spectrum, it is possible to evaluate some properties of the activation mechanism. All the bands seem to raise in a synchronized way, without identification of any bands that increase in a spectrum and then decrease in the following one. One of the main information that can be deduced from this kinetic evaluation is that the activation mechanism takes place in a single step way, without formation of any intermediate species, at least in the time resolution of the experiment. As also found

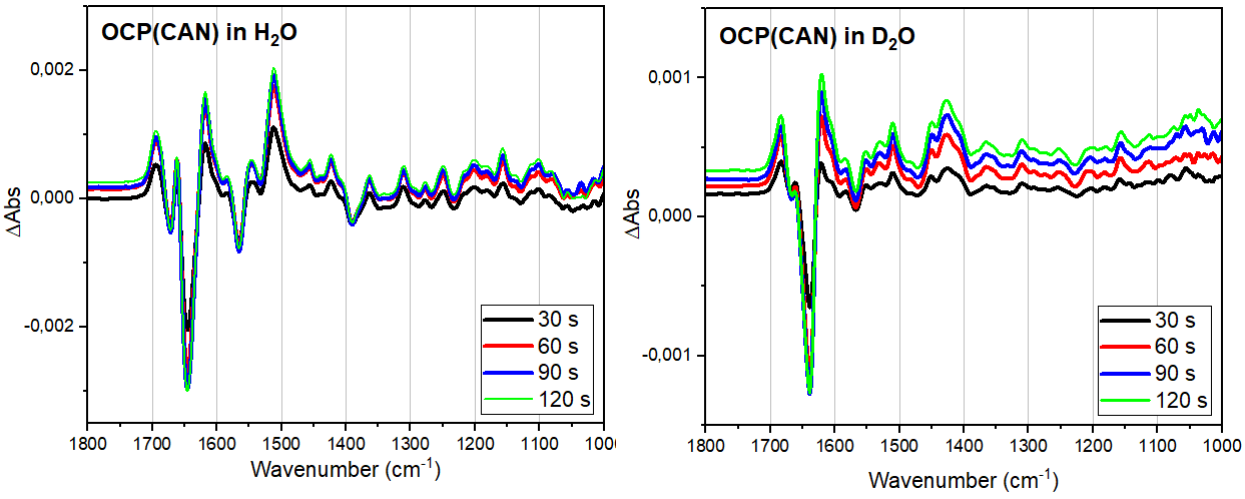

Figure 4.7: DS-FTIR spectra of OCP(CAN) in H_2O (black trace) and D_2O (red trace) at different times.

by other studies (for example the one in reference [59]), we witnessed a concerted process of photoactivation where no metastable structures are accumulated and then dissipated to reach OCP^R.

A clearer comparison between the analysis in H_2O and D_2O is shown in Figure 4.8, where all the frequencies of the most intense bands are reported. To shed light on the activation mechanism, the position of each band must be analyzed, identifying the bands that downshift their frequency in the deuterated sample from the ones that do not shift. Peaks that lower their frequency are related to vibrations of chemical groups of the protein that can exchange with deuterium. These chemical groups are most likely placed in positions of the protein that are solvent accessible. Conversely, components of the protein that do not exchange with deuterium tend to maintain the same frequency. These parts include chemical groups where the H atom is not exchangeable due to chemical reasons (for example a very high pKa) or because it is not solvent exposed.

Previous DS-FTIR studies on wilde type and mutant OCP [27] could assign the very intense negative band at 1645 cm^{-1} (1639 cm^{-1} in D_2O) to an unfolding of a solvent exposed secondary motif, most likely the α-helices composing the NTE and/or CTT. Without additional experiments on OCP mutants, no other assignments of the protein secondary structure can be safely made.

Identification of the carotenoid bands is another important step in order to elucidate the photocycle. It is known that upon photoactivation the carotenoid translocates inside the NTD, thus changing its chemical environment and also chemical structure (as it is proposed that the

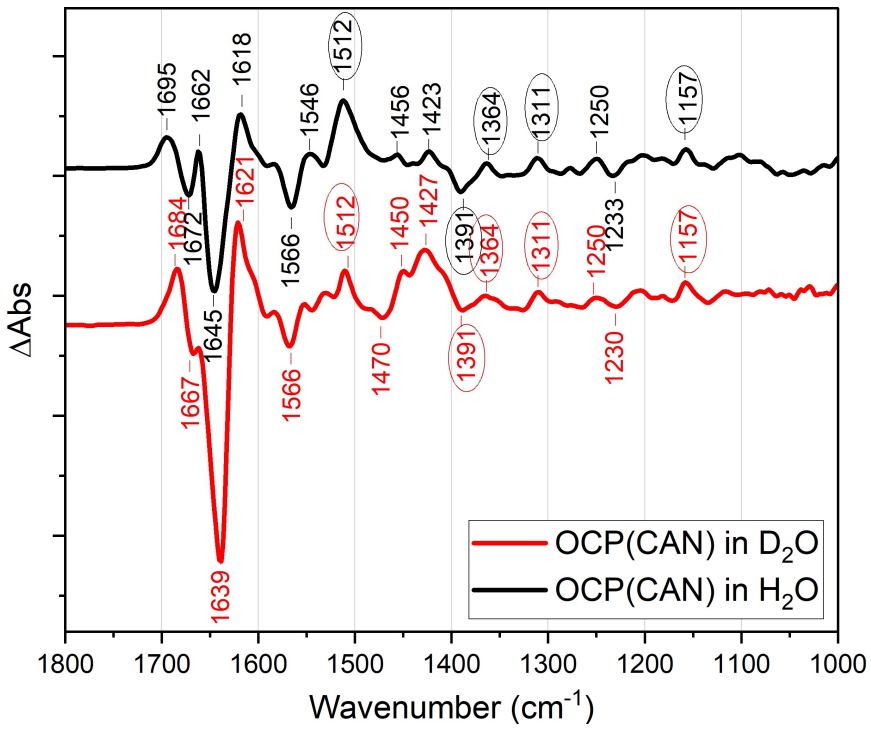

Figure 4.8: DS-FTIR spectra of OCP(CAN) in H_2O (black trace) and D_2O (red trace). Conserved frequencies assigned to the carotenoid molecule after H/D exchange are circled.

carotenoid in OCP^R presents a more rigid and planar geometry in comparison with OCP^O [23]). These modifications should then appear as signals in the difference spectrum. Band assignment of carotenoid molecule canthaxanthin was carried out applying two strategies: first, canthaxanthin does not present any chemical groups exchangeable with deuterium. This means that a putative carotenoid band in the difference IR spectrum must not shift in frequency after deuteration. Secondly, a comparison between the static IR absorption spectrum of isolated canthaxanthin can be executed in order to identify the signals of the DS-FTIR measurements that correspond to the carotenoid. Putting together these requirements, a putative band assignment for the internal canthaxanthin molecule has been made: signals at 1512 cm^{-1} , 1391 cm^{-1}, 1364 cm^{-1}, 1311 cm^{-1} and 1157 cm^{-1} have been identified supposedly as carotenoid bands. Identification of carotenoid bands is a mandatory preliminary step for more detailed experiments. A more precise band assignment will require advanced computational studies taking into account the effect of the protein binding pocket in both the orange and red states of OCP.

To summarize, DS-FTIR analysis of the 1800-1000 cm^{-1} region led us to elucidate some characteristics of the activation mechanism of OCP, in particular confirming that the photocycle proceeds as a single-step synchronized process without formation of long-lived intermediates. Furthermore, we have identified putative bands for the carotenoid molecule in both orange and red states of OCP.

5

OCP Adsorption on SBA-15-NH_2 Nanoparticles

Entrapment of proteins and enzymes in solid structures has been a field of interest largely investigated by researchers over the past decades [60, 61]. Among all the different varieties of solid substances that have been studied for protein encapsulation, structured inorganic materials have always been considered of great interest. Their advantageous properties, such as the possibility to regulate pore sizes, pore volumes and surface areas in a highly reproducible way, make these materials a very reliable system for applications involving proteins and enzymes. A wide range of biotechnological applications like biocatalysis, sensoring, nanomedicine and tissue engineering can all benefit of protein immobilization on solid surfaces. These uses strongly depend on the extent of protein adsorption, whose uptake capacity is usually regulated by the relation between protein and pore dimensions as well as the specific intermolecular interactions occurring within the solid material and protein.
Mesoporous materials, that are a specific class of materials containing pores with diameters between 2 nm and 50 nm, have been extensively used for protein loading as their pore sizes are compatible with the protein dimensions for an effective adsorption [62]. Among them, mesoporous silica nanoparticles (MSNs) really stood up for applications in protein and enzyme immobilization and drug delivery [63]. They feature high surface areas with large pore volumes, uniform and tunable pore sizes and stable frameworks. In addition, the easy synthesis method and the possibility to functionalize the surfaces with different functional groups have made these materials substantially useful for several purposes.
In this chapter, a description of Orange Carotenoid Protein adsorption on MSNs will be presented. SBA-15 mesoporous nanoparticles functionalized with amine groups (SBA-15-NH_2) have been chosen as our inorganic support for OCP immobilization in order to create a photochromic nanosystem that can be used for subsequent development of tunable fluorescent devices (described in Chapter 6).

5.1 SBA-15 nanoparticles: general properties

SBA-15 (Santa Barbara Amorphous) nanoparticles consist in a mesostructured nanomaterial synthesized for the first time in 1998 [64]. At the microscopic level SBA-15 is composed of well-ordered hexagonal two-dimensional mesophases (p6mm space group) with uniform pore

sizes (up to 30 nm depending on the synthesis) and high stability in water and in most organic solvents. SBA-15 has been applied in catalysis, water treatments and in analytical chemistry [65]. Its biocompatibility suggests also multiple applications in bio-imaging, biomedical and therapeutic/diagnostic applications [66].
Synthesis of SBA-15 nanoparticles has been studied and reviewed [67]. The reaction mechanism is classified as a cooperative self-assembly process which begins with the preparation of a supramolecular self-assembly of surfactants (template). This is usually achieved adding anionic, cationic or nonionic surfactants (for example nonionic Pluronic P123 copolymer) in water under acidic conditions, resulting in the formation of micelles. Subsequently, a silica source acting as a precursor is added to the surfactant system. The silica precursor adsorbs on the micelles surfaces and starts to polymerize, creating a silica framework which eventually precipitates. More in detail, five stages have been identified during SBA-15 self-assembly cooperative synthesis mechanism [68]. First, the hydrolysis of the silica precursors (usually organic silicates, like TEOS) occurs. As a second step, the hydrolyzed silicates adsorb on micelles surfaces and start to polymerize. This process may influence the stability of micelles, which could elongate and assume a rod-like shape. Subsequently, micelles start to associate, creating large flocs (third step) which then precipitate (fourth step). During the last step, an internal rearrangement involving micelle-micelle coalescence initiates, forming cylindrical aggregates. The obtained reaction product is then calcinated in order to eliminate the surfactants. The final material consists of elongated rod-shaped nanoparticles presenting internal linear cylindrical channels organized in a hexagonal geometry. The nanoparticle dimensions and the diameter of the mesopores is mainly influenced by temperature and by the stechiometric ratio between the surfactant and the silica source. In this way, by regulating the experimental conditions of reaction it is possible to select the morphological properties of the final nanoparticles.

Functionalization of SBA-15 nanoparticles with different groups like thiol, phenyl, nitrile, halide and amine chemical groups has been reported [70]. Functionalization is a general procedure that is performed with the main purpose of enhancing the stability of the solid system and increasing the affinity between the surface of the material and the molecules that are meant to be adsorbed. In addition, covalent immobilization of molecules and proteins on the solid system usually necessitates functionalization with proper reactive chemical groups.

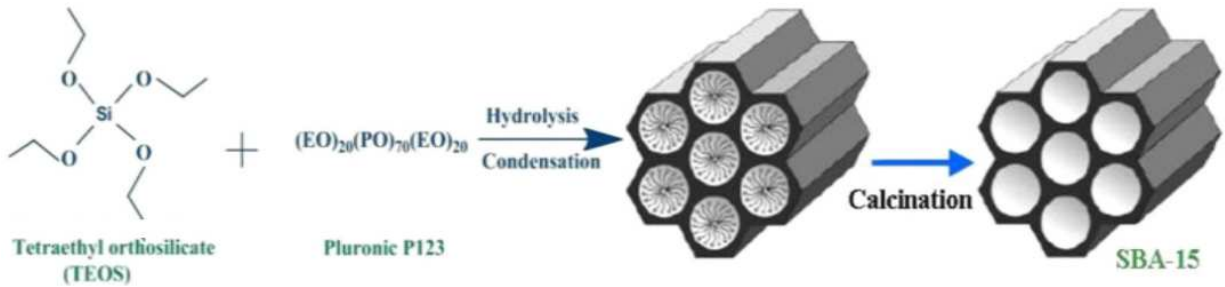

Figure 5.1: Scheme of SBA-15 synthesis and structure. Image taken from reference [69].

Functionalization of SBA-15 nanoparticles can be performed in two different methods: co-condensation (direct synthesis) or post-modification (grafting) [71]. The first method allows surface functionalization through a single step process concomitant with the nanoparticle synthesis. In this case a "one pot" reaction is sufficient, where the molecules that act as precursors for SBA-15 nanoparticles react during an individual step with some additives that provide the specific functionalizing chemical group. Instead, the grafting protocol consists in a post-functionalization of the material surface where the new chemical groups are inserted during a synthetic second step that takes place after the actual nanoparticle synthesis.
For OCP adsorption we have used SBA-15 nanoparticles functionalized with amine groups. Functionalization took place by grafting method using the APTES molecule as a grafting agent.

The most useful characterization methods for SBA-15 nanoparticles consist in SEM and TEM microscopy, which allow to describe the morphology of the material at different dimensional scales. Nitrogen physisorption analysis is also very common in order to determine the surface areas and the pore size distributions. X-ray diffraction is widely applied to investigate structural properties like the order and unit cell parameters. Other complementary characterization techniques include FTIR spectroscopy, thermogravimetric analysis (TGA) and determination of the point of zero charge (PZC).

5.2 Protein adsorption on silica particles

Immobilization of proteins and enzymes in solid mesoporous matrices provides beneficial outcomes depending on the specific application. In enzymatic systems, the entrapment inside a solid nanoscale scaffold allows protection and stabilization of the enzyme against high temperatures, organic solvents and mechanical treatments. Furthermore, the possibility to easily separate and recover the system for reuse while maintaining activity is a great advantage in catalysis. Also proteins in solid materials found their way in different application fields, for

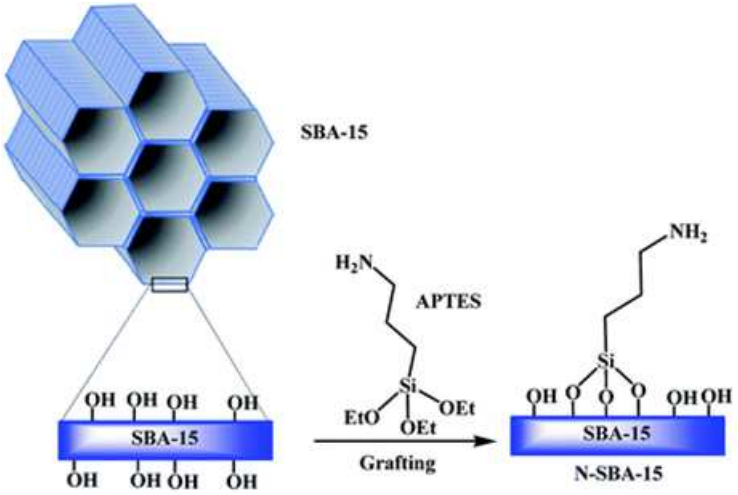

Figure 5.2: Scheme of SBA-15 amine functionalization by grafting method.

example in biosensors and for biomedical systems. The most intuitive and easy way to perform immobilization of proteins in mesoporous materials is by simple adsorption. The favorable intermolecular interactions between the protein and the material allow efficient adsorption on the external surface of the matrices and also inside their pores. Different factors related to the specific properties of the material and the protein can all influence the adsorption capacity [72]:

- *Relative size between proteins and pores:* Mesoporous well-structured materials present abundant internal surface areas and volumes that can host proteins. However, if the protein dimensions are too large compared to pore diameters, there is no access to the internal surfaces and the protein will adsorb only on the external surfaces, thus remaining exposed to the environment. So, an intuitive effective approach for the selection of a mesoporous material for high protein immobilization involves the correspondence between the pore diameter and the hydrodynamic dimensions of the protein. There are still some debates regarding whether the pores should have consistently bigger dimensions or if a similar matching size between pores and proteins is more convenient.

- *Particle morphology:* Other morphological properties, for example pore volumes and the length of pore channels can influence protein loading. In particular, due to the effect of pore blocking by protein, different materials with the same pore volumes will show higher immobilization efficiency when the length of the pore channels is lower.

- *Isoelectric points:* Depending on the pH of the protein buffer solution where the mesoporous nanoparticles are suspended, the electrical charge of the material and of the protein will adjust according to the corresponding isoelectric points. Effective protein adsoption occurs when opposite charges on the material and protein surface will match. As a general rule, efficient adsorption is usually guaranteed if the pH value of the buffer is below the pI of the enzyme and above that of the support (or viceversa).

- *Functionalization:* If the surface properties of the solid material are not convenient for protein adsorption, functionalization with selected chemical groups can be applied as previously mentioned.

- *Other:* Some experimental conditions, like the initial protein concentration, the nanoparticle concentration in the suspension, the temperature and the incubation time can all largely influence the protein uptake.

5.2.1 OCP adsorption

Several studies on Orange Carotenoid Protein adsorption on SBA-15 and SBA-15-NH_2 nanoparticles have been performed by Leccese *et al.* [73]. The influence of nanoparticle pore sizes, amine functionalization and initial concentration have been investigated in order to assess the

effect on the immobilization efficiency. Two different proteins, OCP reconstructed with echinenone, OCP(ECN), and OCP reconstructed with canthaxanthin, OCP(CAN) have been used. The main results are here summarized:

1. The kinetic analysis on the adsorption process showed that the immobilization equilibrium is reached after 4 hours of incubation of the nanoparticles inside the OCP solution, without any particular differences regarding the initial OCP concentration or the internal carotenoid molecule.

2. The maximum protein uptake from mesoporous nanoparticles has been shown for unfunctionalized SBA-15 under high initial concentrations (2 mg/mL) of OCP(CAN). The reached protein loading in these conditions has been of 52 mg of protein every 1 g of SBA-15.

3. Studying the immobilization efficiency of OCP(CAN) and OCP(ECN) at lower initial concentration (0.2 mg/mL), some interesting observation have been made. First, comparisons on the protein uptake between unfunctionalized SBA-15 and functionalized SBA-15-NH_2 prove that a better protein adsorption occurs using SBA-15-NH_2 nanoparticles (keeping constant nanoparticle pore sizes). In this case, the chemical environment provided by amine groups is more compatible with the protein surface, causing an increased protein uptake. Comparisons of the protein immobilization efficiencies while changing the pore sizes (but not the functionalization) indicate that a better protein loading is generally (but not in all cases) reached when nanoparticles with bigger pores are used.

4. Protein loading is also influenced by OCP photoactivation. Strikingly, OCP activated with a blue LED light increases its ability to adsorb on mesoporous nanoparticles. This event has been justified considering the fact that photoactivated OCP presents a more elongated conformation which can eventually penetrate the SBA-15 channels and adapt to the pore morphology in a better way.

5.3 Synthesis of SBA-15 and SBA-15-NH_2

Hereafter, the synthesis protocols that have been adopted for SBA-15 and SBA-15-NH_2 are reported.

5.3.1 SBA-15

SBA-15 was synthesized as described in the literature. Summarizing, 8.02 g of triblock copolymer Pluronic P123 ($(EO)_{20}(PO)_{70}(EO)_{20}$; Aldrich) acting as directing agent were mixed under stirring with 280 mL of HCl 0.1 M for 2 hours at 40°C until complete dissolution. After, 16.80 g of tetraethyl-orthosilicate (TEOS; Aldrich; 98%) as silica precursor were added drop by drop to the solution under slow stirring. The resulting suspension was stirred for 24 hours and then transferred into a 1 L glass bottle for a hydrothermal treatment at 80°C for 24 hours.

The temperature of the hydrothermal synthesis strongly affects the nano-porosity of the final nanoparticles. As a last step, the solid was filtrated and thoroughly washed with approximately 4 L of distilled water to remove the P123 polymer. The resulting powder was dried at 80°C overnight and calcined at 550°C (heating ramp: 0.4°C/min) for 6 hours under air to remove the template. Around 4 g of final SBA-15 material were obtained.

5.3.2 SBA-15-NH_2

Synthesis of SBA-15-NH_2 was performed as described in literature using a post-functionalizing grafting protocol. Starting SBA-15 nanoparticles were preliminary treated at high temperatures in order to dry the material and get rid of humidity. To do so, 1.2 g of SBA-15 were introduced in a cylindrical glass device under a 50 mL/min flow of gaseous argon. The thermal treatment consisted of 3 hours treatment at 50°C followed by a temperature increase (1.5°C/min ramp) until 350°C were reached. After 7 hours at 350°C, the sample was cooled down and 1.0 g of dry SBA-15 were introduced in a dried reactor equipped with a septum. After adding 50 mL of anhydrous toluene (VWR, 99.9%), the reactor was flushed with Ar and treated in ultrasonic bath for 30 seconds in order to create a uniform silica suspension. Subsequently, 1.0 mL of APTES (3-aminopropyltriethoxysilane; Aldrich; 99%) were added with a syringe and the reactor was placed in a thermostatic bath set at 166°C. Reflux was kept for 24 hours. The product was filtered, washed with 30 mL of toluene (VWR; 99.9%), 30 mL of acetonitrile (VWR; 99%) and 30 mL of ethanol (99%; Aldrich) and dried overnight at 60°C. As a last step, the SBA-15-NH_2 product was purified to remove the excess APTES: the nanoparticles were introduced in a cellulose cartridge and placed inside a Soxhlet apparatus. 125 mL of CH_2Cl_2 (Carlo Erba Reagents; 99.9%) were introduced in the flask connected to the Soxhlet apparatus and heated using a thermostatic bath set at 62°C. Reflux was kept for 24 hours. Lastly, the product was collected and dried at 60°C overnight. Around 0.7 g of SBA-15-NH_2 were obtained.

5.4 SBA-15 and SBA-15-NH_2 characterization

After nanoparticle synthesis, the products were characterized by TEM and SEM microscopy, thermogravimetric analysis (TGA) and by determination of the point of zero charge (PZC). Comparisons between SBA-15 and SBA-15-NH_2 are reported.

5.4.1 SEM and TEM microscopy analysis

Instrumentation:
Characterization by Scanning Electron Microscope (SEM) was performed using a SEM-FEG Hitachi SU-70 instrument operating at a working distance of 3 mm. The acceleration voltage was set at a low value of 2.0 kV: SBA-15 nanoparticles are not conductive materials and as a consequence the electron beam must not be too much energetic in order to avoid charge effects. Nanoparticles were deposited on a conductive carbon adhesive tape.

Analysis by High Resolution Transmission Electron Microscope (HRTEM) was performed us-

ing a JEOL JEM 1011 (W) microscope operating at 100 kV and equipped with an ORIUS Gatan Camera. Sample preparation consisted in the suspension of silica nanoparticles in ethanol followed by treatment in ultrasonic bath. A small drop of the suspension was deposited on a 3 mm copper grid coated with an amorphous carbon film. After letting the solvent evaporate for 1 hour, the sample can be analyzed.

Electronic microscopy images are reported in Figure 5.3. As expected, the typical morphology of SBA-15 nanoparticles is shown. Looking at the synthesized system at a larger scale, the one provided by SEM analysis, it is clear that the nanoparticles present a worm-like elongated shape characterized by a width of about 200-400 nm and a length of 1–2 μm. However, in the SEM images the typical mesostructured pores cannot be identified. TEM analysis provides high resolution images at the nanoscale level where the peculiar morphological properties can be recognized. In the TEM images the typical linear long channels organized in hexagonal structures are shown. It can be also observed that the overall crystalline structure of the nanoparticles is the same before and after functionalization by APTES molecules. This means that the functionalization step does not induce any modification of the mesostructure of silica support, thus making

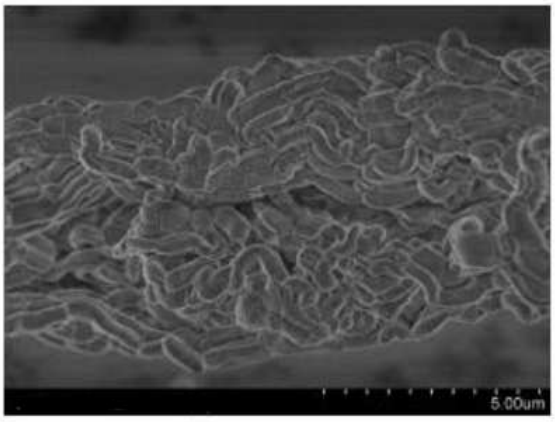

(a) SEM image of SBA-15

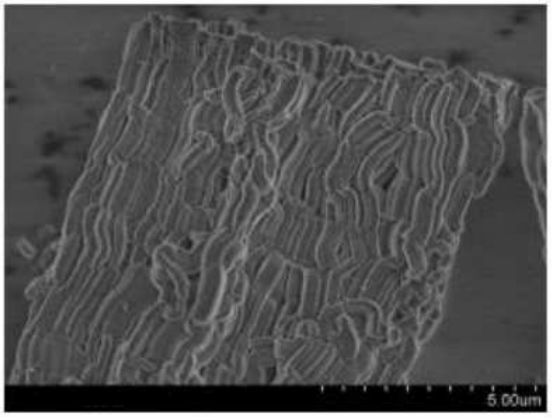

(b) SEM image of SBA-15-NH_2

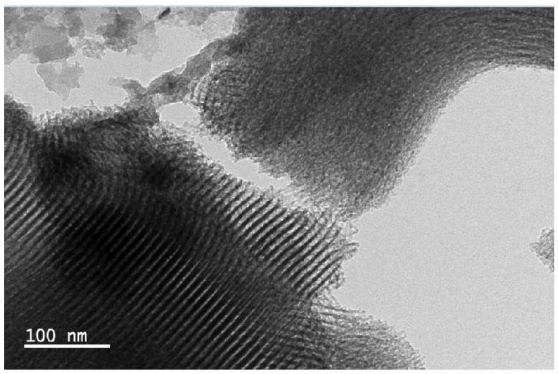

(c) TEM image of SBA-15

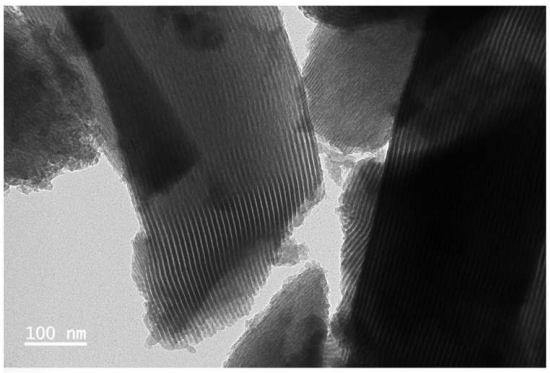

(d) TEM image of SBA-15-NH_2

Figure 5.3: SEM and TEM microscopy images of SBA-15 and SBA-15-NH_2 nanoparticles.

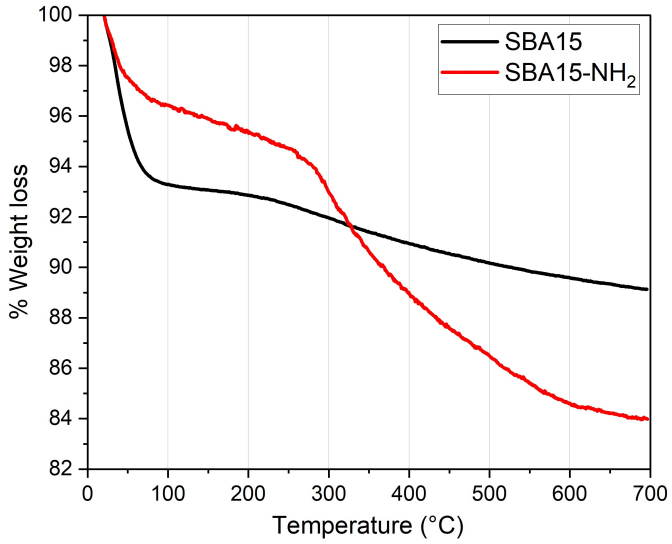

Figure 5.4: TGA analysis on SBA-15 (black trace) and SBA-15-NH_2 (red trace).

bare SBA-15 and functionalized SBA-15-NH_2 nanoparticles to be morphologically similar. For both SBA-15 and SBA-15-NH_2 it is possible to measure the pore dimensions from the TEM images. For the unfunctionalized SBA-15, pores of diameter around 5 nm are shown. Instead, the functionalized SBA-15-NH_2 presents pores with 4.5 nm diameters. This observation can be explained considering that the aminopropyl groups that functionalize the starting material fill up a portion of the available space inside the mesopores. The measured pore dimensions are compatible for OCP adsorption, as the protein in its monomeric form presents a smaller mean diameter (about 4 nm).

5.4.2 TGA analysis

Thermogravimetric analysis (TGA) is a common technique applied for determination of weight loss during a thermal treatment of a material. Several properties can be defined using this method. In this case, the quantification of the number of functionalizing organic moieties grafted on SBA-15-NH_2 can be calculated by TGA [71].

Instrumentation:
TGA analysis was performed on STD Q600 thermobalance (TA Instrument). The weight loss was measured while heating from 25 °C to 700°C (heating rate 5°C/min) under air flow (100 mL/min). Initial masses of SBA-15 and SBA-15-NH_2 deposited inside the instrument were, respectively, 9.196 mg and 11.015 mg. The results are reported in Figure 5.4.

For normal SBA-15, the initial 7% loss of weight between 25°C and 90 °C can be justified considering desorption of water molecules from the material. After that, a 3% loss of weight occurs between 220°C and 700°C. This behavior can be explained taking into account the possibility that some residual molecules of the surfactant P123 copolymer, that were not fully eliminated during the calcination step of the synthesis, may be expelled during the TGA thermal treatment

at high temperatures by oxidation with the oxygen provided by the air flow.
For SBA-15-NH_2 an initial 4% loss of weight between 25°C and 100°C is due to elimination of water molecules (same behavior as normal SBA-15). Between 300°C and 700°C substantial 10% loss of weight is caused by the oxidation of the grafting aminopropyl groups. Starting from this piece of information and considering also the total surface area calculated by nitrogen physisorption analysis (see section 5.5.2) we can estimate the density of NH_2 groups grafted on SBA-15-NH_2 to 1.72 mmol/g (or 1.36 NH_2 groups/nm^2).

5.4.3 PZC determination

SBA-15 and SBA-15-NH_2 can assume different surface charges according to the environment in which they are inserted. As a matter of fact, both categories of synthesized nanoparticles show on their surfaces specific chemical groups that can be charged. Bare SBA-15 presents mainly OH chemical groups on its surface, which tend to deprotonate in water, leaving a negative charge density. Conversely, SBA-15-NH_2 is characterized by external NH_2 chemical groups that easily protonate in water, creating positive charges on the particle surface. In this sense, protonation/deprotonation equilibria depending on the pK_a of the chemical groups and on the pH of the water mixture in which nanoparticels are suspended strongly influence the surface charges. The characterization of the nanoparticle surface charges at different pH values of the suspension permits to evaluate in which conditions protein adsorption takes place, thus finding the best circumstances for efficient protein uptake.
This characterization is assessed by the determination of the Point of Zero Charge (PZC) [74]. A surface is at its PZC when the total surface charge density is zero. Similarly to the isoelectric point, the pH value of the water suspension at which the suspended nanoparticles present no surface charges can be considered as the PZC.
The state of surface charge can be evaluated by determination of the ζ-potential, which consists on the potential drop across the mobile part of the double layer of counterions that arranges around the charged particle. ζ is positive if the potential increases from the bulk of the liquid phase towards the interface. Measuring the ζ-potential at different pH values (and thus at different charge states of the particle surface) allows to get an overview of the surface charges at all the accessible pH conditions. The pH value at which ζ-potential tends to zero can be assigned as PZC.

Instrumentation:
ζ-potential measurements were performed using Litesizer500 (Anton Paar) instrumentation equipped with a Kalliope software. The principle of the measurement is based on the electrophoretic light scattering phenomenon, caused by the particle suspension, which is analyzed to determine the electrophoretic mobility (using the Smoluchowsky model) and the ζ-potential. Sample preparation was carried out as follows: initial dispersions of SBA-15 and SBA-15-NH_2 where prepared adding 0.01 g of nanoparticles in 25 mL of KNO_3 0.1 M solution and sonicat-

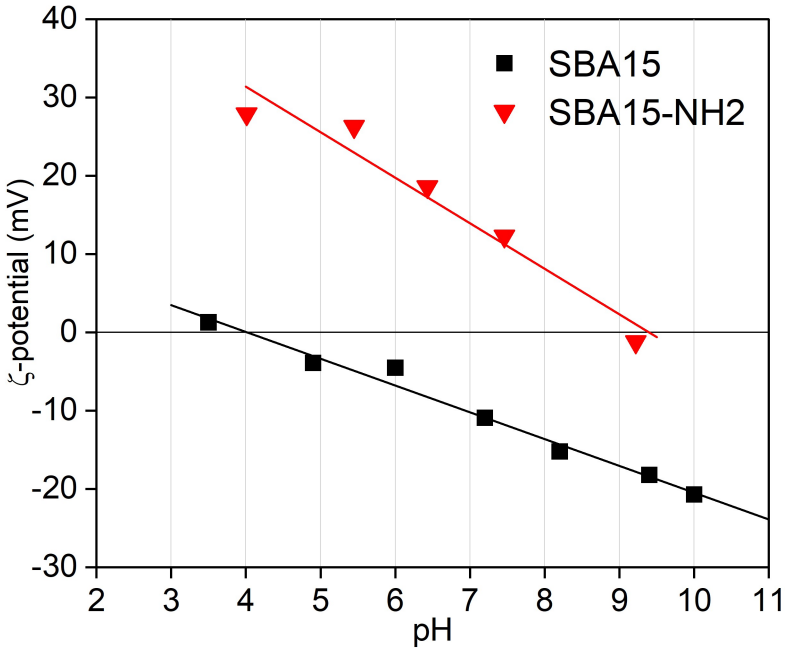

Figure 5.5: ζ-potential determination for SBA-15 (black trace) and SBA-15-NH_2 (red trace) at different pH values.

ing the system for 1 minute. By adding a few drops of HNO_3 0.1M or KOH 0.1 M the pH was adjusted ad different values (monitored with a pH-meter). At each pH value, determination of ζ-potential was performed. Results are reported in Figure 5.5.

Through the intersection between the fitting line and the base line at 0 mV it is possible to extrapolate the PZC value. For SBA-15, the PZC is at around 4.0, while for SBA-15-NH_2 PZC is set at 9.4. This behavior is logically acceptable. SBA-15 presents acidic OH groups on the nanoparticle surfaces that easily dissociate and charge negatively the particle. To reach a neutral charge density, the pH of the suspension must be pushed at low values, confirming a PZC at 4.0. For SBA-15-NH_2, amine groups present a certain degree of basicity which is at the base of the protonation equilibrium that charges positively the surface. To neutralize the surface, pH must be raised at basic values, and a PZC of 9.4 is found.
With the perspective of adsorbing OCP on silica surfaces, SBA-15-NH_2 seems to fulfill the requirements mentioned in Section 5.2. The adsorption protocol is performed at neutral pH (the one of the buffer solution in which OCP is stored) which happens to be in the middle between the isoelectric point of the protein (around 5.4) and the isoelectric point (PZC) of SBA-15-NH_2. In these conditions, the protein will present negative charges that will be attracted by the positive charges of the nanoparticles, and an efficient protein adsorption will take place.

5.5 OCP on SBA-15-NH_2

In order to create OCP-loaded nanoparticles as photochromic devices, a protocol for OCP adsorption on SBA-15-NH_2 was followed. Provided that PZC measurements confirmed that the chemical characteristics of particle and protein surfaces are matching, an efficient protein im-

mobilization is expected. After protein loading, the final product was analyzed by nitrogen physisorption and by solid state UV-Vis spectroscopy.

5.5.1 OCP adsorption protocol

10 mg of synthesized SBA-15-NH_2 nanoparticles were introduced in a 1.5 mL eppendorf test tube with 1.0 mL of OCP(CAN) solution 0.2 mg/mL. Incubation in dark under gentle agitation was kept for 4 h. This treatment ensures almost 100 % of protein immobilization efficiency as previously reported [73]. Incubation was followed by centrifugation at 8000 rpm for 20 minutes and the final precipitate was collected for further analysis.

5.5.2 Nitrogen physisorption analysis

Through N_2 physisorption [75], typical properties like pore size distribution, surface area and total pore volume could be investigated for SBA-15, SBA-15-NH_2 and SBA-15-NH_2 loaded with OCP. In order to register nitrogen physiorption isotherms, a degassing pre-treatment was applied to the samples: SBA-15 was dehydrated at 120°C overnight while for SBA-15-NH_2 and OCP loaded SBA-15-NH_2 a dehydration at 40°C for 30 minutes followed by a 60°C treatment for other 30 minutes under vacuum was used. The pre-treatment at low temperatures was chosen to prevent thermal degradation of the NH_2 groups and of OCP.

Instrumentation:
Nitrogen adsorption isotherms at -196°C were measured using a BELSORP max apparatus. The pore size distribution was calculated using the Barrett – Joyner – Halenda (BJH) method [76] applied to the desorption branch of the isotherm. Determination of specific surface area was obtained by application of Brunauer – Emmett – Teller (BET) model [77] from adsorption values at six relative pressures (p/p_0) ranging from 0.04 to 0.25. The total pore volume was determined from the amount of N_2 adsorbed at p/p_0= 0.975.

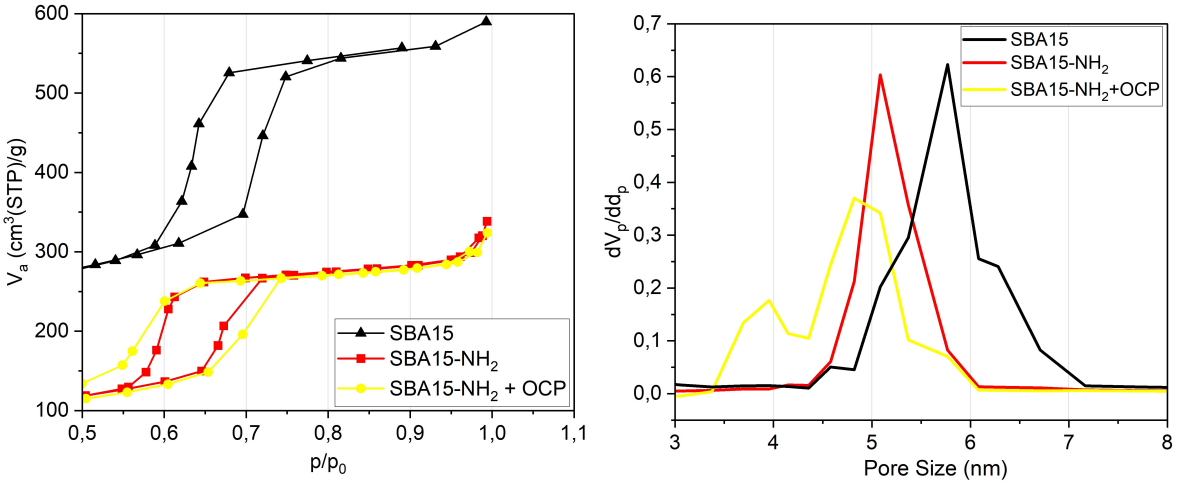

(a) Nitrogen physisorption isotherms (b) Pore size distribution

Figure 5.6: N_2 physisorption analysis on SBA-15, SBA-15-NH_2 and OCP loaded SBA-15-NH_2.

Table 5.1

	Mean pore diameter (nm)	Surface Area (m^2/g)	Pore Volume (cm^3/g)
SBA-15	5.8	759	0.90
SBA-15-NH_2	5.1	296	0.46
SBA-15-NH_2+ OCP	4.8	281	0.45

N_2 physisorption isoterms and pore size distributions are reported in Figure 5.6. All the properties calculated by N_2 physisorption are summarized in Table 5.1. Looking at the pore diameter distribution, SBA-15 presents pores with mean dimensions of 5.8 nm, in good agreement with the value of 5 nm found in TEM imaging. The pore dimensions are sequentially reduced after functionalization (5.1 nm, in agreement with 4.5 nm value for TEM imaging) and after adsorption of OCP. Intriguingly, the pore size distribution of OCP-loaded SBA-15-NH_2 presents an absolute maximum at 4.8 nm and a relative maximum at around 4.0 nm, thus creating two different populations. It can be hypothesized that the dimensional family of 4.0 nm might be related to pores filled with OCP, as the protein occupies some of the available space comprised in the porous channels of SBA-15-NH_2. This is a possible indirect evidence that OCP adsorbs not only on the nanoparticle surface but also inside the pores. This observation can also be justified by the slight decrease of total pore volume between SBA-15-NH_2 and OCP-loaded SBA-15-NH_2. Surface areas calculated by BET method are very extended, as it is usually found in mesoporous materials. These values were used to calculate the numeric density of NH_2 groups grafted on SBA-15-NH_2 (see section 5.4.2).

5.5.3 UV-Vis spectroscopy analysis

In order to evaluate the spectral properties of OCP(CAN) adsorbed on SBA-15-NH_2, solid state UV-Vis spectroscopy was applied on the system. OCP(CAN) presents an internal canthaxanthin molecule which strongly absorbs incident blue/green light and causes photoactivation of the protein from OCP^O to OCP^R. The dark-adapted state and the photoactivated state of OCP show different absorption spectra in which OCP^R presents a red-shifted maximum in comparison with OCP^O. The photoactivation process of OCP was monitored on loaded SBA-15-NH_2 to determine if a correct activation and back-conversion of the protein can occur also inside the silica matrices.

Instrumentation:
Solid state UV-Vis spectra of SBA-15-NH_2 loaded with OCP(CAN) were recorded on a Varian 2300 UV-Vis spectrophotometer equipped with an integrating sphere and using a resolution of 1 nm and an acquisition time of 0.1 s per point. The total diffused reflectance recorded by the integrating sphere was converted automatically by the Scan software into absorption spec-

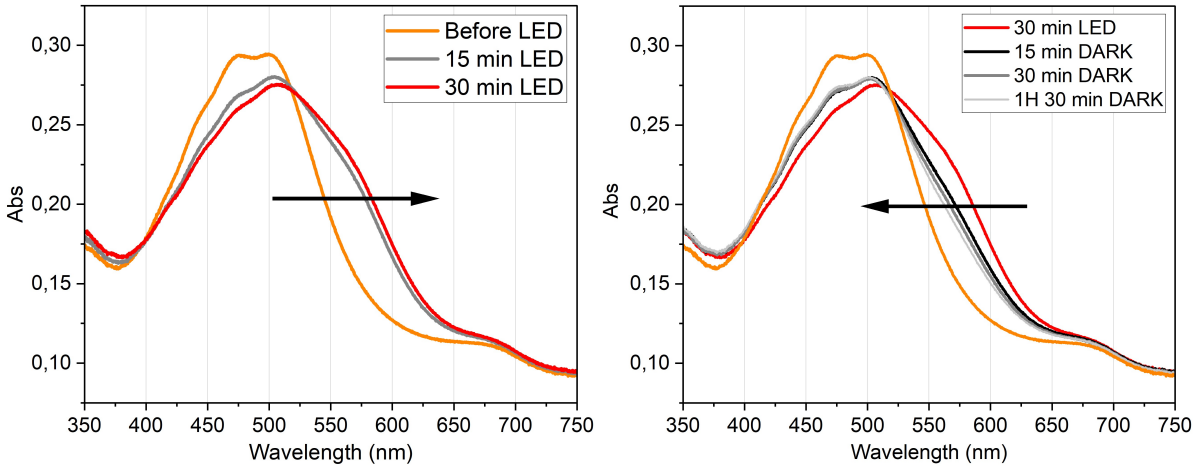

(a) OCP activation kinetics during blue LED light exposure

(b) OCP back-conversion kinetics in dark

Figure 5.7: Kinetics of photoactivation and back-conversion of OCP(CAN) adsorbed on SBA-15-NH_2

tra through Kubelka-Munk approach [78]. Sample preparation follows the same steps reported in section 5.5.1. The collected nanoparticles were placed in the spectrometer sample holder and analyzed. By using a blue LED light, photoactivation was induced directly in the sample holder. Nanoparticles were not fully dried after OCP adsorption as dehydration can affect negatively the photoactivation process. The kinetic evolution of the system under LED light and the back-conversion process are reported in Figure 5.7.

UV-Vis analysis confirms that the photoactivation process is effective also in SBA-15-NH_2. Before exposing the system to the blue LED light, the typical absorption spectrum of OCP(CAN) is shown, characterized by an absorption maximum at around 480 nm and by the presence of a vibronic progression. After switching on the LED light, photoactivation of the protein occurs, as evidenced by the red-shifting behavior of the absorption curve. After 30 minutes of exposure, no more changes are detected on the spectrum. It can be concluded that during the process a large number of OCP molecules convert from OCP^O to OCP^R. However, not all the proteins adsorbed on silica converted, as some features of the OCP^O state (the vibronic bands) are still slightly identifiable. After letting the sample rest in the dark, an almost complete back-conversion of the system from the activated state to the dark-adapted state is shown, as proved by the UV-Vis spectra. Overall, it can be stated that OCP photoactivation and back-conversion mechanisms are still present even when the protein is adsorbed on silica matrices, and that the processes are reversible. Furthermore, in order to change its state, OCP needs to modify its conformational structure. As the photoactivation mechanism is observed, it can be affirmed that SBA-15-NH_2 environment does not particularly perturb the protein and does not provide much constraints for the protein to change its structure and adapt to the new conformation.
Provided that OCP spectral properties are maintained, the application of this system for the development of fluorescent tunable nanoparticles can proceed, as described in Chapter 6.

6

OCP-loaded Fluorescent SBA-15-NH_2 Nanoparticles

In this chapter, the development of photo-tunable silica SBA-15-NH_2 fluorescent nanoparticles will be described. This work was inspired by the research project of Andreoni *et al.* [39] who designed a three-strand DNA junction, incorporating OCP and different fluorophores, following the idea of creating photonic systems that could be applied in artificial photosynthesis or as starting point for the development of complex photonic networks. Our intentions were to apply the properties found on Andreoni's system in a similar way also on silica SBA-15-NH_2 solid nanoparticles, with the perspective of possible applications in fluorescence imaging.
The spectral features of OCP photoactivation, namely the spectral red-shift of the Vis absorption spectrum during photoconversion from OCP^O to OCP^R, could be used as a tool to produce tunable fluorescent nanoparticles. OCP loaded on SBA-15-NH_2 does not have any detectable fluorescence yield, so the adsorption of different fluorophores like Cyanine 3 (Cy3), Cyanine 5 (Cy5) and 3-Hydroxyflavone (3HF) together with OCP was envisaged for our purposes. For all systems, OCP absorption spectrum in its activated state, OCP^R, overlaps with the emission spectrum of the fluorophores. In this way, hypothesizing an energy transfer from the fluorophore to the internal OCP carotenoid, the fluorescence emission of the fluorophore can be partially quenched. By photoactivating OCP at different stages, a modulation of the energy transfer between the molecules was found, thus creating fluorescent SBA-15-NH_2 nanoparticles equipped with a system of regulation of their emission intensity.
In the following sections, two different systems containing either Cy3:Cy5 or 3HF adsorbed on SBA-15-NH_2 in presence of OCP will be described.

6.1 Cy3:Cy5 system

Cyanines are organic dyes usually classified in two main categories: naturally occurring cyanine dyes (vegetable source) and pure synthetic cyanine dyes (chemical source) with the general formula $R_2N[CH{=}CH]_nCH{=}N^+R_2$ [79]. The chemical structure of cyanines consists typically in two heterocyclic rings containing an atom of nitrogen and connected together by a long conjugated chain. The actual electronic structure is a hybrid of resonance between two different resonance structures which delocalize a positive charge across the unsaturated chain. The length of the conjugated system affects the spectral absorption and emission properties of cya-

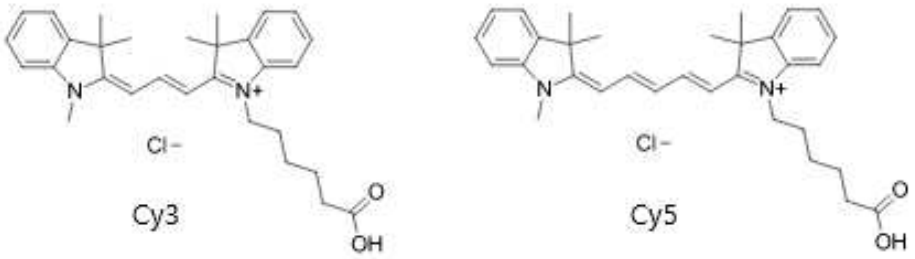

Figure 6.1: Chemical structures of Cyanine 3 (Cy3) and Cyanine 5 (Cy5) carboxylic acids.

nines, which can be tuned according to the number of methine groups forming the central chain. Overall, cyanines differ from each other according to the number of atoms composing the connecting chain, the presence of substituents and the structure of the heterocyclic moiety. The high molar extinction coefficient permits to perform spectroscopic experiment using moderate concentrations.

The molecules that have been used for our studies are cyanine carboxylic acids Cy3 and Cy5 (Figure 6.1). The two dyes present a different number of carbon atoms composing the linking chain. While Cy3 has three carbon atoms in the chain, Cy5 has two additional carbon atoms which create one more double bond in the conjugated structure. These properties reflect the different spectral absorption and emission responses of Cy3 and Cy5. Indeed, Cy3 appears as a red powder which dissolves in water to create a magenta solution. The absorption spectrum consists of two maxima at around 511 nm and 543 nm while the emission peak is at 557 nm. Differently, Cy5 presents itself as a dark blue powder which creates a light-blue water solution showing absorption maxima at 594 nm and 639 nm and an emission maximum at 660 nm (Figure 6.2). Cyanines are known as an efficient FRET couple [80]. In fact, the emission spectrum of Cy3 is superimposed with the absorption spectrum of Cy5. This means that if some conditions are verified, in particular a short distance between the molecules and a correct relative orientation, the excitation energy of Cy3 can be transferred to Cy5. As a consequence, while illuminating the system at the absorption maximum of Cy3, a reduced fluorescence from Cy3 and an enhanced fluorescence from Cy5 should be detected.

SBA-15-NH_2 does not have any chemical groups that can emit visible light. In order to obtain a fluorescent system, we have developed a protocol for Cy3 and Cy5 adsorption on SBA-15-NH_2. First, an analysis of the actual possibility that Cy3 and Cy5 could be adsorbed on the solid support was performed. The amount of adsorbed Cy3 and Cy5 on SBA-15-NH_2 was monitored at different times of incubation in order to assess the affinity of the molecules towards the silica support (Paragraph 6.1.1). After that, absorption and emission spectroscopy analysis on SBA-15-NH_2 loaded with Cy3 and Cy5 was applied to define the effect of the solid matrix on the spectral features of the fluorophores (Paragraph 6.1.2). Next, after verifying that Cy3 and Cy5 can be adsorbed on SBA-15-NH_2, a protocol to adsorb the two fluorophores and OCP protein at the same time on the silica support was followed (Paragraph 6.1.3). In this

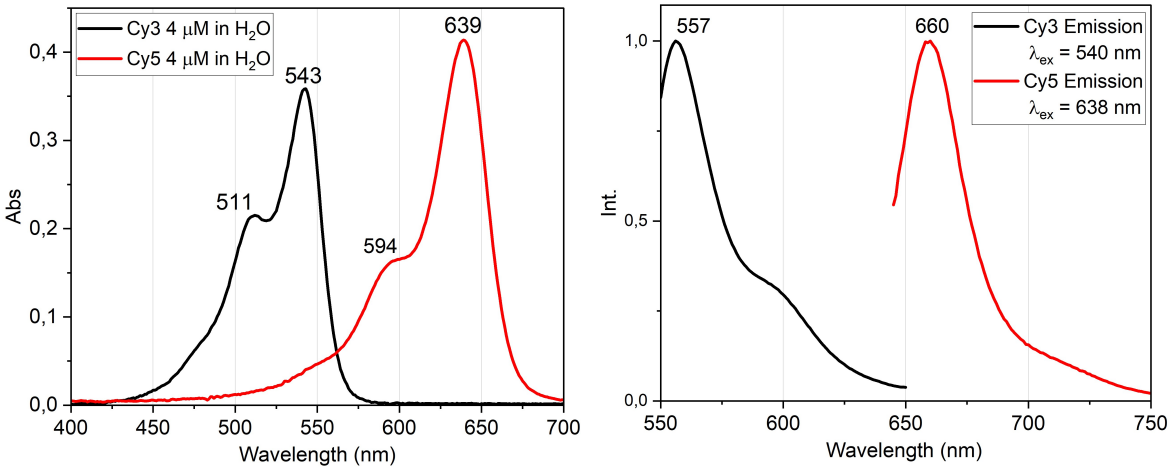

(a) Absorption spectra of Cy3 and Cy5 in water. (b) Emission spectra of Cy3 and Cy5 in water.

Figure 6.2: Spectral features of Cy3 and Cy5 in water.

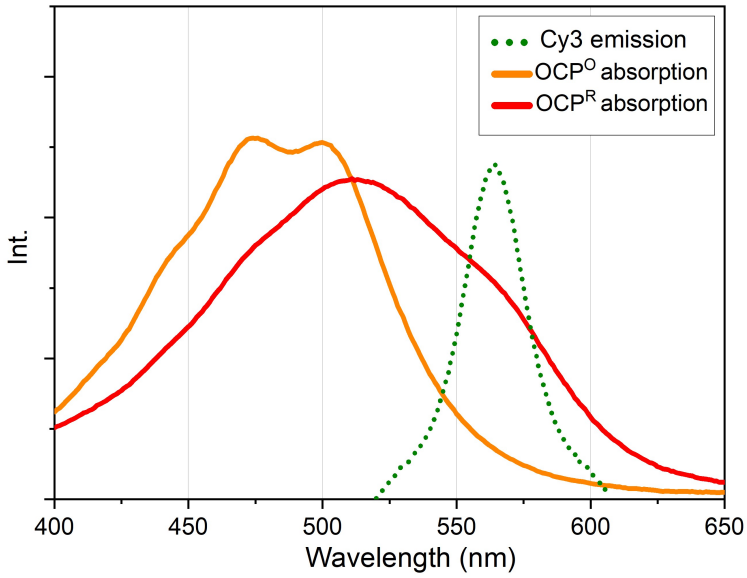

Figure 6.3: Spectral overlaps between absorption of OCP^O and OCP^R and Cy3 emission

system, OCP provides a mechanism to regulate fluorescence emission. As shown in Figure 6.3, the emission spectrum of Cy3 scarcely overlaps with the absorption spectrum of the inactive state of the protein OCP^O. Conversely, the photoactivated form OCP^R is well superimposed with Cy3 emission. This means that, while illuminating the system containing the two fluorophores and the protein (Cy3Cy5@SBA-15-NH_2+OCP^O) in its resting state at the absorption maximum of Cy3, an emission of Cy5 should be detected as energy transfer between the two fluorophores in not perturbed. On the contrary, after exposing the system to a blue led light which induces OCP photoactivation, a reduced fluorescence from Cy5 should be emitted from the system Cy3Cy5@SBA-15-NH_2+OCP^R because OCP^R blocks energy transfer. In this way, a tunable fluorescent system (Paragraph 6.1.4) can be developed.

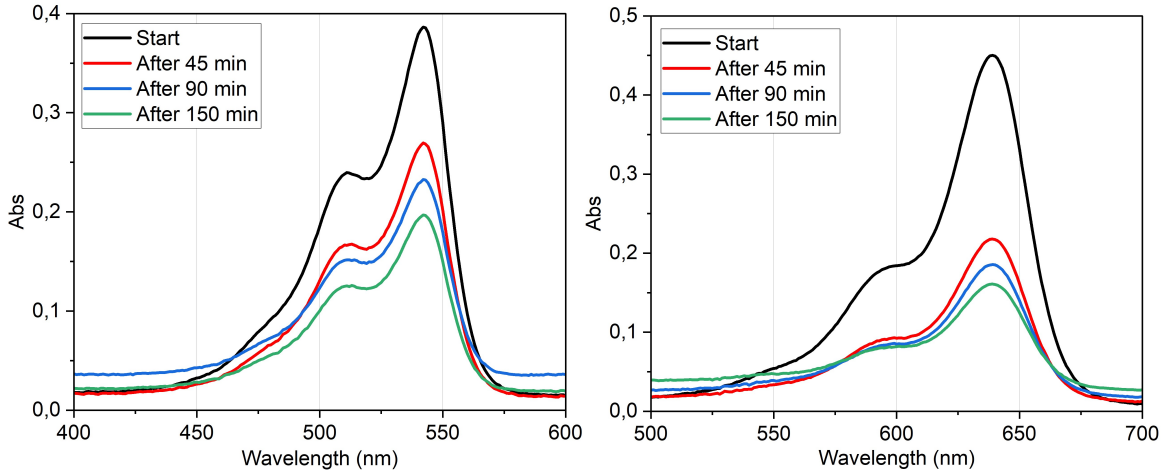

(a) UV-Vis absorption spectra of incubation liquids at different times for Cy3.

(b) UV-Vis absorption spectra of incubation liquids at different times for Cy5.

Figure 6.4: Immobilization monitoring of Cy3 and Cy5 on SBA-15-NH_2 .

6.1.1 Adsorption of Cy3 and Cy5 on SBA-15-NH_2

The adsorption kinetics of the two fluorophores on silica nanoparticles was assessed in order to determine the loading capacity. Logically speaking, an effective adsorption process should be witnessed because of the chemical affinity between the basic NH_2 functionalizing groups of the solid support and the carboxilic moiety of the fluorophores.

Experiments were carried out using 4 μM stock solutions of Cy3 and Cy5 (Lumiprobe) in Milli-Q water (pH 7 for Cy3 and pH 6.5 for Cy5). Immobilization of cyanines on SBA-15-NH_2 was performed adding 1 mL of cyanine stock solution to 10 mg of SBA-15-NH_2 powder in a 1.5 mL Eppendorf test tube. The sample was gently stirred for a certain amount of time (45 minutes, 90 minutes and 150 minutes) on a moving plate. After centrifuging the system for 5 minutes at 10000 rpm, the incubation liquids were analyzed by UV-Vis absorption spectroscopy to calculate the amount of fluorophores adsorbed on the solid powder.

Liquid phase UV-Vis spectroscopy was executed using a Biochrom Libra S60 spectrophotometer with a resolution of 0.5 nm and an acquisition time of 0.1 s per point. A 1 cm path quartz cuvette was used.

Figure 6.4 shows the absorption spectra of the starting solution at different times of incubation. The decrease of the absorbance values demonstrates that an efficient fluorophore uptake from the liquid bulk to the nanoparticle takes place. It is important to notice that some absorption

Table 6.1

	After 45 min	After 90 min	After 150 min
Cy3 immobilization	30%	40%	49%
Cy5 immobilization	51%	59%	69%

spectra of the incubation solutions present higher absorbance intensities at short wavelengths (for example at 400 nm Cy3 incubation liquid at 90 minutes shows higher absorbance than at 45 minutes). This can be justified considering that some nanoparticles may have remained in suspension even after the centrifugation, thus inducing light scattering.
The absorbance values were used to calculate the immobilization ratios, which are summarized in Table 6.1. It can be seen that Cy5 adsorbs more rapidly and in larger amounts compared to Cy3. Probably, the more extended structure of Cy5 results in a better interaction with the silica surfaces, thus enhancing the fluorophore uptake. Complete saturation of the nanoparticles with fluorophores was not reached; even after 150 minutes of incubation the molecules are still adsorbing. However, the loading kinetic analysis was stopped. The fluorophores uptake at around 60 minutes of incubation can be considered sufficient for the next part of the experiments.

6.1.2 Spectroscopic analysis on Cy3@SBA-15-NH_2 and Cy5@SBA-15-NH_2

Solid state UV-Vis spectroscopy and solid state fluorescence spectroscopy were applied on the systems Cy3@SBA-15-NH_2 and Cy5@SBA-15-NH_2 in order to see if the spectral properties of the molecules could change after immobilization. The analyzed nanoparticles were prepared following the protocol described in the previous paragraph.
Solid state UV-Vis spectroscopy was performed using a Varian 2300 UV-Vis spectrophotometer (see Paragraph 5.5.3 for details).
Fluorescence measurements were done using a HORIBA Scientific Fluorolog 3 apparatus equipped with a Xenon lamp at 450 W and two dual array monochromators (Grating 1200 gr/mm) to select the incident wavelength and the emission wavelength. Detection was performed by a PM R928 photomultiplier.

As it can be seen by looking at the analysis (Figure 6.5), some differences are noticeable com-

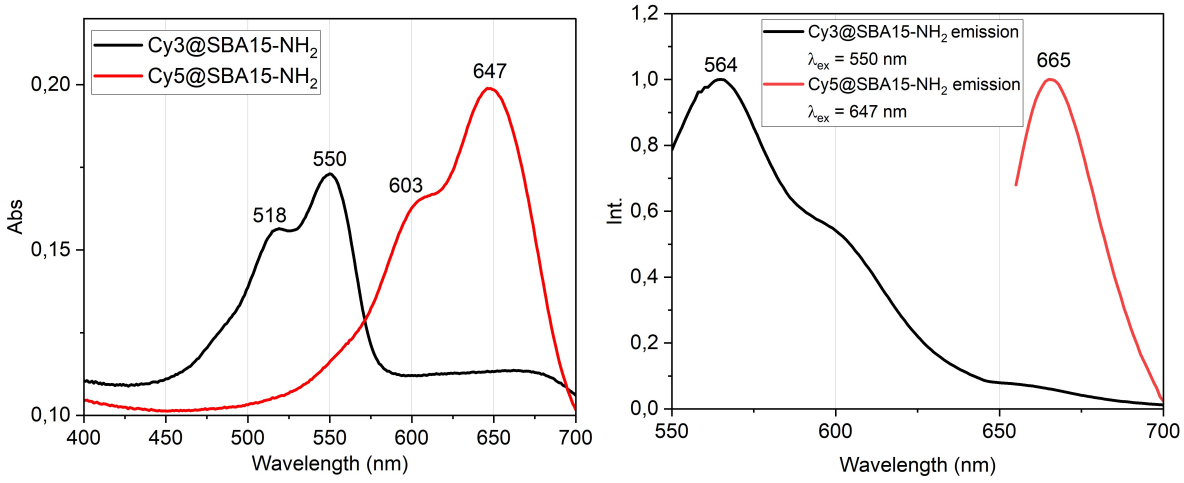

(a) Solid state UV-Vis absorption spectra. (b) Solid state fluorescence spectra.

Figure 6.5: Solid state UV-Vis and fluorescence spectra of Cy3@SBA-15-NH_2 and Cy5@SBA-15-NH_2
.

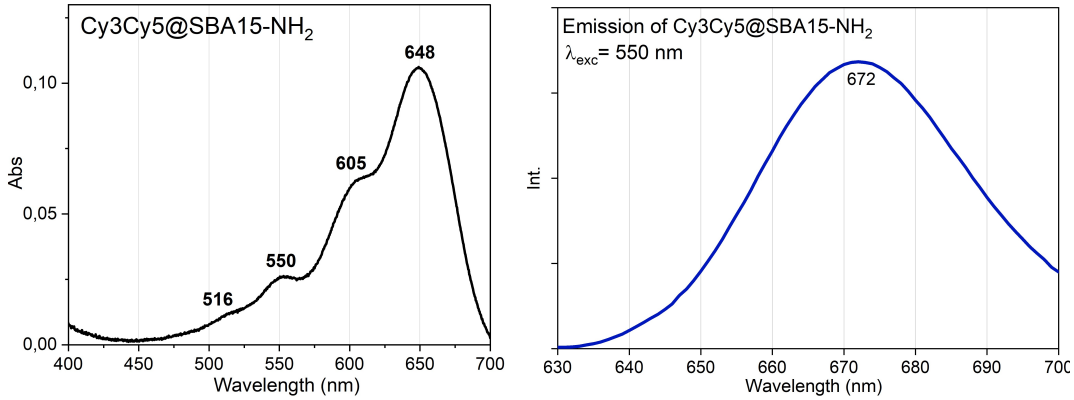

(a) Solid state UV-Vis absorption spectra. (b) Solid state fluorescence spectrum.

Figure 6.6: Solid state UV-Vis and fluorescence spectra of Cy3Cy5@SBA-15-NH_2 1:9 ratio

paring the spectroscopic responses of the fluorophores in water and in SBA-15-NH_2. For Cy3, a 7 nm red-shift for both absorption spectra and fluorescence spectra is displayed while changing the environment from the solution to SBA-15-NH_2. For Cy5, a 8-9 nm red-shift for the absorption spectra is shown, while for the emission spectrum a 5 nm red-shift is present. These modifications can be interpreted considering the interactions between the molecules and the SBA-15-NH_2 surfaces. Possibly, a distortion of the conformational structure of Cy3 and Cy5, which occurs in order to adapt to the surface, can result in these effects. Other specific chemical interactions between the functionalizing groups of the material and the organic dyes are much probably occurring, influencing the band position.

To prove that energy transfer between Cy3 and Cy5 occurs on the solid system, a new sample was prepared adsorbing Cy3 and Cy5 together on SBA-15-NH_2. The incubation mixture was prepared adding 0.1 mL of Cy3 stock solution to 0.9 mL of Cy5 stock solution. This 1:9 Cy3:Cy5 ratio was selected to enhance the detectable emission from Cy5. The overall 1.0 mL mixed solution was put in contact with 10 mg of silica powder for 60 minutes. After centrifugation, the nanoparticles were collected and analyzed with UV-Vis and fluorescence spectroscopy (Figure 6.6). The absorption spectrum clearly shows the typical bands of the fluorophores, thus concluding that Cy3 and Cy5 can be immobilized simultaneously on SBA-15-NH_2 nanoparticles. By recording an emission spectrum while exciting the sample at 550 nm, which is the absorption maximum of Cy3, an intense fluorescence at 672 nm from Cy5 is detected. This evidence confirms the photophysical mechanism of energy transfer, which can be explained considering two processes: an auto-absorption of the emitted Cy3 light from Cy5 or an actual FRET mechanism. Without further investigations, it is not possible to define which one is the main photophysical process that is taking place.

6.1.3 Cy3, Cy5 and OCP on SBA-15-NH_2

As a next step, immobilization of Cy3 and Cy5 and OCP protein on SBA-15-NH_2 nanoparticles was attempted in order to create a tunable fluorescent system. If adsorption of the two fluorophores and of OCP can be accomplished simultaneously, the two organic dyes will provide for an energy transfer based fluorescence emission system, while OCP photoactivation will provide a mechanism of regulation of the emitted light.

The adsorption of dyes and OCP on silica support was monitored by UV-Vis spectroscopy analysis of the incubation solutions. First, a water solution containing Cy3 and Cy5 was prepared adding 0.1 mL of stock solution of Cy3 into 0.9 mL of stock solution of Cy5 (1:9 ratio). The absorption spectrum of this initial solution was registered (Figure 6.7a). After that, 10 mg of SBA-15-NH_2 were introduced inside a 1.5 mL Eppendorf test tube and the Cy3:Cy5 solution was added. After incubation for 1 hour under mild stirring, the sample was centrifuged at 8000 rpm for 20 minutes and the supernatant liquid again analyzed by UV-Vis absorption. The spectra clearly show a decrease of absorption intensity concerning both absorption bands of Cy3 and Cy5, thus confirming fluorophore immobilization, as already assessed in the last paragraph. Subsequently, 1 mL of OCP solution 0.2 mg/mL (absorption spectrum in Figure

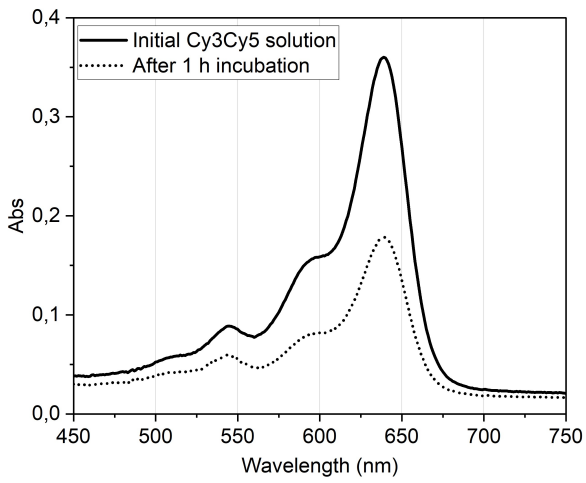

(a) Cy3 and Cy5 uptake on SBA-15-NH_2.

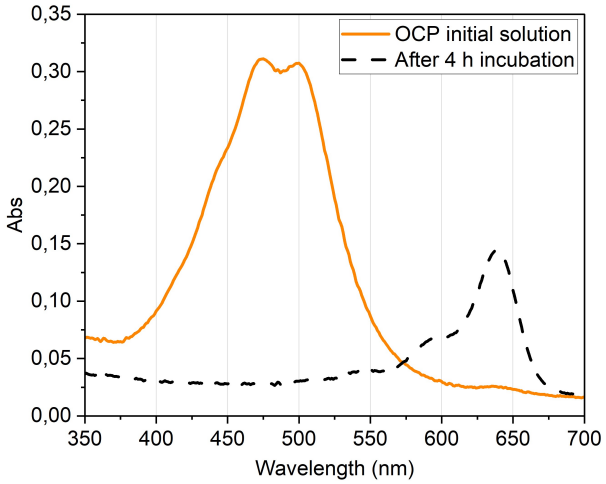

(b) OCP uptake on Cy3Cy5@SBA-15-NH_2.

Figure 6.7: UV-Vis spectra of the immobilization process of Cy3, Cy5 and OCP at the same time on SBA-15-NH_2.

6.7b) was added into the Eppendorf test tube containing the Cy3Cy5@SBA-15-NH_2 system just prepared. The suspension was kept under mild stirring for 4 hours of incubation to let OCP immobilization. Lastly, the sample was centrifuged for 20 minutes at 8000 rpm and the incubation liquids analyzed by UV-Vis spectroscopy.

As it can be seen from the spectra, after OCP incubation all the absorption bands related to OCP are reduced. This means that adsorption of OCP on the silica support had occurred efficiently. However, an absorption band at around 647 nm appears together with a very small band at around 550 nm. These peaks can be assigned to Cy3 and Cy5 absorption, meaning

that a certain amount of the two dyes was desorbed from the silica surfaces and released in the incubating solution. Apparently, OCP protein has a better affinity for SBA-15-NH_2 than Cy3 and Cy5, which dissociate from the material while OCP adsorbs. The consistent dimensional differences between OCP and organic dyes cause the protein to substitute the fluorophores on the silica surfaces. Nevertheless, little quantities of Cy3 and Cy5 are still present inside SBA-15-NH_2 as the last spectrum after OCP incubation does not have the same peak intensities of the spectrum recorded after Cy3 and Cy5 immobilization. Considering also that fluorophores have large absorption and emission yields, the system was further analyzed to define its fluorescence regulation properties.

6.1.4 Regulation of fluorescence by OCP photoactivation

Fluorescence experiments after exposing the Cy3Cy5@SBA-15-NH_2+OCP sample to blue LED light were performed, aiming to assess if the OCP^O- to-OCP^R conversion can induce quenching of Cy5 fluorescence. The sample, prepared as described above, was placed in a sample-holder inside the analysis chamber, and kept in the dark for 1 hour before performing the measurements. An initial emission spectrum was registered, exciting the system at 550 nm (Cy3 max absorption) and collecting the emission from Cy5. After that, the system was exposed to blue light from a LED source for 5, 10, 20 and 30 minutes. After each exposure a new emission spectrum was collected. As shown in Figure 6.8, an intense peak at around 665 nm appears, corresponding to Cy5 emission. Exposure to blue light, triggering photo-activation of OCP, induces partial quenching of Cy5 fluorescence as observed by the decrease in intensity of the emission peak at 665 nm. OCP^R reduces energy transfer between the two dyes, resulting in an emission decrease from Cy5. After 30 min of LED illumination, a plateau is reached, with a 37% loss of fluorescence emission. To see if a back recovery of fluorescence can occur, the sample was kept in the dark for different periods of time and emission spectra were collected after 30 minutes, 1 hour, 2 hours and 12 hours (overnight). The fluorescence intensity was almost completely restored after 2 hours in the dark and completely restored after 12 hours. Leaving the sample in the dark the back conversion of OCP^R to OCP^O restores energy transfer between the fluorophores. A second cycle of OCP photo-activation and fluorescence quenching was tested on the same sample. The same fluorescence reduction was detected and an almost complete emission restoration is observed after leaving the sample in dark for 12 hours.
To understand if the emission diminution is actually caused by the hypothesized photophysical mechanism, a control experiment was carried out on a sample containing only the two fluorophores on SBA-15-NH_2. The same blue LED exposure cycle was applied on the system to make sure that the emission reduction is not caused by a photodegradation of the fluorophores. The analysis (Figure 6.9) confirms that fluorescence emission from Cy5 is basically unperturbed after 30 minutes of light exposure, thus concluding that Cy3 and Cy5 are not photodegradated. Overall, SBA-15-NH_2 tunable fluorescent nanoparticles based on Cy3 and Cy5 fluorophores (providing emission yield) and OCP protein (providing a regulation mechanism) were success-

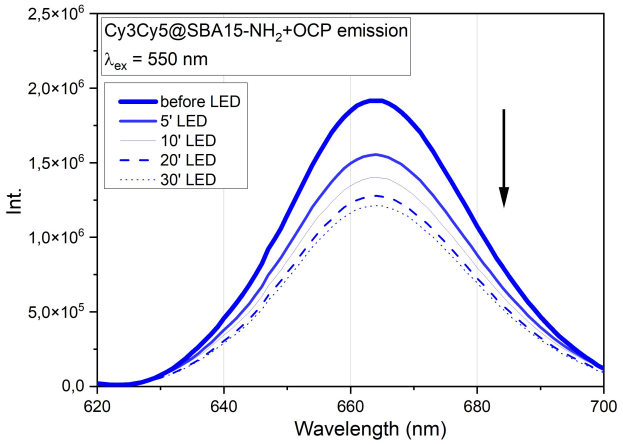

(a) First activation cycle: fluorescence decrease.

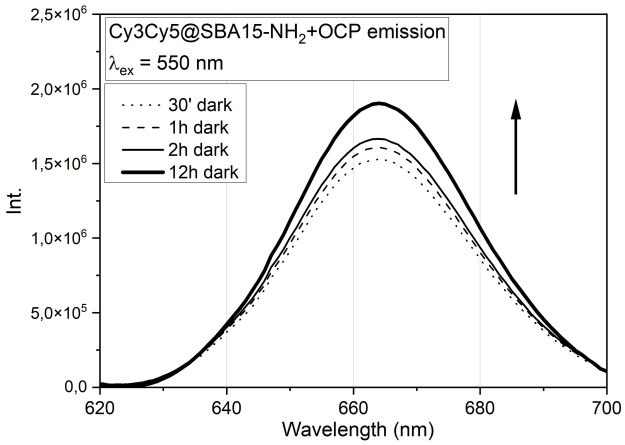

(b) First activation cycle: full fluorescence recovery.

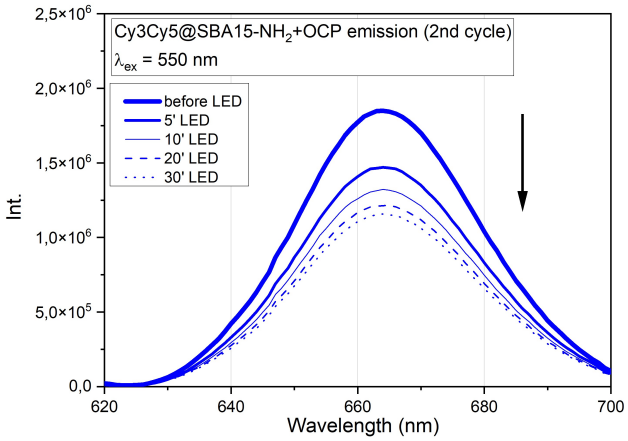

(c) Second activation cycle: fluorescence decrease.

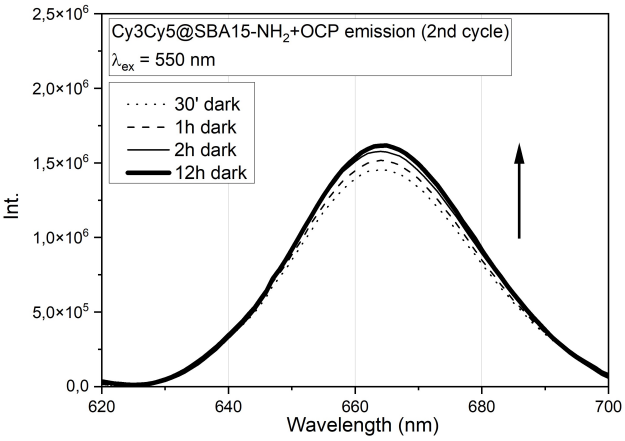

(d) Second activation cycle: partial fluorescence recovery.

Figure 6.8: Solid state emission spectra of Cy3Cy5@SBA-15-NH_2+OCP for first and second activation cycles.

fully developed. It is important to notice that our system mimics the natural photoprotective roles of OCP. In cyanobacteria, activated OCP preforms photoprotection by blocking energy transfer between phycobilisomes and reaction centers. In our developed system the same process occurs, as OCP blocks energy transfer between the two dyes.

6.1.5 pH-dependent fluorescence regulation

Considering previous experiments showing how OCP responds to pH changes [53, 73], it was observed that when the protein encounters a very acidic environment (pH $\leq$ 1) an activation of OCP occurs, even in dark, leading to an accumulation of the OCP^R state. This process could be applied also on our fluorescent system, where the fluorescence regulation of Cy5 can be achieved by OCP activation induced by a chemical stimulus, i.e. the pH change. To do so, Cy3Cy5@SBA-15-NH_2+OCP was analyzed using emission spectroscopy. After recording a first fluorescence spectrum, 1 drop of concentrated HCl was added to the system and the subsequent fluorescence spectra were recorded. The system shows an 80% loss of the initial

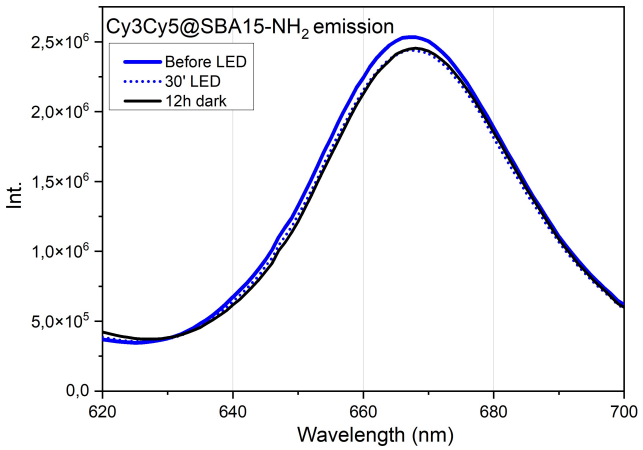

Figure 6.9: Emission spectroscopy control experiment on Cy3Cy5@SBA-15-NH_2 exposed to blue LED light.

intensity emission after 30 minutes (Figure 6.10). However, the intensity drop is not fully caused by the blocked energy transfer from Cy3 to Cy5. A degradation of fluorophores is also encountered, as a control experiment performed on a sample of Cy3Cy5-loaded SBA-15-NH_2 shows that after addition of HCl the intensity of Cy5 emission decreases of about 10%.
This experiment can be considered as a proof of principle for future studies on the applications of the system as a pH sensor.

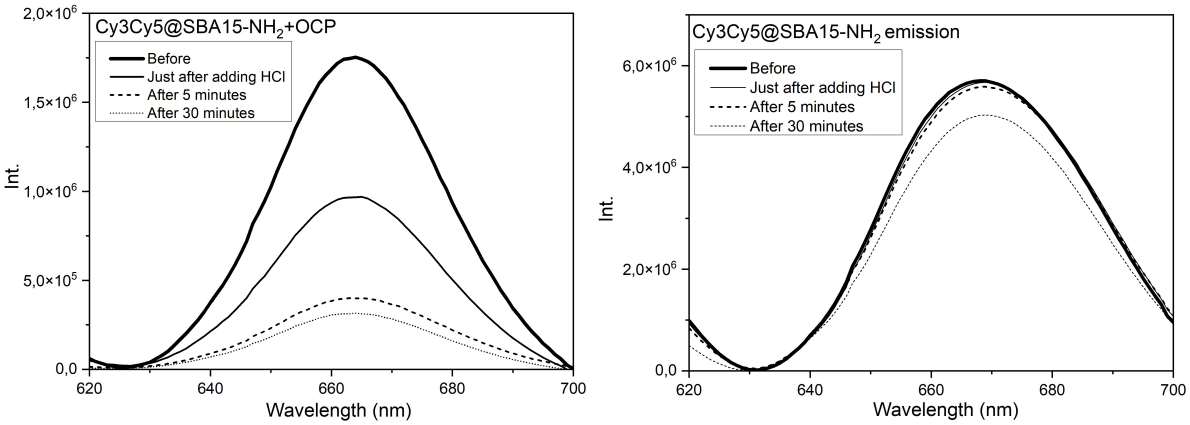

(a) Fluorescence emission after HCl addition. (b) Control experiment without OCP.

Figure 6.10: Fluorescence quenching of Cy3Cy5@SBA-15-NH_2+OCP system by changing the pH of the environment.

6.2 3HF system

Another additional category of molecules was adsorbed on our solid material for the development of fluorescent nanoparticles. This new group of molecules consists in flavonoids. Flavonoids are natural widely abundant polyphenolic compounds occurring in a large variety of structures [81, 82]. In plants, among all the different roles in which they are involved, they act in particular as natural antioxidants and perform photoprotective activity. The recurrent

chemical structure of flavonoids consists of two aromatic rings connected by a pyrane core, forming together a conserved fifteen carbon atoms moiety. Immobilization of flavonoids on silica nanoparticles gained attention over the past years. Functionalized silica NPs were used as carriers for antioxidant flavonoid delivery, increasing the stability, epidermal penetration and topical efficiency of the antioxidant [83].

The present work has the objective of developing a photo-regulated fluorescent nanoparticle system, using the same photophysical concepts of the fluorescent nanoparticles doped with Cy3 and Cy5 dyes and OCP protein. This new system containing flavonoids and OCP adsorbed on silica SBA-15-NH_2 will present intriguing properties not only because it will be biocompatible, but also because it will be characterized by antioxidant properties, as both the fluorophore (flavonoid) and the photo-modulation element (OCP) are strong antioxidants. For our system, a flavonoid belonging to the flavonol sub-group, 3-hydroxyflavone (3HF), was chosen.

6.2.1 3HF photophysics

3-hydroxyflavone (3HF) presents a complex photophysics studied by multiple research works (see references [84, 85] and refs. therein). In short, the UV light absorption promotes the 3HF molecule from its ground state N to its excited singlet N^* state. The excited singlet N^* state undergoes a process called excited state intramolecular proton transfer (ESIPT) where the proton from the 3-OH group is transfered to the C=O moiety. This mechanism results in the formation of an excited tautomeric form T^* which eventually relaxes emitting light in the Vis range of 500-540 nm. However, the molecule can also relax from its original exited state N^*, giving an emission peak at around 400 nm. For these reasons, the emission spectrum of 3HF is typically composed of two bands originating from N^* and T^* relaxations. The ratio between N^* and T^* fluorescence emission strongly depends on the environment in which 3HF is sur-

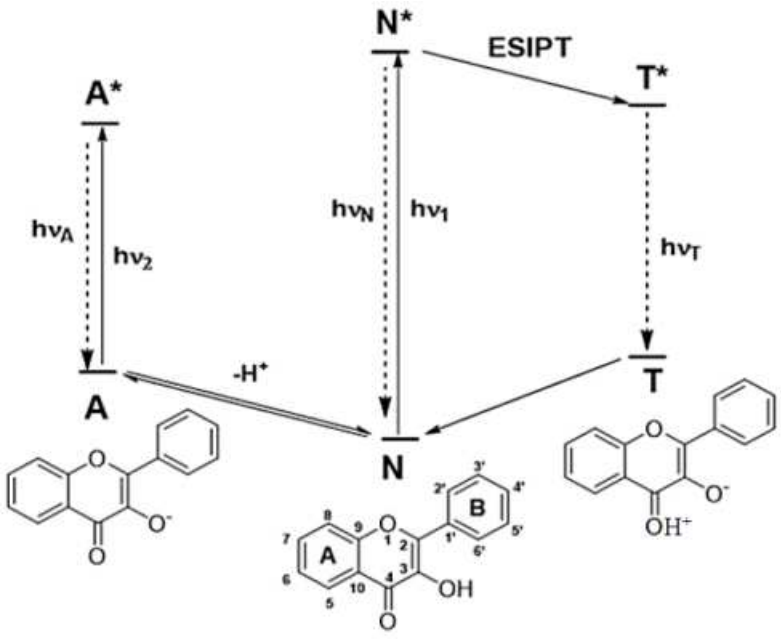

Figure 6.11: Photophysics of absorption and emission involving the different states of 3HF.

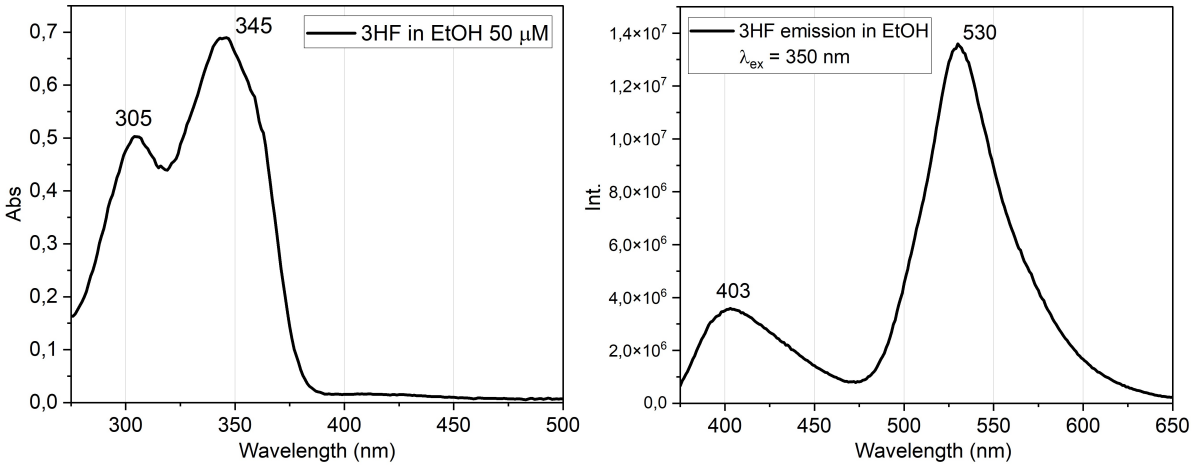

(a) Absorption spectrum (b) Emission spectrum

Figure 6.12: Absorption and emission spectra of 3HF in ethanol.

rounded. For example, polar and protic solvents tend to inhibit the ESIPT mechanism and thus the T^* emission. Conversely, in very apolar solvents, ESIPT and its T^* emission are the only occurring processes. Furthermore, 3HF in its ground state has the ability to establish a deprotonation equilibrium (always envolving the 3-OH group) which results in the generation of an anionic species A. The anionic form absorbs light at higher wavelengths and emits fluorescence at around 460-490 nm. Similarly to the other processes, the formation and the spectral characteristics of the anionic species depend on the chemical environment.

As an example, absorption and emission spectra of 3HF in ethanol are reported in Figure 6.12. The emission spectrum presents a band at 403 nm which is assigned to the radiative relaxation of N^* state, while the band at 530 is generated from the tautomeric T^* state emission given by ESIPT process. A third band related to the A^* state emission is not observable, due to the low amount of anion formed in ethanol (which is responsible of the very weak band at around 420 nm in the absorption spectrum).

The development of 3HF-based tunable fluorescent nanoparticles loaded with OCP takes advantage of the different spectral overlaps between the emission spectrum of 3HF and the absorption spectrum of OCP^O and OCP^R. Indeed, due to the ESIPT process, the emission spectrum of 3HF is largely shifted at higher wavelengths compared to its absorption spectrum. OCP^O and OCP^R absorption spectra are thus located in the middle between absorption and emission of 3HF (see Figure 6.13). OCP^R is largely overlapped with the emission of 3HF, so that photoactivation of the protein after a blue LED light exposure should reduce 3HF emission (the processes of FRET energy transfer and/or normal absorption of 3HF emitted light from OCP^R can take place). In this way, similarly to the system containing Cy3 and Cy5 described above, fluorescence emission of 3HF-doped SBA-15-NH_2 nanoparticles can be regulated by OCP photoactivation.

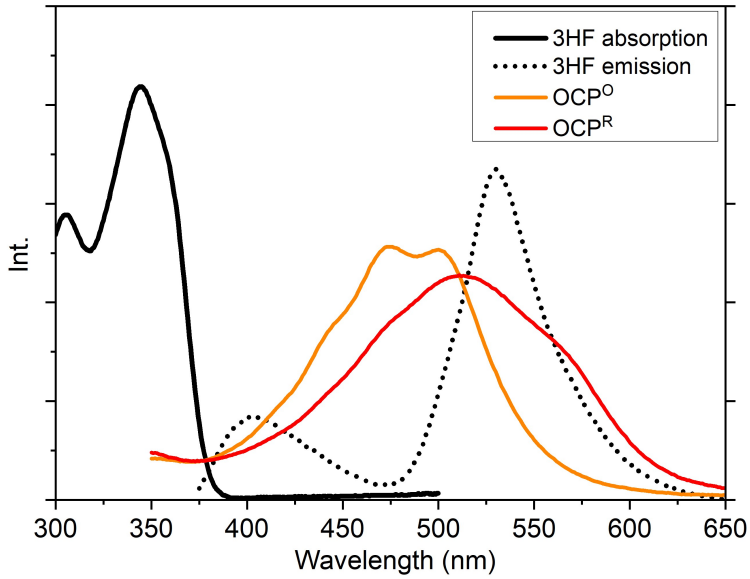

Figure 6.13: Spectral overlaps between 3HF absorption and emission and OCP^O and OCP^R absorptions.

6.2.2 3HF adsorption on SBA-15-NH_2

A protocol to adsorb 3HF on SBA-15-NH_2 was followed. Briefly, 10 mg of silica nanoparticles were put in contact with 1 mL solution of 3HF 10^{-3} M for 1 hour inside a 1.5 mL Eppendorf test tube under gentle stirring. After, the solvent was removed by evaporation. Subsequently, a water treatment on the dry 3HF-loaded nanoparticles was performed adding 1 mL of water at different pH values (pH 7.5 and pH 5). The sample was then centrifuged at 8000 rpm for 20 minutes and the solid collected for solid state fluorescence emission analysis (Figure 6.14).
After water treatment at pH 7.5 (the pH value of the protein buffer) the emission spectrum shows two intense bands at 485 nm and at 533 nm that can be assigned respectively to the emission from the anionic species (A^*) and from the tautomeric species (T^*). In fact, the NH_2 groups of the silica matrix act as a base and partially deprotonate the flavonol, thus enhancing the fluorescence emission from the anion. A very small band at around 400 nm can be associated to the emission from the normal photoexcited state N^*. Conversely, the sample treated at pH 5 presents a smaller band at 487 nm, always assignable to the anionic form of 3HF, because the slight acidic environment affects the protonation equilibrium, inducing an accumulation towards the protonated species. The 523 nm band is related to the emission of the tautomer, while the small peak at around 410 nm is related to the N state.
The effect of blue LED light exposure was analyzed for both 3HF@SBA-15-NH_2 samples. The sample treated at pH 7.5 is very photo-degradable, as it can be seen by the decrease of fluorescence intensity during illumination, while the sample treated at pH 5 seems more resistant to light exposure. This can be explained considering that the anionic species, which is more abundant in the sample at pH 7.5, is less photostable compared to the other forms of 3HF. For the sample treated at pH 5, only a slight decrease of emission intensity is observed. These evidence led us to use the sample at pH 5 for the development of tunable nanoparticles based on 3HF and

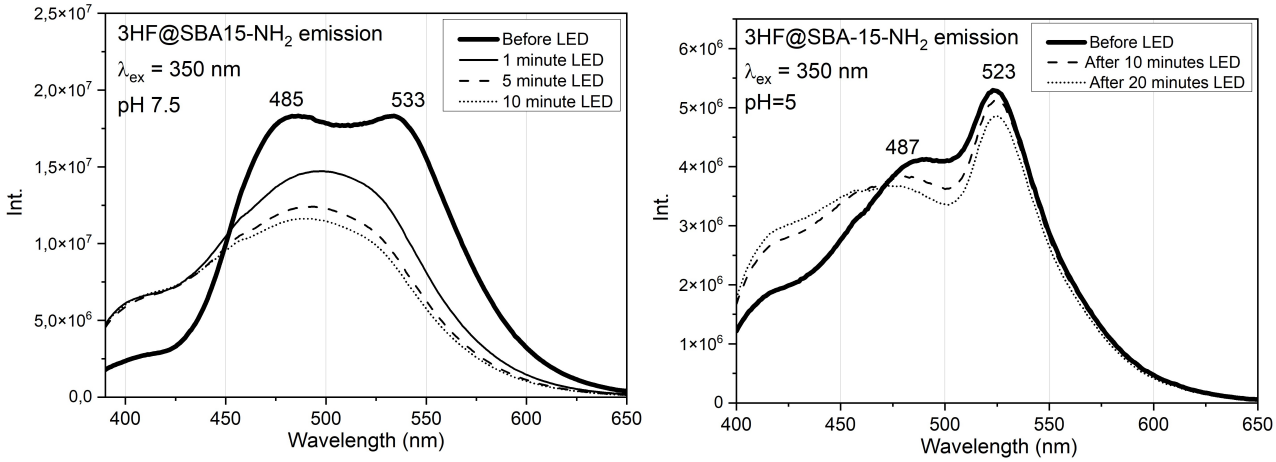

(a) Emission spectrum at pH 7.5 (b) Emission spectrum at pH 5

Figure 6.14: Emission spectra of 3HF@SBA-15-NH_2 treated at pH 7.5 or pH 5. Effect of blue LED light exposure.

OCP protein adsorbed on SBA-15-NH_2 nanoparticles.

6.2.3 OCP loaded 3HF@SBA-15-NH_2 tunable fluorescent system

To create a tunable fluorescent system, OCP was adsorbed together with 3HF on the silica scaffold. To do so, 3HF@SBA-15-NH_2 nanoparticles treated at pH 5, as prepared and described in the previous paragraph, were put in contact with 1 mL solution of OCP 0.2 mg/mL for 4 hours under gentle stirring inside a 1.5 mL Eppendorf test tube. After incubation, the sample was centrifuged at 8000 rpm for 20 minutes to collect the solid phase for emission spectroscopy analysis (Figure 6.15).

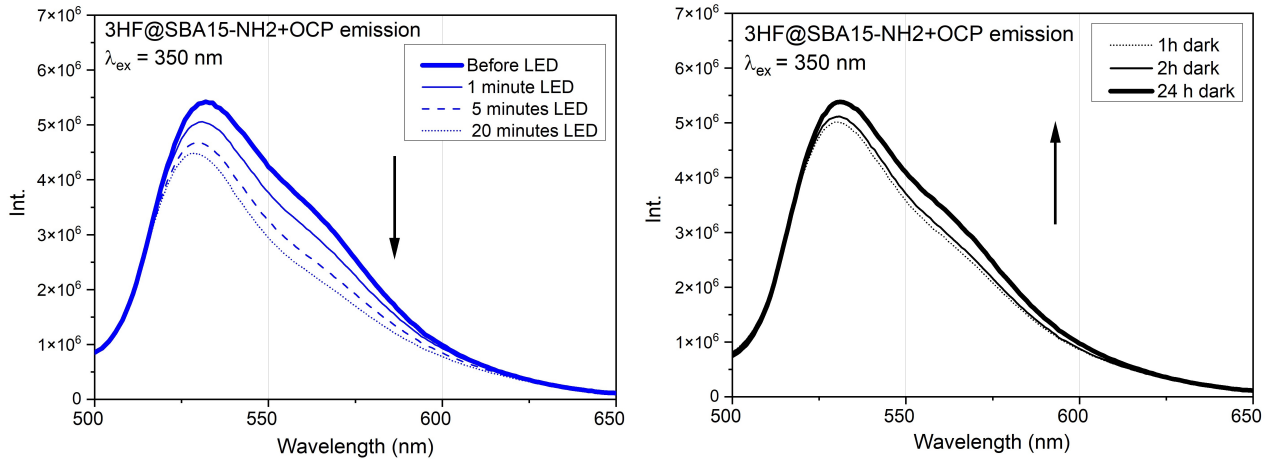

(a) Fluorescence decrease. (b) Fluorescence back recovery.

Figure 6.15: Emission spectra of 3HF@SBA-15-NH_2+OCP at different blue LED light exposure times and fluorescence back recovery in dark.

A first emission spectrum was recorded before switching on the blue LED light, showing an emission band at around 530 nm from the tautomeric state. Subsequently, LED light exposure

was applied for 1, 5 and 20 minutes, registering an emission spectrum at each stage. As it can be seen on the image, a decrease in intensity is shown, which can be explained considering OCP photoactivation and consequent spectral overlap between 3HF emission and OCP^R absorption. The fluorescence intensity reduction after 20 minutes of LED exposure is about 20%. After leaving the sample in the dark for some time, an almost complete back recovery of fluorescence is shown. OCP back conversion in its dark-adapted state restores 3HF emission.

Overall, the development of fluorescent tunable nanoparticles was successfully achieved. Different fluorophores like Cyanine 3, Cyanine 5 and 3-hydroxyflavone were efficiently adsorbed on silica SBA-15-NH_2 nanoparticles in order to create a fluorescent system. By a concomitant adsorption of fluorophores and OCP protein, the synthesized system results in a fluorescent device photo-modulated by blue light.

7

EPR Spectroscopy on OCP

Electron Paramagnetic Resonance spectroscopy reveals selectively paramagnetic states, which means systems with unpaired electrons [86, 87]. The detection of paramagnetic states by EPR spectroscopy permits to assess the characteristics of their electronic structures and thus their chemical properties. EPR spectroscopy has been applied in multiple fields, including the investigation of photosynthetic systems. Regarding this aspect, the determination of specific chemical features associated to photosynthesis processes, embracing also the mechanisms of photoprotection, has been largely accomplished by EPR analysis [88, 89].

Regarding OCP, studies by EPR spectroscopy have never been applied before. Besides some EPR spin trapping analysis on OCP's ability to quench singlet oxygen, characterizations of possible paramagnetic states involving the internal OCP carotenoid molecule have never been reported up to date. However, radicals [90], triplet states and charge-separation states [91] are known to be formed in carotenoids and therefore can in principle be found or trapped even in OCP. Also, some of these states could be further stabilized in the SBA-15-NH_2 matrix.

Our analysis began with Time Resolved Electron Paramagnetic Resonance (TR-EPR) measurements under photoexcitation on OCP in solution and adsorbed on SBA-15-NH_2 nanoparticles. By photoexciting the system at the absorption wavelength of the OCP carotenoid we tried to isolate possible paramagnetic species that could be formed during the photoactivation mechanism of the protein, thus revealing additional intermediate states that might play a key role in the overall process.

Our second approach was to force the formation of paramagnetic species through triplet-triplet energy transfer (TTET) mechanism between OCP's carotenoid and an external chlorophyll *a* molecule acting as photosensitizer. This strategy was inspired by the natural photoprotective processes found in plant and algae. In the condition of high irradiance, the absorption of excess light by chlorophylls in photosynthetic organisms induces an accumulation of triplet states (^{3}Chls) by the action of Intersystem Crossing (ISC) mechanism. ^{3}Chls can act as photosensitizer for production of singlet oxygen $^1O_2$, a dangerous oxidizing species that performs photodamage. In order to suppress the generation of singlet oxygen, the triplet state of chlorophylls is quenched to the singlet state by the interaction with carotenoid molecules. If a carotenoid is located in proximity of a ^{3}Chl molecule, there is a certain probability that a TTET mechanism

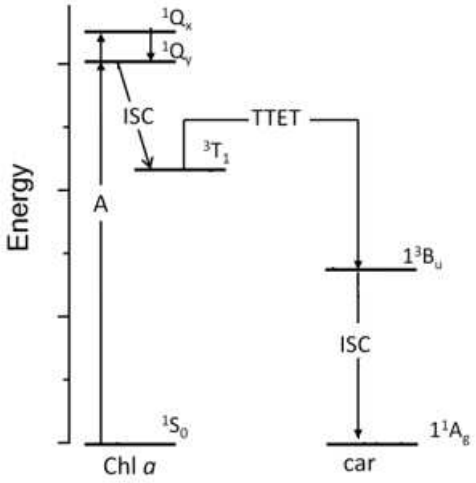

Figure 7.1: Simplified scheme for the energy levels of chlorophylls and carotenoids.

takes place. The triplet state of chlorophyll is transferred to the carotenoid molecule, which then can dissipate the acquired energy by a further ISC mechanism (Figure 7.1), thus accomplishing photoprotection.

By means of TTET with an interacting photoexcited ^{3}Chl molecule, the carotenoid can be isolated for a certain period of time in its triplet state and characterized by TR-EPR spectroscopy. In order to have an efficient TTET process, the molecules need to be at short distances. As seen in the previous chapters, mesoporous nanoparticles can be used to bring molecules in close contact allowing to envisage possible uses for different scopes based on energy transfers. We tried to exploit this potentiality to mimic the TTET occurring between chlorophylls and carotenoids in photosynthetic systems. We analysed a system containing OCP and chlorophyll *a* (Chla) adsorbed on SBA-15-NH_2 nanoparticles by TR-EPR at different excitation wavelengths. The study of the effects of the protein chemical environment and of the SBA-15-NH_2 matrix on the electronic characteristics of the delocalized carotenoid triplet is considered as the principal scope of our analysis.

In the following paragraphs, a brief description of paramagnetic states, in particular triplet states and their interaction with an external magnetic field is presented, as well as the ISC and TTET mechanisms. A summarized explanation of a typical TR-EPR experiment is reported in Section 7.2, while the analysis of the prepared samples of OCP and chlorophyll is described in Section 7.3.

7.1 Systems with two electrons

A spin system of two electrons can assume four different spin states [41]:

$$\alpha(1)\alpha(2) \quad \alpha(1)\beta(2) \quad \beta(1)\alpha(2) \quad \beta(1)\beta(2) \tag{7.1}$$

where $\alpha()$ and $\beta()$ are the spin eigenfunctions of the monoelectronic spin operators $\hat{S}^2$ and $\hat{S}_z$ and the numbers 1 and 2 identify which one of the two electrons is considered. This description is also called *uncoupled representation*.

It is more convenient, for two interacting electrons, to combine these states in an antisymmetric or in a symmetric combination (*coupled representation*) with respect to the exchange of the electrons. The total spin quantum number $S = \sum s_i$ and the total magnetic quantum numbers $M_s = \sum m_{s,i}$ classify the four spin states:

$$Antisymmetric\ (S = 0): \qquad \sigma_0 = \frac{1}{\sqrt{2}}[\alpha(1)\beta(2) - \beta(1)\alpha(2)] \tag{7.2}$$

$$Symmetric\ (S = 1): \qquad \tau_{+1} = \alpha(1)\alpha(2) \tag{7.3}$$

$$\tau_0 = \frac{1}{\sqrt{2}}[\alpha(1)\beta(2) + \beta(1)\alpha(2)] \tag{7.4}$$

$$\tau_{-1} = \beta(1)\beta(2) \tag{7.5}$$

The antisymmetric and symmetric combinations are eigenfunctions of the total operators $\hat{S}^2 = (\hat{s}_1 + \hat{s}_2)^2$ and $\hat{S}_z = \hat{s}_{z,1} + \hat{s}_{z,2}$. The state characterized by a total spin quantum number $S = 0$ and, consequently, by a total magnetic quantum number $M_s = 0$ is called singlet, thus identified by the symbol σ_0. The state with $S = 1$ is splitted in three states (triplet) identified by the total magnetic quantum numbers $M_s = +1, 0, -1$, thus by the symbols τ_{+1}, τ_0 and τ_{-1}.

For two electrons occupying the same spacial orbital, only the antisymmetric combination can describe the spin sate (Pauli exclusion principle) and the system will be a singlet. However, if the electrons occupy different orbitals, then a symmetric combination of the spin states is possible, leading formation of a triplet state.
The main interactions between two electrons are the Electron-Exchange Interaction and the Electron-Electron Dipole Interaction, described in the following paragraphs.

7.1.1 Electron-Exchange Interaction

Exchange interaction takes into account the electrical coulombic interaction between the two electrons [92]. This causes a split in energy between the singlet state and the triplet states (which remain degenerate). Exchange interaction can be represented by the exchange spin hamiltonian, here simplified considering only its isotropic part:

$$\hat{H}_{exch} = J_0 \hat{\mathbf{S}}_1 \cdot \hat{\mathbf{S}}_2 \tag{7.6}$$

where $\hat{\mathbf{S}}_1$ and $\hat{\mathbf{S}}_2$ are the spin operators for electrons 1 and 2 and J_0 is the isotropic exchange coupling constant, in first approximation given by the exchange integral:

$$J_0 = -2\langle\phi_a(1)\phi_b(2)|\frac{e^2}{4\pi\epsilon_0 r}|\phi_a(2)\phi_b(1)\rangle \tag{7.7}$$

ϕ_a and ϕ_b are two different spacial wavefunctions evaluated considering the electrons to be non-interacting, ϵ_0 is the permittivity of vacuum and r is the interelectronic distance.
The sign of J_0 defines which state, the singlet or the triplet, lies at lower energy. For example, if $J_0 < 0$, the triplet state will be at lower energy compared to the singlet state (Figure 7.2).

7.1.2 Electron-Electron Dipole Interaction

In addition to exchange, the dipolar interaction must be considered in a system with more than one unpaired electron. Dipolar interaction consists in an anisotropic dipole-dipole magnetic interaction between the magnetic moments associated to the spin angular moments [92]. This interaction causes the three-fold degeneracy of the triplet states to be removed even without the application of an external magnetic field; this effect is called *zero-filed splitting* (ZFS).
The magnetic dipole-dipole interaction is described by the dipolar hamiltonian term:

$$\hat{H}_{SS} = \frac{\mu_0}{4\pi}(g\beta_e)^2\left[\frac{\hat{\mathbf{S}}_1 \cdot \hat{\mathbf{S}}_2}{r^3} - \frac{3(\hat{\mathbf{S}}_1 \cdot \mathbf{r})(\hat{\mathbf{S}}_2 \cdot \mathbf{r})}{r^5}\right] \tag{7.8}$$

where g is the electron g-factor (considered isotropic for simplicity), β_e is the Bohr magneton and μ_0 is the magnetic permittivity of vacuum.
Since the system is composed of coupled electrons, it is more convenient to express the $\hat{H}_{SS}$ hamiltonian in terms of the total spin operator $\hat{\mathbf{S}}$ and of the second rank dipolar tensor $\tilde{\mathbf{D}}$:

$$\hat{H}_{SS} = \hat{\mathbf{S}} \cdot \tilde{\mathbf{D}} \cdot \hat{\mathbf{S}} \tag{7.9}$$

where the tensor elements are

$$D_{ij} = \frac{\mu_0}{8\pi}(g\beta_e)^2\langle\frac{r^2\delta_{ij} - 3ij}{r^5}\rangle \tag{7.10}$$

where $i, j = x, y, z$ are the distance components of r in the reference frame and the bra-ket notation expresses an average over the electronic spacial wavefunction.
If a proper system of coordinates is chosen, usually reflecting the symmetrical properties of the molecule, the dipolar tensor can assume a diagonal form. The diagonal elements of the diagonalized dipolar matrix, called principal values, are expressed as X, Y and Z. By convention, Z is assigned to the principal value with the highest absolute magnitude. Y has the smallest absolute value (in the case where X ≠ Y).
In the principal axis frame, the dipolar hamiltonian takes the simpler form:

$$\hat{H}_d = X\hat{S}_x^2 + Y\hat{S}_y^2 + Z\hat{S}_z^2 \tag{7.11}$$

with

$$X = \frac{\mu_0}{8\pi}(g\beta_e)^2\langle\frac{r^2 - 3x^2}{r^5}\rangle \tag{7.12}$$

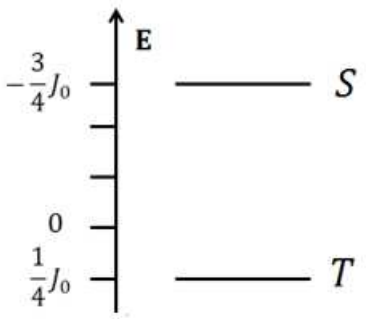

Figure 7.2: Singlet (S) and triplet (T) state energies for a bi-electronic system with $J_0 < 0$.

$$Y = \frac{\mu_0}{8\pi}(g\beta_e)^2\langle\frac{r^2 - 3y^2}{r^5}\rangle \tag{7.13}$$

$$Z = \frac{\mu_0}{8\pi}(g\beta_e)^2\langle\frac{r^2 - 3z^2}{r^5}\rangle \tag{7.14}$$

The sum of the diagonal elements of the dipolar tensor is zero (traceless tensor). This restriction implies that only two of the principal values are independent. According to this property, the principal values can be expressed in function of two parameters D and E, known as ZFS parameters:

$$D = -\frac{3}{2}Z \tag{7.15}$$

$$E = \frac{1}{2}(Y - X) \tag{7.16}$$

The D parameter reflects the extension of the electronic delocalization along the principal Z axis, while the E parameter gives information on the deviation of the electronic structure from the axial symmetry with respect to the Z principal axis.
It is important to notice that the spin eigenfunctions τ_{+1}, τ_0 and τ_{-1} defined before are no more eigenfunction for the dipolar hamiltonian $\hat{H}_d$. However, they provide a basis set for linear combinations in order to diagonalize $\hat{H}_d$. These linear combinations are:

$$\tau_x = \frac{1}{\sqrt{2}}[\tau_{-1} - \tau_{+1}] \tag{7.17}$$

$$\tau_y = \frac{i}{\sqrt{2}}[\tau_{-1} + \tau_{+1}] \tag{7.18}$$

$$\tau_z = \tau_0 \tag{7.19}$$

It is possible to demonstrate that the energies related to the τ_x, τ_y and τ_z states are respectively X, Y, and Z, which can be written according to the D and E parameters:

$$X = \frac{1}{3}D - E \tag{7.20}$$

$$Y = \frac{1}{3}D + E \tag{7.21}$$

$$Z = -\frac{2}{3}D \tag{7.22}$$

For planar molecules, like chlorophyll *a* and carotenoids, the ZFS reference frames that verify the convention |Z|>|X|>|Y| are reported in Figure 7.3.

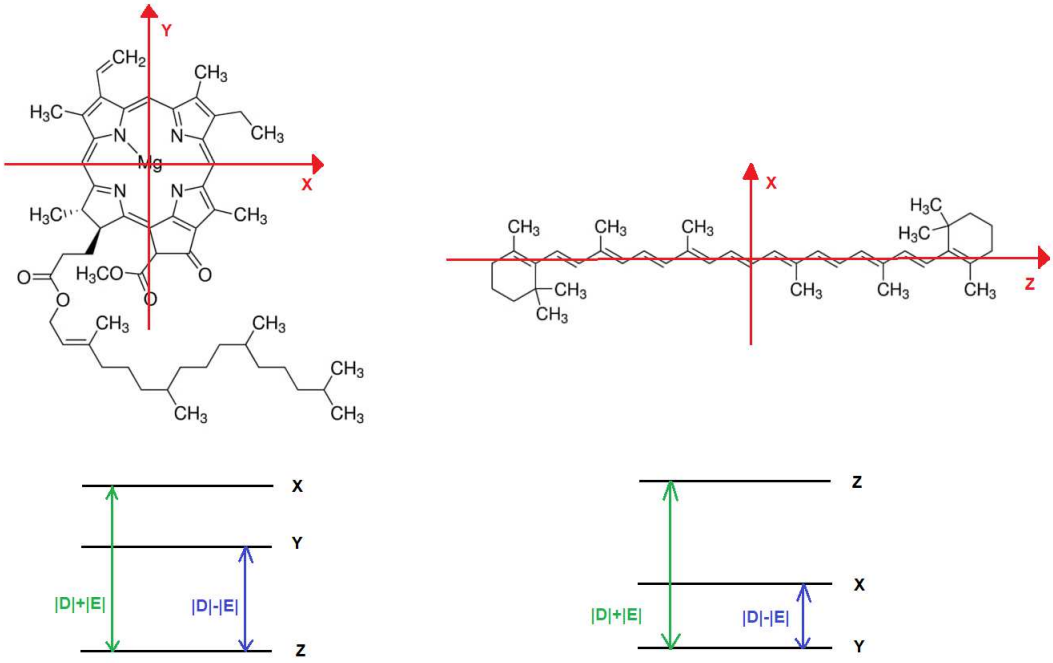

Figure 7.3: On top, Chlorophyll *a* and carotenoid ZFS reference frames. At the bottom, energy levels of the triplet states. For chlorophyll, D>0 and E<0. For carotenoid, D<0 and E<0.

7.1.3 Interaction with an external magnetic field

If an external static magnetic field is applied to the system, the interaction between the spin moments and the magnetic field $\mathbf{B}_0$, described by the Zeeman hamiltonian ($\hat{H}_Z$) must be considered [92]. The total spin hamiltonian will be:

$$\hat{H}_{Tot} = \hat{H}_d + \hat{H}_Z \tag{7.23}$$

$$= \hat{\mathbf{S}} \cdot \tilde{\mathbf{D}} \cdot \hat{\mathbf{S}} - g\beta_e \mathbf{B}_0 \cdot \hat{\mathbf{S}} \tag{7.24}$$

Neither the eigenfunctions τ_{+1}, τ_0, τ_{-1} nor the eigenfunctions τ_x, τ_y, τ_z can diagonalize the total spin hamiltonian. Thus, the functions τ_x, τ_y and τ_z are chosen as a basis set for linear combinations in order to diagonalize the total hamiltonian and create three orthonormal eigenfunctions. To solve the problem, it is simpler to study the case where $\mathbf{B}_0$ is directed parallelly to one of the ZFS axis, for instance the Z axis. In this way, the spin states and the corresponding energies are:

$$T_{+1} = \frac{\sqrt{2}}{2i}(\tau_y - \tau_x) \qquad E_{+1} = g^2\beta^2 S B_0 + \frac{1}{2}(X + Y) \tag{7.25}$$

$$T_0 = \tau_z \qquad E_0 = Z \tag{7.26}$$

$$T_{-1} = \frac{\sqrt{2}}{2i}(\tau_y + i\tau_x) \qquad E_{-1} = -g^2\beta^2 S B_0 + \frac{1}{2}(X + Y) \tag{7.27}$$

The same approach can be applied also when the magnetic field is parallel to the X or the Y axis of the ZFS reference frame, obtaining similar results. The main conclusion is that the

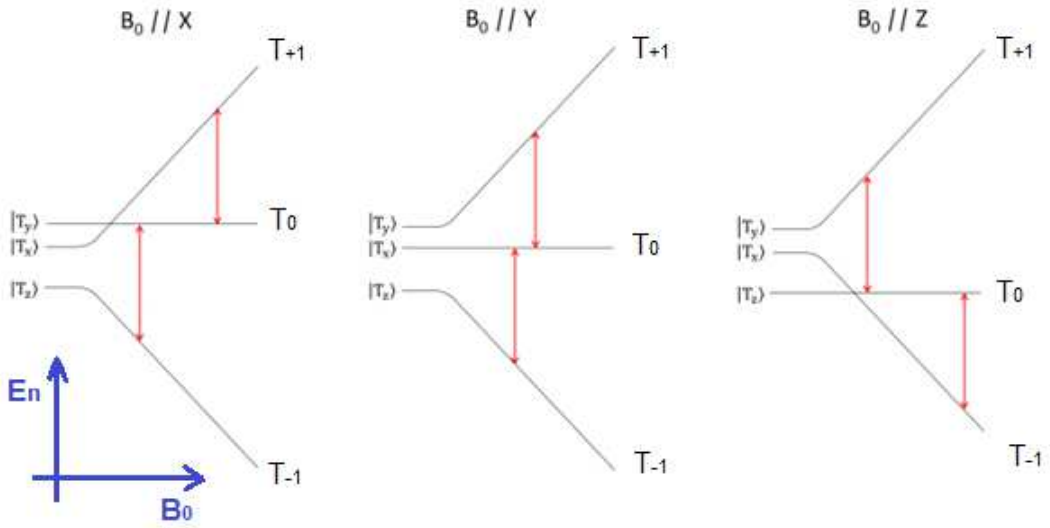

Figure 7.4: Energy levels of a triplet spin system in an external magnetic field oriented along the X or Y or Z directions of the ZFS reference frame. Scheme valid for D>0 and E<0 (e. g. chlorophyll *a*). In red, the allowed EPR transitions.

energy levels and the spin states depend on the direction of $\mathbf{B}_0$ with respect to the molecular orientation. In Figure 7.4, an example of the triplet energy levels and their behaviour according to the magnetic filed intensity is reported.

7.1.4 Spin Polarization

The photophysical mechanism of Intersystem Crossing (ISC) populates the triplet states of a molecule starting from its excited singlet state [41]. This is the case of chlorophyll molecules, where the excitation upon absorption of Vis light induces the formation of an excited singlet state (S_1) which then converts into a triplet state by ISC. The transition should be forbidden, however the presence of the spin-orbit coupling, described by the spin-orbit hamiltonian $\hat{H}_{SO}$, permits a mixing of the orbital angular momentum with the spin angular momentum, allowing the transition.

Without an external magnetic field, the ISC matrix elements that characterize the interaction (and thus the transition) between the singlet state and the triplet sublevels are different due to the differences in the symmetrical properties:

$$< S_1|\hat{H}_{SO}|\tau_x > \neq < S_1|\hat{H}_{SO}|\tau_y > \neq < S_1|\hat{H}_{SO}|\tau_z > \tag{7.28}$$

In this situation, the population (p_i) and depopulation (k_i) rates of the triplet τ_i sublevels (i=x,y,z) depend on the square of the corresponding matrix element:

$$p_i \propto | < S_1|\hat{H}_{SO}|\tau_i > |^2 \tag{7.29}$$

$$k_i \propto | < \tau_i|\hat{H}_{SO}|S_1 > |^2 \tag{7.30}$$

When a magnetic field is applied, the population (P_j) and depopulation (K_j) rates of the triplet T_j sublevels (with j=+1,0-1) are

$$P_j = \sum_i |c_{i,j}|^2 p_i \tag{7.31}$$

$$K_j = \sum_i |c_{i,j}|^2 k_i \tag{7.32}$$

where $c_{i,j}$ is the coefficient of the linear combination of the i-th ZF function that contributes to the j-th function in presence of the magnetic field.
For these reasons, each triplet sublevel will be populated in a selective way according to the magnitude of the spin-orbit interaction and the balance between population rate and depopulation rate. The population distribution of triplet states will not necessarily follow the normal Boltzmann statistic. This situation usually identifies a system defined as polarized [93].

In an EPR experiment, the intensity of a transition band between two triplet states is proportional to the population difference between the states put in resonance. For instance, a transition between the T_0 and the T_{+1} states when $\mathbf{B}_0 \parallel Z$ will have an intensity:

$$I_{0\rightarrow+1} \propto P_{+1} - P_0 \propto \frac{1}{2}(p_x - p_y) - p_z \tag{7.33}$$

and the signal will be in absorption or in emission according to the magnitude of P_{+1} and P_0. For the transition between the T_{-1} and the T_0 states the EPR intensity will be:

$$I_{-1\rightarrow0} \propto P_0 - P_{-1} \propto p_z - \frac{1}{2}(p_x - p_y) = -I_{0\rightarrow+1} \tag{7.34}$$

This means that if a transition between two states $M_S = 0 \leftrightarrow M_S = +1$ will be in absorption, the corresponding transition $M_S = -1 \leftrightarrow M_S = 0$ will be in emission and viceversa, thus creating a symmetric spectrum with an inversion point in its centre.

7.1.5 Triplet-Triplet Energy transfer

Another way to populate triplet states is via a Triplet Triplet Energy Transfer (TTET) from a triplet donor (D) to a triplet acceptor (A). This is the case of carotenoids, where the mechanism of ISC has low probability.
In TTET, a simultaneous exchange of two electrons between a pair of interacting molecules takes place, conserving the total angular momentum. The donor in its triplet state (^3D) interacts with an acceptor in a singlet state (^1A) to give a final system characterized by the donor in a singlet state (^1D) and the acceptor in its triplet state (^3A):

$$^3D +^1 A \rightarrow^1 D +^3 A \tag{7.35}$$

The process can be described by the Dexter mechanism, which requires an overlap between the molecular orbitals of the interacting donor-acceptor pair [94, 95]. The probability of electron transfer from one of the i-th ZFS levels of the donor, $\tau_{i,D}$, to one of the j-th ZFS levels of the acceptor $\tau_{j,A}$ is proportional to the square of the electronic exchange integral:

$$W_{i\rightarrow j} \propto | < \phi_D^{(3)}(1)\tau_{i,D}(1)\phi_A^{(1)}(2)\sigma_A(2)|\frac{1}{r_{1,2}}|\phi_D^{(1)}(1)\sigma_D(1)\phi_A^{(3)}(2)\tau_{j,A}(2) > |^2 \tag{7.36}$$

where $\phi_D^{(3)}$ is the spacial part of the donor wavefunction in the triplet state and $\tau_{i,D}$ one of its i-th triplet spin parts, $\phi_A^{(1)}$ stands for the acceptor spacial wavefunction in the singlet state and σ_A its

singlet spin part. $\phi_D^{(1)}$ identifies the donor spacial wavefunction in the singlet state and σ_D its singlet spin part, while $\phi_A^{(3)}$ is the spacial part of the acceptor in triplet state and $\tau_{j,A}$ one of its j-th triplet spin states. The numbers in parenthesis are referred to the two electrons involved in the process.
The operator $1/r_{1,2}$ has an effect only on the spacial coordinates, so the integral can be factorized:

$$W_{i\to j} \propto |<\tau_{i,D}(1)|\tau_{j,A}(2)>|^2 |<\sigma_A(2)|\sigma_D(1)>|^2 |<\phi_D^{(3)}(1)\phi_A^{(1)}(2)|\frac{1}{r}|\phi_D^{(1)}(1)\phi_A^{(3)}(2)>|^2 \quad (7.37)$$

Only the first term depends on the overlap integral between the triplet states of the donor and the accept, making the mechanism dependent on the relative orientation between the ZFS axis of the donor and the acceptor:

$$W_{i\to j} \propto \cos^2\theta_{ij} \quad (7.38)$$

where θ_{ij} is the angle between the ZFS axis of the i-th sublevel of the donor and the ZFS axis of the j-th sublevel of the acceptor.
The TTET probability $W_{i\to j}$ can be further associated to the spin population of the system, and thus on its spin polarization. In this way, the spin polarization of the acceptor, investigated by EPR spectroscopy, can give information on the relative orientation and on the spin polarization of the donor.

7.2 TR-EPR experiment

In an EPR experiment, the interaction with a static magnetic field and an electromagnetic radiation both applied on the spin system is analysed [87].
The simplest EPR technique is CW-EPR (continuous wave EPR), where the sample is irradiated by a continuous monochromatic radiation in the frequency domain of microwaves (MW) while a slow scan of intensities of the external magnetic field is performed. The most common CW-EPR is X-band EPR, where a radiation between 9 and 10 GHz is used.
If the resonance conditions are verified, meaning that the energy difference between two spin states at the given value of external magnetic field matches the energy transported by the radiation, a transition is induced. The transition is allowed only if the selection rule $\Delta M_S = \pm 1$ is verified.
The sample is introduced and analysed inside a resonant cavity coupled to the monochromatic microwave radiation in order to maximise the magnetic component and minimize the electric component of the radiation at the level of the sample.

In TR-EPR experiments, an additional dimension is monitored during the analysis, which is the temporal evolution of the system. TR-EPR is based on the principles of CW-EPR, but with the peculiarity that the signals arriving at the detector at each value of external magnetic field are recorded in time (transients), thus creating a time resolution. In a photoexcited TR-EPR

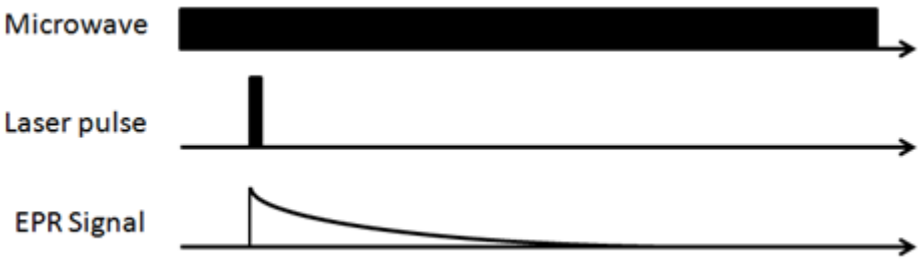

Figure 7.5: Scheme for a TR-EPR experiment. The sequence is performed at every magnetic field intensity.

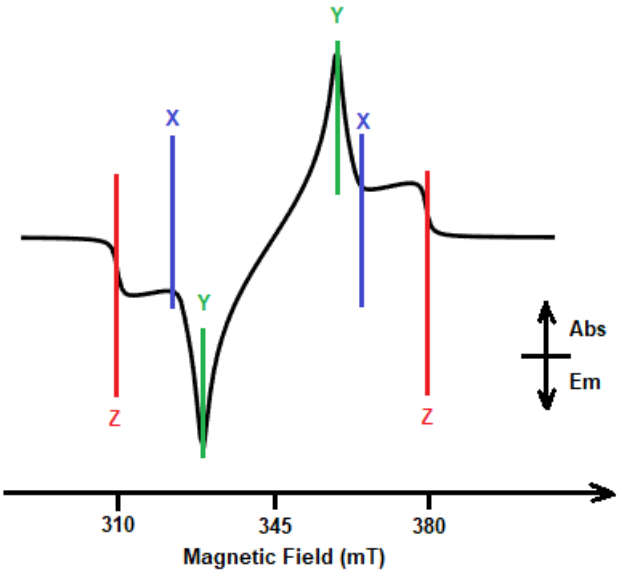

Figure 7.6: Generic triplet state X-band TR-EPR spectrum of chlorophyll. The absorption and emission pattern is set as *eaeaea*.

measurement, a focused laser pulse is sent inside the resonant cavity at the level of the sample in order to induce electronic excitations. After the pulse, the time evolution of the EPR signal is monitored. The procedure is performed separately at each value of external magnetic field. The collected series of time traces at each value of magnetic field give a final three-dimensional surface representing the evolution of the spectrum in time.

7.2.1 TR-EPR spectrum of triplet state

As stated in the previous sections the resonance conditions depend on the orientation of the molecule compared to the direction of the external magnetic field. As it can be seen in Figure 7.4, for each orientation of the molecule there are two possible transitions. This means that in a disordered solid sample the spectrum will be composed by a pair of lines for every molecule, with a splitting that depends on the orientation of the molecule in the system relatively to the magnetic field. Overall, the spectrum will result in the convolution of all the possible lines of a uniformly disorder macroscopic system [93]. It is possible to identify in the spectrum six characteristic features, called "turning points", that correspond to the transitions generated when the molecules' ZFS axis are oriented parallel to the external field. In addition, the spectrum will

be spin polarized, meaning that the turning points will be shown in absorption or in emission according to the specific spin-orbit coupling [93]. The absorption and the emission pattern will be symmetric relatively to its centre. In Figure 7.6, a typical spectrum of triplet state of chlorophylls is shown.

7.3 EPR analysis of OCP

Solid state TR-EPR spectroscopy was applied on different samples. The first one containing only OCP in solution, the second containing OCP adsorbed on SBA-15-NH_2 and the third containing both Chla and OCP adsorbed on SBA-15-NH_2. A control sample was prepared adsorbing only Chla on SBA-15-NH_2.

7.3.1 Sample Preparation

1. First sample (OCP in solution):
   200 μL of OCP solution 45 μM (solvent: 50% buffer, 50% degassed glycerol) were introduced in an EPR quartz tube and sealed under vacuum.

2. Second sample (OCP in SBA-15-NH_2):
   15 mg of SBA-15-NH_2 were introduced in a 1.5 mL Eppendorf test tube with 180 μL of OCP stock solution 30 μM and 820 μL of water. The sample was incubated for 4 hours under mild agitation. After, the sample was centrifuged for 15 minutes at 10000 rpm. The nanoparticles were collected, dried overnight and inserted in a quartz EPR tube sealed under vacuum.

3. Third sample (OCP + Chla in SBA-15-NH_2):
   15 mg of SBA-15-NH_2 were introduced in a 1.5 mL Eppendorf test tube with 250 μL of a solution of chlorophyll *a* in THF 107 μM. The sample was stirred vigorously for a few seconds and left in the dark overnight in order to let the solvent evaporate. Next, 180 μL of OCP stock solution 30 μM and 820 μL of water were added in the test tube, which was gently stirred for 4 hours (Chla:OCP ratio of 5:1). After incubation, the sample was centrifuged for 15 minutes at 10000 rpm. The nanoparticles were collected, dried overnight and inserted in a quartz EPR tube sealed under vacuum. The incubation with OCP doesn't remove chlorophyll from SBA-15-NH_2 surface because the pigment is not soluble in water.

4. Fourth sample (Chla in SBA-15-NH_2):
   15 mg of SBA-15-NH_2 were introduced in a 1.5 mL Eppendorf test tube with 400 μL of Chla solution in THF 140 μM. The sample was stirred vigorously for a few seconds and left in the dark overnight in order to let the solvent evaporate. After evaporation, the powder was collected and inserted in a quartz EPR tube sealed under vacuum.

7.3.2 Instrumentation

TR-EPR measurements were carried out at 80 K using a Bruker Elexsys E580 spectrometer. A Nd-YAG pulse laser (Quantel Brilliant, 20 Hz, 3 mJ per pulse) equipped with second (532 nm) and third (355 nm) harmonic generators was used to photoexcite the system. An Optical Parametric Oscillator (Opolette, OPOTEK) device is coupled to the pulse laser to get tunable wavelengths from 420 nm to 680 nm and from 750 nm to 1000 nm. The temperature was controlled with a nitrogen flow cryostat. Signals ware recorded with a LeCroy 5LT364 digital oscilloscope, triggered by the laser pulse.
Simulations of the obtained spectra were performed using the EasySpin package run by the MATLAB software.

7.3.3 Results

TR-EPR measurements on OCP in solution (first sample) and in SBA-15-NH_2 (second sample) were conducted under laser pulsed photoexcitation at 490 nm (carotenoid maximum absorption). No detectable signals were recorded during the experiment, meaning that formations of paramagnetic species such as charge-separation states and triplet states do not occur after direct photoexcitation of the system, thus excluding the possibility that the photoactivation cycle of the protein passes through paramagnetic states.

The third sample, containing OCP and Chla adsorbed on SBA-15-NH_2, was analysed under two different excitation wavelengths, 660 nm and 425 nm, which coincide respectively with the Qy and Soret absorption bands of chlorophyll. Moreover, at 425 nm significant absorption from the carotenoid is also present. In this way, a maximum energy absorption from the system is guaranteed. The experimental EPR spectra for both excitations at 660 nm and at 425 nm are reported in Figure 7.7. It can be seen a very different response of the system after changing the excitation wavelength:

- Excitation at 660 nm:
  The TR-EPR spectrum does not show any evidence of contributions arising from a triplet state of the carotenoid. In fact, after performing a simulation of the spectrum (see Figure 7.8), the simulated ZFS parameters are D = 850 MHz and E = -110 MHz, which are very close to the ZFS parameters of chlorophyll triplet state. The control sample containing only Chla in SBA-15-NH_2 was analysed as well with TR-EPR (see Figure 7.9) in order to determine if a correspondence between the two different samples is shown. Indeed, the simulated spectrum of the system containing only Chla in SBA-15-NH_2 presents ZFS parameters of D = 860 MHz and E = -105 MHz. The differences between the values of the two samples are very limited, taking us to conclude that photoexcitation at 660 nm leads to the accumulation of the triplet state of the adsorbed Chla but not of the internal OCP's carotenoid. Even the populations of the triplet sublevels Z, Y and X, as determined by the fitting procedure, are very similar: [0.1 0.54 0.36] for the sample containing OCP

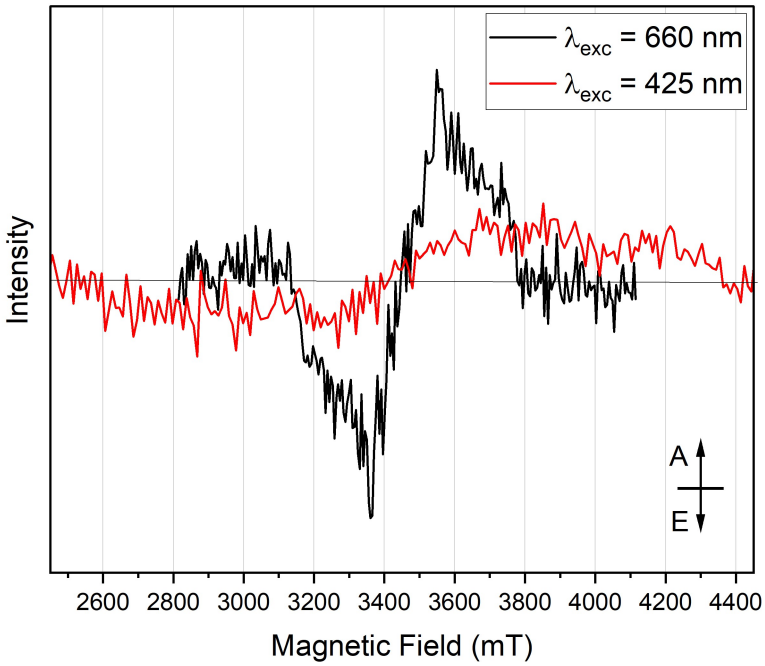

Figure 7.7: Experimental EPR spectra of Chla and OCP adsorbed simultaneously on SBA-15-NH_2 nanoparticles. Black trace: excitation at 660 nm; MW freq: 9.716 GHz; MW power: 0.65 mW; Power attenuation: 25 dB. Red trace: excitation at 425 nm; MW freq: 9.732 GHz; MW power: 0.65 mW; Power attenuation: 25 dB.

and [0.1 0.51 0.39] for the sample with only Chla.

Most likely, the explanation under the fact that no carotenoid triplets are shown is that the Chla photosensitizer does not interact efficiently with the carotenoid. An excessive distance between the molecules and/or an incorrect orientation of their ZFS axes prevent an efficient TTET and thus the formation of the triplet state of the carotenoid.

It is important to notice also that the ZFS parameters of Chla in SBA-15-NH_2 are similar, but not identical, to the ones calculated for Chla in organic solvents. For example, in MeTHF, D= 846 MHz and E = - 114 MHz [96]. In pyridine, D = 825 MHz and E = - 109 MHz [97]. The specific chemical interactions between the chlorophyll molecules and the NH_2 moieties of the functionalized SBA-15 matrix can influence the triplet state and thus the ZFS parameters. Also, possible distortions of the molecular geometry of Chla in order to adapt to the silica surface can affect eventually the spectroscopic response.

- Excitation at 425 nm:

  The spectrum at 425 nm is very different from the previous one. There are clearly some additional features in the regions at lower and higher values of magnetic field which might seem characteristic of carotenoids. At 425 nm, not only chlorophyll absorbs light, but also the carotenoid of protein (moderately), which can eventually start to photoactivate and change its conformation. We suppose here that the photoactivated state of the protein, which presents a more elongated shape and an internal carotenoid that is more exposed, can interact more effectively with chlorophyll, leading to formation of carotenoid triplet

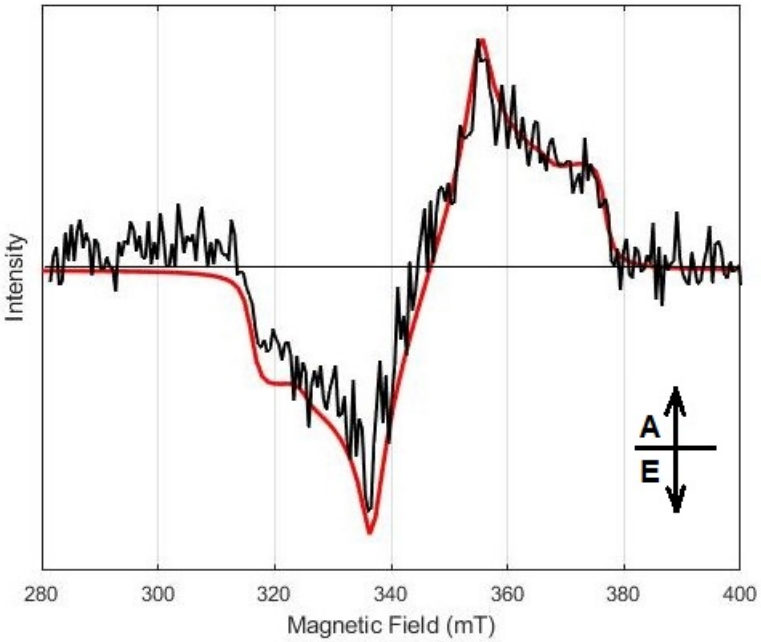

Figure 7.8: Black trace: experimental EPR spectrum of Chla and OCP adsorbed simultaneously on SBA-15-NH_2 nanoparticles. MW freq: 9.716 GHz; MW power: 0.65 mW; Power attenuation: 25 dB; λ_{exc} = 660 nm. Red trace: simulation of the EPR spectrum. The simulation parameters were: g = 2.0 (isotropic); D = 850 MHz; E = -110 MHz; Spin populations for, respectively, Z,Y, and X sublevels: [0.1 0.54 0.36].

state. However, this interpretation remains merely hypothetical, as the spectrum is not well resolved and simulations cannot be performed.

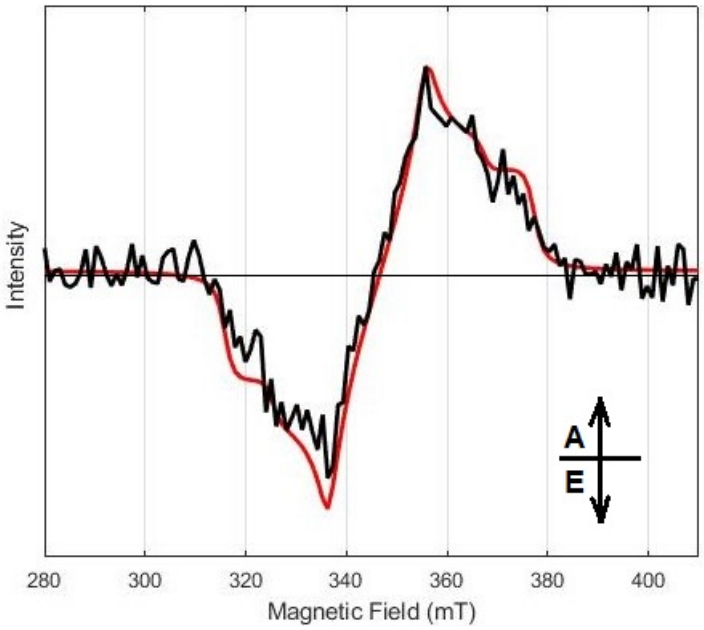

Figure 7.9: Black trace: experimental EPR spectrum of Chla adsorbed on SBA-15-NH_2 nanoparticles. MW freq: 9.716 GHz; MW power: 0.65 mW; Power attenuation: 25 dB; λ_{exc} = 532 nm. Red trace: simulation of the EPR spectrum. The simulation parameters were: g = 2.0 (isotropic); D = 860 MHz; E = -105 MHz; Spin populations for, respectively, Z,Y, and X sublevels: [0.1 0.51 0.39].

8

Conclusions

The presented research work covers a multitude of aspects and approaches joined together by a common factor: Orange Carotenoid Protein. Starting from spectroscopic analysis by DS-FTIR, passing through synthesis and characterization of fluorescent silica nanoparticles, and concluding with the spectroscopic EPR technique, a comprehensive study under multiple points of view was performed.

The first objective of the study consisted in a spectroscopic investigation on the photoactivation mechanism of OCP. Time resolved difference infrared spectroscopy, DS-FTIR, applied to our system provided a method to understand some of the details of the photoactivation cycle. In particular, two main characteristics of the process were defined. First, studying the spectral region where stretching bands of water are located, it was possible to demonstrate that internal water molecules, weakly H-bonded to the protein, may participate directly in the photoactivation mechanism. Specifically, the positive band at 3649 cm^{-1} in the difference spectrum, which downshifts at 2712 cm^{-1} after deuteration of the sample, was assigned to the stretching normal modes of respectively H_2O and D_2O molecules actively participating in the mechanism. A second aspect concerning the activation cycle was assessed analyzing the canonical frequency region of the protein spectrum. By looking at the time evolution of the system under photoactivation, it was concluded that the process involving conformational changes of the protein takes place in a synchronized single-step way without formation of long-lived intermediate species.

The second part of the project was dedicated to the synthesis and characterization of tunable fluorescent OCP-based SBA-15-NH_2 silica nanoparticles. We began with the synthesis of functionalized SBA-15-NH_2 nanoparticles starting from normal SBA-15. Several characterization methodologies, including SEM and TEM imaging, thermogravimetric analysis, PZC determination and nitrogen physisorption could demonstrate an effective functionalization of the starting SBA-15 material with NH_2 moieties, making the system suitable for protein adsorption. After following a protocol for OCP immobilization inside SBA-15-NH_2, UV-Vis solid state spectroscopy demonstrated that OCP remains photoactive even when adsorbed on the solid support, and its photoactivation mechanism was found to be reversible.

Taking advantage of the reversible spectral properties of OCP immobilized on SBA-15-NH_2, the protein and different fluorophores (Cyanine 3, Cyanine 5 and 3-hydroxyflavone) were ad-

sorbed simultaneously on the nanoparticles. Hypothesizing a tunable mechanism of energy transfer between the protein and the fluorophores by OCP photoactivation, the final synthesized nanoparticles were definitely characterized by an efficient fluorescence emission that could be easily modulated by OCP photoactivation.

The last part of the project was dedicated on EPR spectroscopy with the objective of detecting paramagnetic states in OCP. However, no radicals or triplet states or charge-separation states were observed in OCP, both in solution and in SBA-15-NH_2. This is in agreement with the optical studies performed on the protein and also shows that the nanoparticles do not create an altered environment that promotes side photoreactions. To mimic the TTET occurring between chlorophylls and carotenoids in photosynthetic systems, we adsorbed OCP and chlorophyll *a* on SBA-15-NH2 with the aim of exploiting the nanopores to bring the pigments in close contact. The triplet state of Chla was observed in the TR-EPR spectrum, characterized by its typical ZFS parameter D and E, when exciting the sample at the Qy absorption band of Chla. In this case, identification of any signals coming from the carotenoid was not possible. Interestingly, a different signal was detected when exciting at 425 nm: the chlorophyll triplet state was largely decreased and new features appeared in the spectrum. At this wavelength not only the chlorophyll but also the carotenoid moiety is absorbing, photoactivating the protein and exposing its carotenoid. However, since the signal was very weak, it was not possible to assign it definitely to the carotenoid triplet state. Further experiments are needed to clarify this point and to optimize the conditions for TTET in the system.

9

Acknowledgments

I would like to address my gratitude towards Prof. Donatella Carbonera for accepting me as his master student and for supervising my thesis project. Her scientific rigorousness and professional experience were essential for the positive outcome of this project.

Many thanks must be undoubtedly addressed towards Dr. Alberto Mezzetti for welcoming me in his laboratory at LRS - Sorbonne University, Paris. I genuinely thank him for making me part of his research project and for supervising my work. He has been thoroughly helpful and kindly available in all circumstances.

I sincerely thank Prof. Marco Bortolus for his kind supervision and availability, especially during EPR measurements.

Special thanks must be dedicated to PhD student Silvia Leccese. I will not forget her help and precious support during my internship in France.

Lastly, I would like to thank my family and friends. They are my true strength and blessing.

Bibliography

[1] Beverley R. Green, William W. Parson *Light-Harvesting Antennas in Photosynthesis*, Springer Dordrecht (2004).

[2] Barbara Demmig-Adams, Gyozo Garab, William Adams III, Govindjee *Non-Photochemical Quenching and Energy Dissipation in Plants, Algae and Cyanobacteria*, Springer Dordrecht (2010).

[3] Kerfeld, C. A.; Melnicki, M. R.; Sutter, M.; Dominguez-Martin, M. A. *New Phytologist*, **2017**, *215*, 937-951.

[4] Muzzopappa, F.; Kirilovsky, D. *Trends in Plant Science*, **2020**, *25*, 92-104.

[5] Holt, T. K.; Krogmann, D. W. *Biochim. Biophys. Acta.*, **1981**, *637*, 408-414.

[6] Wu, Y. P.; Krogmann, D. W. *Biochim. Biophys. Acta.*, **1997**, *1322*, 1-7.

[7] Wilson, A.; Ajlani, G.; Verbavatz, J.-M.; Vass, I.; Kerfeld, C. A.; Kirilovsky D. *The Plant Cell*, **2006**, *18*, 992-1007.

[8] Wilson, A.; Punginelli, C.; Gall, A.; Bonetti, C.; Alexandre, M.; Routaboul, J.-M.; Kerfeld, C. A.; van Grondelle, R.; Robert, B.; Kennis, J. T. M.; Kirilovsky, D. *PNAS*, **2008**, *105 (33)*, 12075-12080.

[9] Bao, H.; Melnicki, M. R.; Pawlowski, E. G.; Sutter, M.; Agostoni, M.; Lechno-Yossef, S.; Cai, F; Montgomery, B. L.; Kerfeld, C. A. *Nature Plants 3*, **2017**, 17089.

[10] Melnicki, M. R.; Leverenz, R. L.; Sutter, M.; Lopez-Igual, R.; Wilson, A.; Pawlowski, E. G.; Perreau, P.; Kirilovsky D.; Kerfeld, C. A. *Molecular Plant*, **2016**, *9*, 1379–1394.

[11] Muzzopappa, F.; Wilson, A.; Yogarajah, V.; Cot, S.; Perreau, F.; Montigny, C.; Bourcier de Carbon, C.; Kirilovsky, D. *Plant Physiology*, **2017**, *175*, 1283–1303.

[12] Kerfeld, C. A.; Sawaya, M. R.; Brahmandam, V.; Cascio, D.; Ki Ho, K.; Trevithick-Sutton, C. C.; Krogmann, D. W.; Yeates, T. O. *Structure*, **2003**, *11*, 55-65.

[13] Wilson, A.; Kinney, J. N.; Zwart, P. H.; Punginelli, C.; D'Haene, S.; Perreau, F.; Klein, M. G.; Kirilovsky, D.; Kerfeld, C. A. *J. Biolog. Chem.*, **2010**, *285*, 18364- 18375.

[14] Bourcier de Carbon, C.; Thurotte, A.; Wilson, A.; Perreau, F.; Kirilovsky, D. *Scientific Reports*, **2015**, *5 : 9085*.

[15] Andreeva, E. A.; Niziński, S.; Wilson, A.; Levantino, M.; De Zitter, E.; Munro, R.; Muzzopappa, F.; Thureau, A.; Zala, N.; Burdzinski, G.; Sliwa, M.; Kirilovsky, D.; Schirò, G.; Colletier, J.-P. *Biophysical Journal*, **2022**, *121*, 2849-2872.

[16] Liu, H.; Zhang, H.; Orf, G. S.; Lu, Y.; Jiang, J.; King, J. D.; Wolf, N. R.; Gross, M. L.; Blankenship, R. E. *Biochemistry*, **2016**, *55*, 1003-1009.

[17] Leverenz, R. L.; Sutter, M.; Wilson, A.; Gupta, S.; Thurotte, A.; Bourcier de Carbon C.; Petzold, C. J.; Ralston, C.; Perreau, F.; Kirilovsky, D.; Kerfeld, C. A. *Science*, **2015**, *348*, 1463-1466.

[18] Slouf V.; Kuznetsova, V.; Fuciman, M.; Bourcier de Carbon, C.; Wilson, A.; Kirilovsky, D.; Polıvka, T. *Photosynth Res*, **2017**, *131*, 105-117.

[19] Maksimov, E. G.; Sluchanko, N. N.; Slonimskiy, Y. B.; Slutskaya, E. A.; Stepanov, A. V.; Argentova-Stevens, M.; Shirshin, E. A.; Tsoraev, G. V.; Klementiev, K. E.; Slatinskaya, O. V.; Lukashev, E. P.; Friedrich, T.; Paschenko, V. Z. ; Rubin, A. B. *Scientific Reports*, **2017**, *7: 15548*.

[20] Konold, P. E.; van Stokkum, I. H. M.; Muzzopappa, F.; Wilson, A.; Groot, M.-L., Kirilovsky, D.; Kennis, J. T. M. *JACS*, **2019**, *141*, 520-530.

[21] Yaroshevich I. A.; Maksimov, E. G.; Slunchanko, N. N.; Zlenko, D. V.; Stepanov, A. V.; Slutskaya, E. A.; Slonimskiy, Y. B.; Botnarevskii, V. S.; Rameeva, A.; Gushlin, I.; Kovalev, K.; Gordeliy, V. I.; Shelaev, I. V.; Gostev, F. E.; Khakhulin, D.; Poddubnyy, V. V.; Timofey, S. G.; Cherapanov, D. A.; Polivka, T.; Kloz, M.; Friedrich, T.; Paschenko, V. Z.; Nadtochenko, V. A.; Rubin, A. B.; Kirpichnikov, M. P. *Communications Biology*, **2021**, *4:539*.

[22] Khan, T.; Kuznetsova, V.; Dominiguez-Martin, M. A.; Kerfeld, C. A.; Polivka, T. . *ChemPhotoChem*, **2022**, *6*, e202100194.

[23] Nizinski, S.; Wilson, A.; Uriarte, l. M.; Ruckebusch, C.; Andreeva, E. A.; Schlichting, I.; Colletier, J.-P.; Kirilovsky, D.; Burdzinski, G.; Sliwa, M. *JACS Au*, **2022**, *2*, 1084-1095.

[24] Andersson, P. O.; Gillbro, T. *J. Chem. Phys*, **1995**, *103*, 2509-2519.

[25] Kish, E.; Pinto, M. M. M.; Kirilovsky, D.; Spezia, R.; Robert, B. *Biochim. Biophys. Acta*, **2015**, *1847*, 1044.

[26] Punginelli, C.; Wilson, Routaboul, J.-M.; Kirilovsky, D. *Biochim. Biophys. Acta*, **2009**, *1787*, 280-288.

[27] Mezzetti, A.; Alexandre, M.; Thurotte, A.; Wilson, A.; Gwizdala, M.; Kirilovsky, D. *J. Phys. Chem. B*, **2019**, *123*, 3259-3266.

[28] Zhang, H.; Liu, H.; Niedzwiedzki, D. M.; Prado, M.; Jiang, J.; Gross, M. L.; Blankenship R. E. *Biochemistry*, **2014**, *53*, 13-19.

[29] Wilson, A.; Gwizdala, M.; Mezzetti, A.; Alexandre, M.; Kerfeld, C.A.; Kirilovsky, D. *Plant Cell*, **2012**, *24*, 1972-1983.

[30] Wilson, A.; Muzzopappa, F.; Kirilovsky, D. *BBA Bioenergetics*, **2022**, *1863, 148504*.

[31] Leverenz, R. L.; Jallet, D.; Li, M.-D.; Mathies, R. A.; Kirilovsky, D.; Kerfeld, C. A. *The Plant Cell*, **2014**, *26*, 426-437.

[32] Gwizdala, M.; Wilson, A.; Kirilovsky, D. *The Plant Cell*, **2011**, *23*, 2631–2643.

[33] Squires, A. H.; Dahlberg, P. D.; Liu, H.; Magdaong, N.C.M.; Blankenship, R. E.; Moerner, W. E. *Nature Communications*, **2019**, *10:1172*.

[34] Jallet, D.; Thurotte, A.; Leverenz, R. L.; Perreau, F.; Kerfeld, C. A.; Kirilovsky, D. *Plant Physiology*, **2014**, *2*, 790-804.

[35] Gwizdala, M.; Wilson, A.; Omairi-Nasser, A.; Kirilovsky, D. *Biochimica et Biophysica Acta*, **2013**, *1827*, 348-354.

[36] Sutter, M.; Wilson, A.; Leverenz, R. L.; Lopez-Igual, R.; Thurotte, A.; E. Salmeen, A.; Kirilovsky, D.; Kerfeld, C. A. *PNAS*, **2013**, *110 (24)*, 10022-10027.

[37] Sedoud, A.; Lopez-Igual, R.; ur Rehman, A.; Wilson, A.; Perreau, F.; Boulay, C.; Vass, I.; Krieger-Liszkay, A.; Kirilovsky, D. *The Plant Cell*, **2014**, *26*, 1781-1791.

[38] Lopez-Igual, R.; Wilson, A.; Leverenz, R. L.; Melnicki, M. R.; Bourcier de Carbon, C.; Sutter, M.; Turmo, A.; Perreau, F.; Kerfeld, C. A.; Kirilovsky, D. *Plant Physiol.*, **2016**, *171*, 1852-1866.

[39] Andreoni, A.; Lin, S.; Liu, H.; Blankenship, R. E.; Yan, H.; Woodbury, N. W. *Nano Lett.*, **2017**, *17*, 1174–1180.

[40] Maksimov, E. G.; Yaroshevich, I. A.; Tsoraev, G. V.; Sluchanko, N. N.; Slutskaya, E. A.; Shamborant, O. G.; Bobik, T. V.; Friedrich, T.; Stepanov, A. V. *Sci Rep.*, **2019**, *9:8937*.

[41] Peter Atkins; Julio de Paula *Atkins' Physical Chemistry*, 10th Edition, Oxford University Press (2014).

[42] Barth, A. *Biochimica et Biophysica Acta*, **2007**, *1767*, 1073-1101.

[43] Mezzetti, A.; Schnee, J.; Lapini, A.; Di Donato, M. *Photochemical & Photobiological Sciences*, **2022**, *21*, 557–584.

[44] Kottke, T.; Lorenz-Fonfria, V. A.; Heberle, J. *J. Phys. Chem. B*, **2017**, *121*, 335-350.

[45] Mezzetti, A.; Leibl, W. *Photosynthesis Research*, **2016**, *131*, 121-144.

[46] Krimm, S.; Bandekar, J. *Advances in Protein Chemistry*, **1986**, *38*, 181-364.

[47] Abe, Y.; Krimm, S. *Biopolymers*, **1972**, *11*, 1817–1839.

[48] Brauner, J.W.; Dugan, C.; Mendelsohn, R. *J. Am. Chem.Soc.*, **2000**, *122*, 677–683.

[49] Goormaghtigh, E.; Cabiaux, V.; Ruysscheart, J.-M. *Subcell. Biochem.*, **1994**, *23*, 405-450.

[50] Oberg, K.A.; Ruysschaert, J.M.; Goormaghtigh, E. *Eur. J. Biochem.*, **2004**, *271*, 2937-2948.

[51] Cai, S.; Singh, B. R. *Biochemistry*, **2004**, *43*, 2541-2549.

[52] Venyaminov, S. Y.; Prendergast, F. J. *Analytical Biochemistry*, **1997**, *248*, 234–245.

[53] Leccese, S. *Interactions between Orange Carotenoid Protein and mesoporous silica: from spectroscopic investigations to photoactive nanodevices* (PhD thesis), **2022**.

[54] Malferrari, M.; Venturoli, G.; Francia, F.; Mezzetti, A. *Spectroscopy: An International Journal*, **2012**, *27*, 337–342.

[55] Gupta, S.; Guttman, M.; Leverenz, R. L.; Zhumadilova, K.; Pawlowski, E. G.; Petzold, C. J.; Lee, K. K.; Ralston, C. Y.; Kerfeld, C. A. *PNAS*, **2015**, *112(41)*, E5567-74.

[56] Maeda, A. *Biochemistry (Moscow)*, **2001**, *66*, 1256-1268.

[57] Noguchi, T.; Sugiura, M. *Biochemistry*, **2000**, *39*, 10943-10949.

[58] Herzberg, G. *Molecular Spectra and Molecular Structure, II. Infrared and Raman Spectra of Polyatomic Molecules*, (1945) Princeton, NJ.

[59] Gupta, S.; Sutter, M.; Remesh, S. G.; Dominguez-Martin, M. A.; Bao, H.; Feng, X. A.; Chan, L.-J. G.; Petzold, C. J.; Kerfeld, C. A.; Ralston, C. Y. *J. Biol. Chem.*, **2019**, *294(22)*, 8848 –8860.

[60] Coglitore, D.; Janot, J.-M.; Balme, S. *Advances in Colloid and Interface Science*, **2019**, *270*, 278–292.

[61] Laurent, N.; Haddoub R.; Flitsch, S. L. *Trends in Biotechnology*, **2008**, *26*, 328-337.

[62] Zhao, D.; Wan, Y.; Zhou, W. *Ordered Mesoporous Materials*, Wiley (2013).

[63] Li, Z.; Zhang, Y.; Feng, N. *Expert Opinion on Drug Delivery*, **2019**, *16*, 219-237.

[64] Zhao, D.; Feng, J.; Huo, Q.; Melosh, N.; Fredrickson, G. H.; Chmelka, B. F.; Stucky, G. D. *Science*, **1998**, *279*, 548-552.

[65] Larki, A.; Saghanezhad, S. J.; Ghomi, M. *Microchemical Journal*, **2021**, *169 106601*.

[66] Jafari, S.; Derakhshankhah, H.; Alaei, L.; Fattahi, A.; Varnamkhasti, B. S.; Saboury, A. A. *Biomedicine & Pharmacotherapy*, **2019**, *109*, 1100-1111.

[67] Wan, Y.; Zhao, D. *Chemical Reviews*, **2007**, *107*, 2821-2860.

[68] Flodstrom, K.; Wennerstrom, H.; Alfredsson, V. *Langmuir*, **2004**, *20*, 680-688.

[69] Chaudhary, V.; Sharma, S. *J Porous Mater*, **2017**, *24*, 741–749.

[70] Yiu, H. H. P.; Botting, C. H.; Botting, N. P.; Wright, P. A. *Phys. Chem. Chem. Phys.*, **2001**, *3*, 2983-2985.

[71] Maria Chong, A. S.; Zhao, X. S. *J. Phys. Chem. B.*, **2003**, *107*, 12650-12657.

[72] Hudson, S.; Cooney, J.; Magner, E. *Angew. Chem. Int. Ed.*, **2008**, *47*, 8582 – 8594.

[73] Leccese, S.; Onfroy, T.; Wilson, A.; Kirilovsky, D.; Casale, S.; Guira, S.; Selmane, M.; Jolivalt, C.; Mezzetti, A. *Microporous and Mesoporous Material*, **2022**, *340 112007*.

[74] Sposito, G. *Environ. Sci. Technol.*, **1998**, *32*, 2815–2819.

[75] Sing, K. *Colloids and Surfaces*, **2001**, *187-188*, 3-9.

[76] Barrett, E. P.; Joyner, L. G.; Halenda, P. P. *J. Am. Chem. Soc.*, **1951**, *73*, 373.

[77] Brunauer, S.; Emmett, P. H.; Teller, E. *J. Am. Chem. Soc.*, **1938**, *60*, 309.

[78] Hecht, H. G. *Journal of Research of the National Bureau of Standards*, **1976**, *80A*, 567-583.

[79] Mishra, A.; Behera, R. K.; Behera, P. K.; Mishra, B. K.; Beher, G. B. *Chem. Rev.*, **2000**, *100*, 1973-2011.

[80] Herbst, E.; Shabat, D. *Org. Biomol. Chem.*, **2016**, *14*, 3715-3728.

[81] Harborne, J. B. *The Flavonoids Advances in Research Since 1986*, Chapman & Hall (1994).

[82] Shen, N.; Wang, T.; Gan, Q.; Liu, S.; Wang, L.; Jin, B. *Food Chemistry*, **2022**, *383, 132531*.

[83] Arriagada, F.; Gunther, G.; Morales, J. *Pharmaceutics*, **2022**, *12, 302*.

[84] Lazzaroni, S.; Dondi, D.; Mezzetti, A.; Protti, S. *Photochem. Photobiol. Sci.*, **2018**, *17*, 923-933.

[85] Landstrom, A.; Leccese, S.; Abadian, H.; Lambert, J.-F.; Concina, I.; Protti, S.; Seitsonen, A. P.; Mezzetti, A. *Dyes and Pigments*, **2021**, *185, 108870*.

[86] Roessler, M. M.; Salvadori, E. *Chem. Soc. Rev.*, **2018**, *47*, 2534-2553.

[87] Brustolon, M.; Giamello, E. *Electron Paramagnetic Resonance: A Practitioners Toolkit*, Wiley (2009).

[88] Tikhonov, A. N.; Subczynski, W. K. *Chem. Soc. Rev.*, **2019**, *77*, 47-59.

[89] Di Valentin, M.; Carbonera, D. *Journal of Physics B: Atomic, Molecular and Optical Physics*, **2017**, *50, 162001*.

[90] Focsan, A. L.; Magyar, A.; Kispert, L. D. *Archives of Biochemistry and Biophysics*, **2015**, *572*, 167-174.

[91] Di Valentin, M.; Bisol, A.; Agostini, G.; Moore, A. L.; Moore, T. A.; Gust, D.; Palacios, R. E.; Gould, S. L.; Carbonera, D. *Molecular Physics*, **2006**, *104*, 1595–1607.

[92] Weil, J. A.; Bolton, J. R. *Electron Paramagnetic Resonance: Elementary Theory and Practical Applications*, Wiley (2007).

[93] Richert, S.; Tait, C. E.; Timmel, C. R. *Journal of Magnetic Resonance*, **2017**, *280*, 103-116.

[94] Dexter D. L. *J. Chem. Phys.*, **1953**, *21*, 836-850.

[95] El-Sayed, M. A.; Tinti, D. S.; Yee, E. M. *J. Chem. Phys.*, **1969**, *51*, 5721-5723.

[96] Lendzian, F.; Bittl, R.; Telfer, A.; Lubitz, W. *Biochimica et Biophysica Acta*, **2003**, *1605*, 35-46.

[97] Angerhofer, A. *Chlorophyll Triplets and Radical Pairs*, CRC Press (1991).